Spatially-resolved mass transport in a liquid/liquid slug-flow micro-capillary reactor

Zur Erlangung des akademischen Grades eines
Dr.-Ing.
von der Fakultät Bio- und Chemieingenieurwesen
der Technischen Universität Dortmund
genehmigte Dissertation

von
Christian Heckmann
aus
Werne

Tag der mündlichen Prüfung: 3. Juli 2019
1. Gutachter: Prof. Dr.-Ing. Peter Ehrhard
2. Gutachter: Prof. Dr.-Ing. David W. Agar

Dortmund 2019

Abstract

The mass transport in a liquid/liquid slug-flow micro-capillary reactor is clarified by means of the investigation of the local mass transfer at the free interface. The transient mass transport is modeled based on the steady-state two-phase flow in a periodic element, with and without second-order chemical reaction, for dilute solutions and taking axial dispersion through wall film into account. An interface-tracking method is used for the direct numerical simulation of the mass transfer at the free interface. Therefore, separate phase-fitted and coupled computational domains are arranged on both sides of a numerically generated steady-state interface, computed with an existing simulation model. Numerical diffusion is minimized by means of the local alignment of the numerical mesh with the flow close to the free interface of the phase fitted and spatially highly-resolved computational domains. The steady-state two-phase flow and the transient mass transport are simulated one after another. Two mass-transfer test systems, a physical and a reactive test system, are selected and examined experimentally as basis for the validation of the numerical simulations and the investigation of the local mass transfer at the free interface. Results show, that the spatial distribution of the mass flux at the free interface is mainly determined by the Péclet number, i.e. the ratio of convection to diffusion. The flow through the wall film intensifies the local mass transfer and the transport between the solvent bulks for large Péclet numbers. For a large global ratio of convection and diffusion, more than 80% of mass is transferred through the wall film and the transfer at the caps is small. Furthermore, the local ratio of convection and diffusion inside the thin wall film, captured by a wall-film Péclet number, correlates with the spatial distribution of the mass flux at the free interface. An optimal average channel-velocity is derived.

Zusammenfassung

Der Stofftransport in einer flüssig/flüssig Pfropfenströmung in einem Mikrokapillarreaktor wird aufgeklärt anhand der Untersuchung des lokalen Stofftransfers an der freien Grenfläche. Der transiente Stofftransport wird auf Grundlage der stationären Zweiphasenströmung in einem periodischen Element, mit und ohne chemische Reaktion zweiter Ordnung, für verdünnte Lösungen und unter Berücksichtigung axialer Dispersion durch den Wandfilm modelliert. Eine Interface-Tracking Methode wird für die direkte numerische Simulation des Stofftransfers an der freien Grenzfläche genutzt. Separate, formangepasste und gekoppelte Rechengebiete werden dazu um eine importierte stationäre und numerisch generierte Grenzfläche angeordnet, erzeugt durch ein vorhandenes Simulationsmodell. Numerische Diffusion wird durch Ausrichtung der numerischen Rechennetze mit der Strömung nahe der freien Grenzfläche der örtlich hoch aufgelösten Rechtengebiete minimiert. Die stationäre Strömung und der transiente Stofftransport werden nacheinander simuliert. Die experimentelle Untersuchung zweier Stofftransport Testsysteme, einem physikalischen und einem reaktiven Stoffsystem, dient als Grundlage für die Validierung der numerischen Simulationen und zur detaillierten Untersuchung des lokalen Stofftransfers und der freien Grenzfläche. Die Ergebnisse für die untersuchten Stoffsysteme zeigen, dass die örtliche Verteilung des Stoffstroms durch die Grenzfläche maßgeblich durch die Péclet Zahl, d.h. das Verhältnis von Konvektion zu Diffusion, bestimmt wird. Die Strömung durch den Wandfilm intensiviert den lokalen Stoffdurchgang und den Transport zwischen den Kernbereichen der Phasen für große Péclet Zahlen. Für ein großes globales Verhältnis von Konvektion zu Diffusion, werden mehr als 80% der gesamten Stoffmenge durch den Wandfilm übertragen und der lokale Transfer an den Kappen ist klein. Weiter korreliert das lokale Verhältnis von Konvektion und Diffusion im dünnen Wandfilm, beschrieben durch eine Wandfilm-Pécletzahl, mit der lokalen Verteilung des Stoffstroms an der freien Grenzfläche. Eine optimale mittlere Kanalgeschwindigkeit wird abgeleitet.

... Wenn aber dieses alles möglich ist, auch nur einen Schein von Möglichkeit hat, - dann muß ja, um alles in der Welt, etwas geschehen. Der Nächstbeste, der, welcher diesen beunruhigenden Gedanken gehabt hat, mußanfangen, etwas von dem Versäumten zu tun; wenn es auch nur irgend einer ist, durchaus nicht der Geeignetste: es ist eben kein anderer da. Dieser junge, belanglose Ausländer, Brigge, wird sich fünf Treppen hoch hinsetzen müssen und schreiben, Tag und Nacht. Ja er wird schreiben müssen, das wird das Ende sein.

Malte Laurids Brigge

Danksagung

Contents

1

Introduction

Arising from the advancements in manufacturing technologies, cf. Ehrfeld et al. (2005), the miniaturization of characteristic length scales determines actually one promising possibility for the intensification of technological processes and their economical and technological improvement, cf. Kockmann (2008). Such apparatus, the so-called micro reactors, are defined by continuous flow through regular domains with characteristic dimensions much smaller than in conventional apparatus, cf. Hessel et al. (2004). The shortend transport length result in enhanced specific transport performances and advanced process control compared to conventional apparatus, cf. Jensen (2001) or van Gerven and Stankiewicz (2009).

The two-phase slug flow provides an especially advantageous ratio of process control to intensification, cf. Köhler and Cahill (2014). The stable and reproducible segmented flow structure, cf. Dittmar and Ehrhard (2013), guarantees a narrow residence-time distribution, cf. Gekle (2017), and shear-induced vortices intensify cross-mixing, cf. Bringer et al. (2004), in conjunction with a large specific interfacial area, cf. Ghaini et al. (2010). Following, the slug flow is especially useful for the performance of mass-transfer-limited processes, like in liquid/liquid systems, cf. Kashid et al. (2011). The application of the flow pattern in conjunction with economically produced micro capillaries with circular cross-section results in an adaptive and efficient micro reactor with high productivity, cf. Lomel et al. (2006).

The present contribution concentrates on the investigation of the mass transport within a liquid/liquid slug-flow micro-capillary reactor with and without influence of a chemical reaction. The spatial resolution the mass transfer at the free interface provides insight into the mass transport. The effective use of the free interface and in particular the role of the wall film within transfer process are examined. The local ratio of convection and diffusion inside the wall film is identified as crucial parameter for mass-transfer operations. Further, an optimal average channel velocity is derived.

1.1 Problem definition

In the present work, the mass transport within a liquid/liquid slug-flow micro-capillary reactor is examined. The slug flow consists of a continuous wetting phase (index c) and a disperse phase (index d), confined by a flow channel, i.e. a straight micro capillary with diameter d. The flow is driven by a pressure gradient ∇p. A cylindrical coordinate system (r, φ, z), with velocities (w_r, w_φ, w_z), is used for the description of the system. The two-phase flow is sketched in the
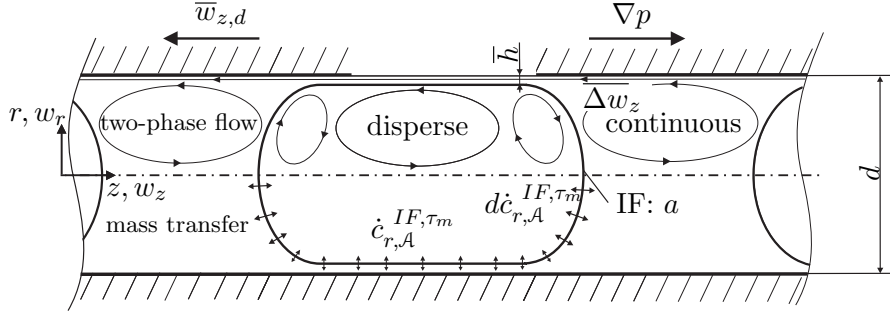
Figure 1.1: Problem sketch: liquid/liquid slug flow in a micro-capillary reactor.

upper half of figure 1.1 on basis of an observer moving with a velocity of the disperse phase $\overline{w}_{z,d}$. The shear-induced vortex structure that results from the velocity difference $\overline{\Delta w_z}$ of the phases. The phases act as solvents for a low concentrated solute $\mathcal{A}$, that is transferred from the raffinate (index r, concentration $c_{r,\mathcal{A}}$) into the extract solvent (index e, concentration $c_{e,\mathcal{A}}$) at the free interface (IF, specific area a). The mass flux at the free interface $\dot{c}_{r,\mathcal{A}}^{IF,\tau_m} = \dot{M}_{\mathcal{A}}^{IF,\tau_m}/V_r$, with $\dot{M}_{\mathcal{A}}^{IF,\tau_m}$ being the molar flux, transferred during the mass-transfer time τ_m, and V_r the volume of the raffinate solvent, can be enhanced by an irreversible chemical reaction with a second low concentrated solute $\mathcal{B}$ (concentration $c_{e,\mathcal{B}}$) inside the extract solvent, see figure 1.2. The mass transport is advantageously characterized in the present context by the volumetric mass-transfer coefficient and its spatial distribution at the free interface

$$ka = \frac{\dot{c}_{r,\mathcal{A}}^{IF,\tau_m}}{\Delta c_{\mathcal{A},ln}} = \int_a \frac{d\dot{c}_{r,\mathcal{A}}^{IF,\tau_m}}{\Delta c_{\mathcal{A},ln}} = \int_a d(ka). \tag{1.1}$$

The volumetric mass-transfer coefficient relates the mass flux at the free interface $\dot{c}_{r,\mathcal{A}}^{IF,\tau_m}$ to the driving mean-logarithmic concentration difference $\Delta c_{\mathcal{A},ln}$, see figure 1.2. By differentiation the local volumetric mass-transfer coefficient $d(ka)$ can be obtained, based on the local mass flux $d\dot{c}_{r,\mathcal{A}}^{IF,\tau_m}$ that is transferred at the differential element of specific interfacial area da. Spatial resolution of the mass flux at the free interface allows to study the mass transport within the slug-flow micro-capillary reactor.
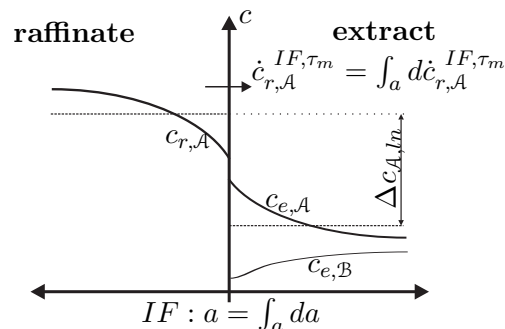
Figure 1.2: Problem sketch: schematic mass transfer at free interface.

1.2   Objective and outline

This thesis contributes to the understanding of the mass transport within a liquid/liquid slug-flow micro-capillary reactor by means of direct numerical simulation. The main goals are:

- Derivation of a model for the investigation of the mass transport, with and without chemical reaction, and its spatial resolution.

- Development, implementation, and validation of a numerical method that allows for the simulation of the spatially-resolved mass transport and in particular the local mass transfer at the free interface.

- Clarification of the mass transport within the liquid/liquid slug-flow micro-capillary reactor.

This thesis is structured as follows: Problem definition and objective build the framework for the review of the current state of research in chapter one. In chapter two, a model for the description of the mass transport is set up and scaled. The used interface-tracking method and the related developed computational approach are presented and investigated by numerical tests, in chapter three. In chapter four, the experimental investigations in conjunction with two mass-transfer test systems are described. The experimental obtained volumetric mass-transfer coefficients are compared to the specifically adapted numerical simulation results. The spatial distribution of the mass transfer at the free interface, the influence of relevant parameters, and the underlying mass transport are examined for the selected mass-transfer test systems in chapter five. The thesis is summarized and an outlook to future developments is given in the last chapter.

1.3   Literature review

First, the slug-flow micro-capillary reactor, consisting of the reactor setup, the slug flow, and the determination of the volumetric mass-transfer coefficient, is introduced. Then the local mass transfer at the free interface within the slug flow is discussed. Additionally, methods for the direct numerical simulation of the mass transfer at free interfaces are presented.

1.3.1   Slug-flow micro-capillary reactor

Slug-flow micro-capillary reactor is a compound designation, cf. Jovanovic (2011), for the use of the micro-capillary reactor concept in conjunction with the two-phase slug flow for process engineering applications. The micro-capillary reactor belongs to the class of micro channels, cf. Kashid et al. (2015), characterized by a reactor length l_{re}, that is much larger than the hydraulic diameter d of the flow channel, i.e. $l_{re} \gg d$, schematically sketched in figure 1.3. Burns and Ramshaw (2001) show the advantages of the slug flow in conjunction with rapid mass-transfer limited liquid/liquid reaction systems, such as nitrations, hydrogenations, sulfonations, oxidations, or catalytic reactions, cf. Jovanovic (2011). Dummann et al. (2003), Ahmed et al. (2006), Kashid et al. (2007b), Fries et al. (2008), Dessimoz et al. (2008), Ghaini et al. (2010), Jovanović et al. (2012), Scheiff (2015), Kurt et al. (2016), and Plouffe et al. (2016) for example prove these advantageous process properties. The stable and reproducible process, cf. Dittmar (2015), with defined flow conditions, cf. Ehrfeld et al. (2005), offers enhanced process safety,

cf. Kiwi-Minsker and Renken (2005), a narrow residence-time distribution, cf. Muradoglu et al. (2007), large specific interfacial areas, cf. Ghaini et al. (2010), and large volumetric mass-transfer coefficients, cf. Burns and Ramshaw (2001), in conjunction with a large amount of cross-mixing, cf. Bringer et al. (2004), at low energy consumption compared to other two-phase flow patterns in micro reactors, cf. Triplett et al. (1999). Overviews focusing on mass transfer are provided by Kashid et al. (2011), Sobieszuk et al. (2012), Assmann et al. (2013), and Sotowa (2014) taking also the case of a gas/liquid slug flow into account, that has found more scientific attention so far.

Two-phase micro-capillary reactor

The micro-capillary reactor is characterized by a modular structure, consisting of low-cost capillaries and junctions with especially a circular cross-section, made of glass, stainless steel or chemically resistant polymers such as Poly-Ether-Ether-Ketone. In consequence a significantly lower manufacturing effort compared to chips or micro-structured micro channels results, cf. Nielsen et al. (2002) or Dummann et al. (2003). The basic structure of a continuously working co-current mass contactor is present for multiphase applications, cf. Perry et al. (1997), see figure 1.3, consisting of units for the generation, the residence-time, and the separation of the multiphase flow. In contrast to the direct meaning of the prefix micro, capillary diameters in the range 10^{-2} mm $\lesssim d \lesssim 10^0$ mm, cf. Lomel et al. (2006), are mainly used, in conjunction with volumetric flow rates in the range of 10^{-3} ml/min $\lesssim \dot{V} \lesssim 10^1$ ml/min, cf. Jovanovic (2011). This gives an advantageous ratio of process intensification, manufacturing costs, and pressure drop, cf. Baltes et al. (2008). Lomel et al. (2006) show that the productivity of a micro reactor is mainly characterized by the ratio of throughput and pressure drop. The pressure drop is mainly influenced by the volumetric flow rate and the reactor length, that is a crucial parameter for an economic system design, cf. Triplett et al. (1999).

The generation unit consists of two reservoirs in combination with syringe or piston pumps, steering the feed of the continuous and the disperse phase, and a mixing junction for the generation of the slug flow. Different geometrical arrangements of the junctions are used, e.g. summarized by Tsaoulidis (2015) and Mansur et al. (2008). Most common is the use of T-junctions in a counter-
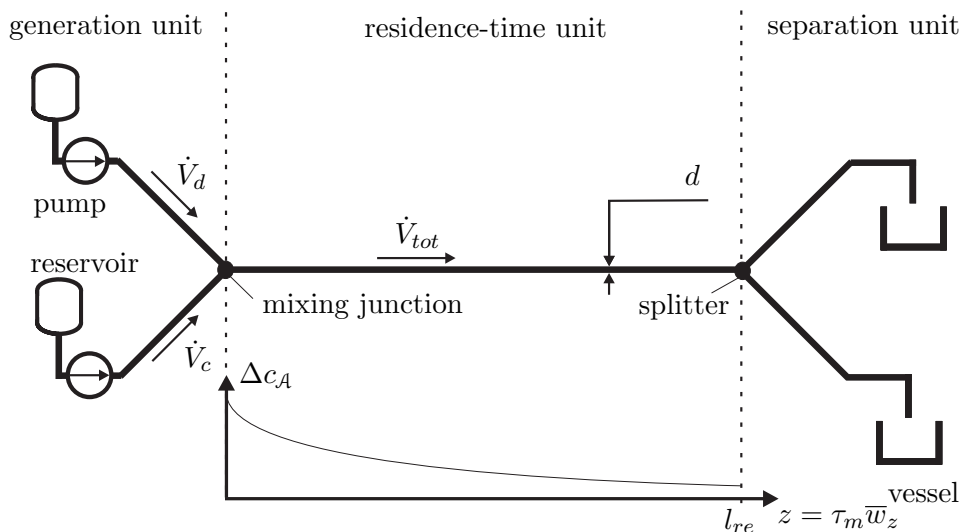

Figure 1.3: Basic modular structure of the examined slug-flow micro-capillary reactor, consisting of a generation unit, a straight residence-time unit, with circular cross-section and a separation unit, emphasizing the continuous mode of operation.

flow or cross-flow arrangement, cf. Garstecki et al. (2005), Dessimoz et al. (2008), Salim et al. (2008), Y-junctions, cf. Kashid and Agar (2007), Tice et al. (2003) or co-flow arrangements, cf. Foroughi and Kawaji (2011), Dreyfus et al. (2003). Also for example a mixing junction with variational cross-section has been proposed, cf. Kaske et al. (2016).

The residence-time unit, subsequent to the generation unit, ensures the residence time for the desired process operations, involving mass transfer in the present context. In the present contribution, a straight capillary tube with circular cross-section of diameter d is present, also representing the most common appearance so far, e.g. used by Irandoust et al. (1992), Bercic and Pintar (1997), Dummann et al. (2003), Kashid and Agar (2007), Ghaini et al. (2010), or Sotowa (2014). Also other geometrical channels arrangements such as meandering, e.g. Dummann et al. (2003), Dessimoz et al. (2008), Okubo et al. (2008), or helical, cf. Kurt et al. (2016) channel arrangements or even more complex structures, cf. Aoki et al. (2011), have been used. Further, different cross-sections, such as rectangular, cf. Burns and Ramshaw (2001), Okubo et al. (2008), Dessimoz et al. (2008), or trapezoidal shapes, e.g. Kashid (2011), have been used.

Downstream exists the separation unit, where the splitting of the two-phase flow into single fluid streams is performed. Both streams are collected in storage vessels or used for subsequent process operations. Tsaoulidis (2015) and Scheiff et al. (2011) summarize the different mechanisms for the phase separation to gravity, centrifugal forces, and wetting. The flow separation by gravity and centrifugal forces need longer time scales than using capillary or wetting forces.

In operation two immiscible phases are fed at constant volumetric flow rates of the continuous or the disperse phase $\dot{V}_c$ and $\dot{V}_d$ into the mixing junction. The generation of the multiphase flow is passively controlled by the ratios of acting forces. The slug flow is transported through the residence-time unit with a total volumetric flow rate of $\dot{V}_{tot} = \dot{V}_d + \dot{V}_c$ and separated at the end of the reactor. The phases act as solvents for solutes $\mathcal{A}$ and $\mathcal{B}$, with the initial concentrations $c_{r,\mathcal{A}}^0$ and $c_{e,\mathcal{B}}^0$. The transfer process is induced as the solvents get into contact, the actual driving concentration difference $\Delta c_{\mathcal{A}}$ is decreased along the reactor axis, corresponding to a mass-transfer time τ_m, with actual mass flux $\dot{c}_{r,\mathcal{A}}^{IF,\tau_m}$ at the free interface, and the transfer process halts as the solvents are completely separated, see figure 1.3. The overall process is characterized by the mean-logarithmic driving concentration difference $\Delta c_{\mathcal{A},ln}$ and the interfacial mass flux $\dot{c}_{r,\mathcal{A}}^{IF,\tau_m}$.

Slug flow

The slug flow is one of four stable flow pattern occurring in micro channels, cf. Dreyfus et al. (2003). It is defined as regular laminar flow of alternating segments, with a length-to-diameter-ratio bigger than one, of two immiscible fluid phases at comparable volumetric flow rates, that is dominated by interfacial tension while the continuous phase wets the capillary walls and encloses the disperse phase completely, considering a wall film and the occurrence of shear-induced vortices, cf. Köhler and Cahill (2014), as introduced in figure 1.1.

The occurrence of the slug flow depends on the ratio of acting forces during the generation process. In particular, it is influenced by the geometry of the mixing element and the flow channel in conjunction with the flow parameters of the two-phase system, cf. Christopher and Anna (2007). The flow regime inside a micro channel can be expected to be laminar, cf. Jensen (1999), Günther and Jensen (2006), or Kashid et al. (2015). Further, unambiguous wetting of the fluid phases at the channel walls is present, cf. Wegmann and von Rohr (2006), i.e. a defined separation into continuous and disperse phase is present, cf. Zorin and Churaev (1992). Also configurations are known where both fluids wet the channel walls, cf. Che et al. (2011),

that are not further considered here. Due to the small diameter and the related large interfacial curvatures, the influence of gravity is rather weak, cf. Bretherton (1960), Kreutzer et al. (2005b), Jovanovic (2011). Hence, the flow behavior is governed by the ratio of viscous and interfacial forces, cf. Afkhami et al. (2011), captured by the capillary number

$$Ca = \frac{\overline{w}_z \, \mu}{\sigma}. \tag{1.2}$$

The dimensionless group relates here the average channel velocity $\overline{w}_z$, characterizing the two phase flow, cf. Suo and Griffith (1964), to the dynamic viscosity μ and the interfacial tension σ. The average channel velocity can be calculated to $\overline{w}_z = \dot{V}_{tot}/\mathbf{A}^D$, with the total volumetric flow rate $\dot{V}_{tot} = \dot{V}_c + \dot{V}_d$ and the cross-sectional area $\mathbf{A}^D$ of the capillary. A threshold of $Ca_{max} \sim 10^{-1}$ for the occurrence of the slug flow, cf. Kashid et al. (2015), results from the required dominance of the interfacial tension. Larger capillary numbers, e.g. at larger volumetric flow rates lead to a break up of the multiphase flow, since the interfacial tension does not dominate anymore, cf. Zhao et al. (2006). A typical magnitude of the capillary number $Ca \sim 10^{-2}$ can be assumed for the slug flow, according to Dittmar (2015), Afkhami et al. (2011), Sarrazin et al. (2006), all in good agreement with Baltes et al. (2008). The multiphase flow is obviously stable for lower volumetric flow rates and average channel velocities. Hence, an average volumetric channel velocity of $\overline{w}_z \sim 10^{-2}$ m/s can be derived for liquid/liquid systems as typical value, based on magnitudes for the liquid density of $\varrho \sim 10^3$ kg/m^3, the dynamic viscosity of $\mu \sim 10^{-3}$ kg/(ms), and the interfacial tension of $\sigma \sim 10^{-3}$ kg/s^2, cf. Perry et al. (1997).

The generation process is sketched in figure 1.4a, based on a T-junction mixing element in a cross-flow arrangement, according to Hoang et al. (2013). The disperse phase enters the axial flow of the continuous phase, is bent into the axial direction, and sheared or squeezed off, cf. de Menech et al. (2008). The ratio of volumetric flow rates

$$\hat{V} = \frac{\dot{V}_d}{\dot{V}_c} \tag{1.3}$$

is in the typical magnitude of $\hat{V} \sim 1$, cf. Christopher and Anna (2007). If the volumetric flow rate of the disperse phase becomes small compared to the volumetric flow rate of the continuous phase, the disperse phase cannot occupy the whole cross section and the flow develops towards a bubbly flow. Changing the ratio into the other direction results in a churn flow, as the wetting of the continuous phase is not maintained throughout the channel, cf. Triplett et al. (1999).

The length of the generated periodic element l_{pe}, with a length of the disperse phase of l_d, depends on the generation process in conjunction with the geometry of the mixing element and the flow parameters. Garstecki et al. (2005), Kreutzer et al. (2005b) or Hoang et al. (2013) for example set up empirical correlations for the dimensionless periodic element length

$$L_{pe} = \frac{l_{pe}}{d}. \tag{1.4}$$

Periodic element lengths in the range of $2d \lesssim l_{pe} \lesssim 10d$ in dependence to the geometric arrangement of the mixing junction are mainly observed. A periodic element length of $L_{pe} \approx 4$ is assumed as typical value here.

The developed slug flow inside the residence-time unit is shown in figure 1.4b. A thin wall film of the continuous phase is present between the disperse and the channel wall with local height $h(z)$ and average height $\overline{h}$, averaged over a length of the wall film l^{WF}, see figure 1.4b.
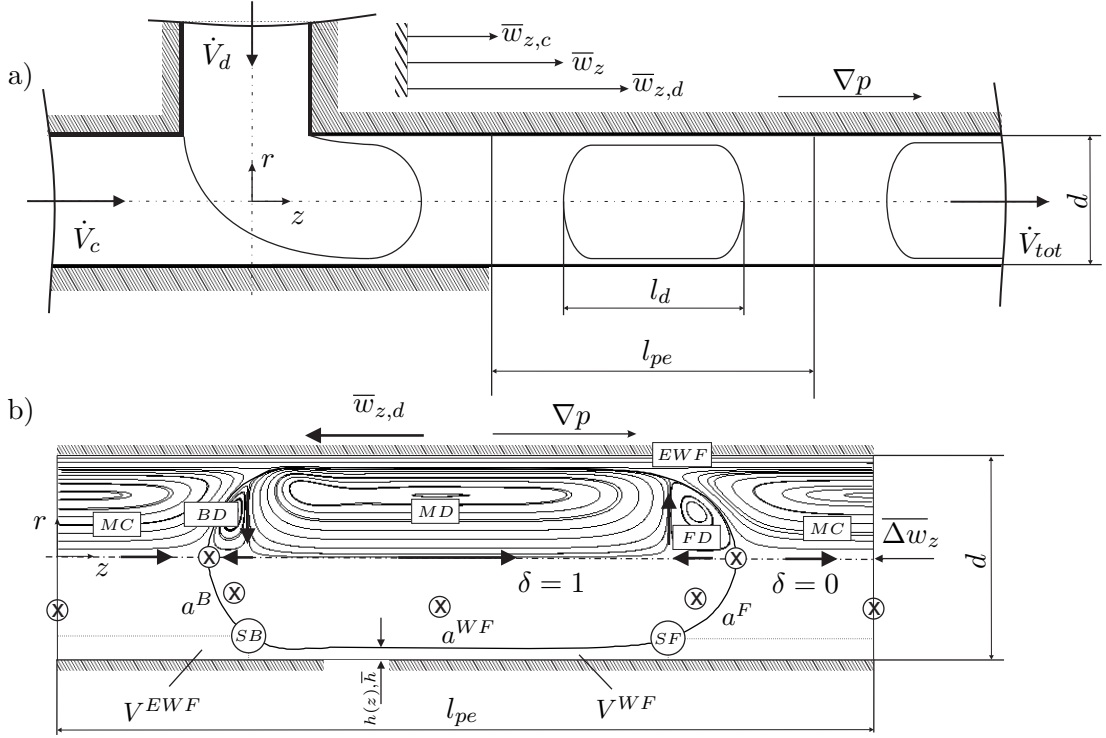
Figure 1.4: Slug-flow pattern: a) Schematic generation of the slug-flow pattern in a T-junction mixing element in cross-flow arrangement, according to Hoang et al. (2013); b) Internal vortex structure for one periodic element based on a frame of reference moving with the dispersed phase, showing the stream-line pattern (upper half) and the singular flow points and the interfacial contour (lower half), emphasizing the positions of the front saddle (SF) point and the back saddle point (SB), according to Dittmar (2015).

Several approaches show, that the wall-film height is strongly related to the capillary number, cf. Wong et al. (1995) or Aussillous and Quéré (2000). Park and Homsy (1984) and Hodges et al. (2004) show, that the most popular correlation, that is set up by Bretherton (1960) for gas/liquid systems, is also valid for liquid/liquid systems with a viscosity ratio $\hat{\mu} = \mu_d/\mu_c \approx 1$. So the dimensionless average wall-film height $\overline{H}$, averaged over the wall-film length l^{WF}, can be calculated for low capillary numbers to

$$\overline{H} = \frac{\overline{h}}{d} = \frac{1}{d}\frac{1}{l^{WF}}\int_{l^{WF}} h \; dz \approx 0.669 \; (Ca_d)^{2/3}. \tag{1.5}$$

Extrapolation of the correlation for a capillary number of $Ca_d = 10^{-2}$ shows that the wall film occupies about 5% of the capillary diameter d.

The disperse flow structure results further in unequal phase velocities, cf. Oertel (2008). The disperse phase travels with a larger velocity $\overline{w}_{z,d}$ than the continuous phase $\overline{w}_{z,c}$, while the average channel velocity $\overline{w}_z$ is in between them, sketched in figure 1.4a. The volume fraction of the disperse phase ζ_d relates the average channel velocity to the phase velocities, cf. Oertel (2008), to

$$\overline{w}_z = \zeta_d\overline{w}_{z,d} + (1 - \zeta_d)\overline{w}_{w,c}, \tag{1.6}$$

$$\zeta_d = \frac{1}{V_{ref}}\int_{V_{ref}} \delta\left(r, \varphi, z, \tau\right) dV, \tag{1.7}$$

$$\overline{w}_{z,p} = \frac{1}{V_{ref}} \int_{V_{ref}} w_{z,p} \; dV. \qquad (1.8)$$

The volume fraction of the disperse phase is here defined by a phase function $\delta\left(r,\varphi,z,\tau\right)$, inside a reference volume V_{ref}, i.e. the reactor or a periodic element. Here, $\delta = 1$ is in the disperse phase and $\delta = 0$ in the continuous phase and the average phase velocity $\overline{w}_{z,p}$ with $p = c, d$, also shown figure 1.4b. The volumetric flow rates of the phases and the average phase velocities are further related by the volume fraction, cf. Oertel (2008), to

$$\hat{V} = \frac{\zeta_d}{1 - \zeta_d} \frac{\overline{w}_{z,d}}{\overline{w}_{z,c}}. \qquad (1.9)$$

Charles (1963) shows, that the average wall-film thickness $\overline{h}$ is the key parameter for the description of the ratio of the phase velocities and the velocity difference $\overline{\Delta w_z} = \overline{w}_{z,d} - \overline{w}_z$. The correlation approach by Fairbrother and Stubbs (1935) is based on the capillary number of the disperse phase, working also for liquid/liquid systems, cf. Taylor (1961), given to

$$\Delta \overline{W}_z = \frac{\overline{w}_{z,d} - \overline{w}_z}{\overline{w}_z} = Ca_d^{1/2}. \qquad (1.10)$$

It can be used to estimate the velocity difference in dimensionless form. For a capillary number of $Ca_d = 10^{-2}$, the disperse phase velocity is about 10% higher than the average channel velocity.

Following from continuity, the different phase velocities cause unequal residence times of the disperse and the continuous phase in a micro channel. This causes axial dispersion inside the continuous phase. The magnitude of the relative flux through the wall film between two continuous segments is characterized by the velocity difference $\overline{\Delta w_z}$, cf. Dittmar (2015). The investigations of Thulasidas et al. (1999), Muradoglu et al. (2007), Gekle (2017), Pedersen and Horvath (1981), and Arsenjuk et al. (2016), show all a strong dependence to the average channel velocity, directly related to equation 1.10. In general the effect appears to be weak compared to other two-phase flows in micro channels.

The flow topology of a periodic element in steady-state is shown in figure 1.4b, following Dittmar (2015), for a flow channel with circular cross-section and a frame of reference moving with the velocity of the disperse phase. The shown flow topology is in good accordance to Miessner et al. (2008), Hazel and Heil (2002), or Afkhami et al. (2011). The disperse flow structure and the related difference of the phase velocities results in the shown shear-induced flow structure in relation to the low capillary number, cf. Taylor (1961) or Magnaudet et al. (2003). Hence, the disperse phase is governed by three toroidal vortices, a front vortex (FD), a main vortex (MD), and a back vortex (BD), see upper half of figure 1.4b. The continuous phase consists of one closed flow structure, i.e. the toroidal main vortex (MC), and the flow through the extended wall film (EWF). The shown directions of rotation of the vortices result from the kinematic constrictions in relation to the moving wall in the frame of reference. The flow topology can be described by its singular points (X) that appear in the vortex centers and at the free interface, cf. Dittmar (2015), see lower half of figure 1.4b. The positions of the saddle points (SF, SB) are especially emphasized here, that separate the closed flow structures of both phases. Dittmar (2015) shows further, that the appearance of the flow topology is mainly controlled by the capillary number of the continuous phase Ca_c and the viscosity ratio $\hat{\mu} = \mu_d/\mu_c$. For large capillary numbers, the ratio of vortices can change and the vortex in the back can become weak, cf. Taylor (1923) or Miessner et al. (2008). Further the main vortex can decompose into two sub-vortices, e.g.

shown by Scheiff (2015) and Dittmar (2015).

The appearance of the free interface, also shown in the lower half of figure 1.4b, is directly related to the flow topology, cf. Dittmar (2015). Bretherton (1960) separates the interface into five portions based on its geometrical appearance of the free interface. The portions consist of a straight wall film, spherical caps, and transition regions. In contrast, Thulasidas et al. (1997) uses the flow topology to separate the interface into wall film and caps, defined by the saddle points at the front (SF) and the back (SB) of the free interface, see lower half figure 1.4b. The idea is taken over by Kreutzer et al. (2005a), Taha and Cui (2006) and Roudet et al. (2011) for the definition of the wall film and the wall-film portion of specific free interface a^{WF} and the caps, consisting of the front a^F and the back a^B, as well as the corresponding volume of the wall film V^{WF}, in between the saddle points, and the extended wall film V^{EWF}. For very low capillary numbers, i.e. $Ca_c \lesssim 10^{-3}$, the free interface can further be approximated by a cylindrical body with spherical caps, proposed for gas/liquid systems by Giavedoni and Saita (1999) and being in good relation to Bretherton's theory. In this case the saddle points (SF, SB) of the flow topology coincide with the transitions of the cylindrical body to the spherical caps in good approximation. The position of the saddle points can also be used to define the length of the wall film l^{WF}.

The flow topology can be influenced by surface active agents or strong temperature gradients resulting in tangential stresses at the free interface, called Marangoni stresses, cf. Marangoni (1871). Anna (2016) summarizes the related effects, showing especially influences to the generation and the flow topology. The effect is not further considered here.

Volumetric mass-transfer coefficient

The mass transfer at the free interface is a transient process that is driven by the actual concentration difference $\Delta c_{\mathcal{A}}$ and controlled by molecular diffusion in the liquid/liquid system. The process is described from the basic approach, see e.g. Lewis and Whitman (1924), to

$$\dot{c}_{r,\mathcal{A}}^{IF} = Ka\Delta c_{\mathcal{A}}. \tag{1.11}$$

The actual mass flux $\dot{c}_{r,\mathcal{A}}^{IF}$ is related to the actual driving concentration difference $\Delta c_{\mathcal{A}}$ by a actual volumetric mass-transfer coefficient Ka, see figure 1.5. The volumetric mass-transfer coefficient itself is the product of the actual-overall mass-transfer coefficient K and the specific interfacial area a. The specific interfacial area $a = A/V_r$ is the ratio the absolute interfacial area A to the total volume of the raffinate solvent V_r. The actual-overall mass-transfer coefficient K summarizes the mass-transfer coefficients of both solvents, i.e. the raffinate and the extract solvent β_r and β_e, and the distribution coefficient $m_{\mathcal{A}}$, that describes the ratio of the concentrations at the free interface, and the volume fraction ζ_r, compare equation 1.8, here all referenced to the raffinate solvent, given to

$$K = \frac{1}{\frac{1}{\beta_r} + \frac{1}{m_{\mathcal{A}}\beta_e}}. \tag{1.12}$$

The presence of Marangoni stresses, due to surfactants and concentration, temperature gradients, or due to a chemical reaction, can influence the transfer process and therefore the transfer coefficients on either side of the free interface, cf. Marangoni (1871), Scriven and Sterling (1960), or Doraiswamy and Sharma (1984). Further, additional resistances to mass transfer may appear at the free interface, cf. Scriven (1960). The overall mass-transfer coefficient and its value
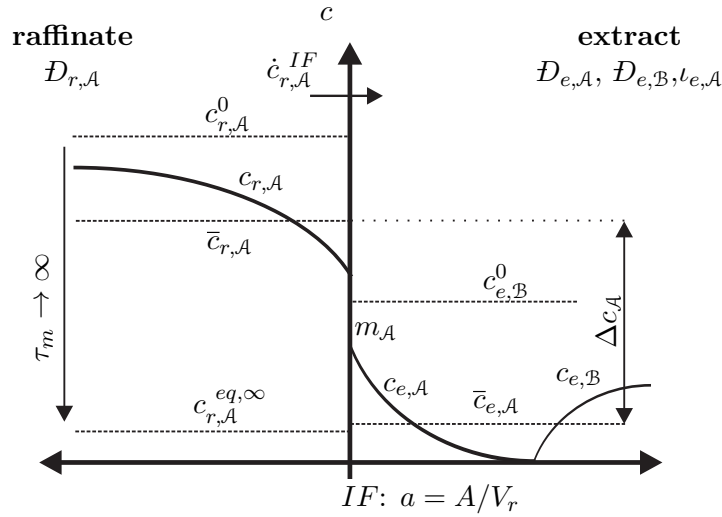
Figure 1.5: Schematic mass transfer at the free interface: Showing relevant parameters for the description of the volumetric mass-transfer coefficient, including the influence of an instantaneous second-order chemical reaction, adapted from Doraiswamy and Sharma (1984).

depend on the chosen reference for the system description, i.e. the assignment of the solvents to the phases, cf. Russell et al. (2008). Here, throughout the thesis, the raffinate solvent is chosen as reference solvent based on a concentration dependent description.

Some investigations suggest the description of the overall mass transfer coefficient by addition of the separately derived transfer coefficients in both solvents, based on investigations of binary mass-transfer systems, see e.g. Skelland (1985). This approach is not working in general in the transient mass-transfer scenario, cf. Juncu (2001), and only theoretically for uniform concentration distributions at the free interface. These appear for the limiting cases of a very large ratio of convection and diffusion or a stagnant fluid phase, i.e. no convection, as shown for the investigation of the transient mass transfer within spherical droplets, cf. Schulze (2007) or for the limiting cases of $\hat{D}_A \to \infty$ rather $\hat{D}_A \to 0$ with $\hat{D}_A = D_{e,A}/D_{e,A}$. The ratio of convection and diffusion in the present application can be estimated by means of the magnitudes of average channel velocity $\overline{w}_z$, the diameter d and the diffusion coefficient in liquids D, being in the magnitude of $D \sim 10^{-9}\mathrm{m}^2/\mathrm{s}$, cf. Lo (1991). The ratio appears as Péclet number to

$$Pe = \frac{\overline{w}_z d}{D}. \tag{1.13}$$

The ratio can be estimated to $Pe \sim 10^3$ assuming the before derived typical values. Hence, a convection dominated mass-transfer system is present, with inhomogeneous time-dependent concentration fields inside both solvents, cf. Harries et al. (2003), Kashid et al. (2007a), or Ghaini et al. (2010).

The driving concentration difference in the conjugate system appears as difference of the average concentrations in the raffinate solvent $\overline{c}_{r,A}$ and the extract solvent $\overline{c}_{e,A}$, again referenced to the raffinate solvent with the distribution coefficient m_A, given to

$$\Delta c_A = \overline{c}_{r,A} - \frac{\overline{c}_{e,A}}{m_A}. \tag{1.14}$$

Here, the volumetric average concentration of solute i, with $i = \mathcal{A}, \mathcal{B}$, in an assigned reference volume of a solvent $V_{s,ref}$, with $s = r, e$, see figure 1.5, is defined to

$$\bar{c}_{s,i} = \frac{1}{V_{s,ref}} \int_{V_{s,ref}} c_{s,i} \, dV. \tag{1.15}$$

The presence of a chemical reaction influences the average concentration of solute $\mathcal{A}$ inside the extract solvent. The reaction rate $\iota_{e,\mathcal{A}} = \partial c_{e,\mathcal{A}}/\partial \tau_m$, cf. Levenspiel (2007), describes the temporal consumption of solute $\mathcal{A}$ inside the extract solvent. The influence of a chemical reaction is therefore also covered by equation 1.14. The enhancement factor

$$\mathcal{E} = \frac{ka(\iota_{e,\mathcal{A}} > 0)}{ka(\iota_{e,\mathcal{A}} = 0)} \tag{1.16}$$

relates the volumetric mass-transfer coefficient with chemical reaction $ka(\iota_{e,\mathcal{A}} > 0)$ to the pure physical volumetric mass-transfer coefficient $ka(\iota_{e,\mathcal{A}} = 0)$, cf. Hatta (1932). The value is a measure for the influence of a chemical reaction to the transfer process.

The relative progress of the time-dependent transfer process is captured by the extract rate $F_{\mathcal{A}}$ of solute $\mathcal{A}$, cf. Clift et al. (1978), relating the actual transferred amount of mass to the maximum transferable amount of mass, cf. Russell et al. (2008), i.e.

$$F_{\mathcal{A}} = \frac{c_{r,\mathcal{A}}^0 - \bar{c}_{r,\mathcal{A}}}{c_{r,\mathcal{A}}^0 - c_{r,\mathcal{A}}^{eq,\infty}},$$
$$c_{r,\mathcal{A}}^{eq,\infty} = \frac{c_{r,\mathcal{A}}^0}{Q} \cdot \max\left[1 - \frac{1}{\psi}; 0\right]. \tag{1.17}$$

Here, $c_{r,\mathcal{A}}^{eq,\infty}$ is the equilibrium concentration in dependence to a chemical reaction for $\tau_m \to \infty$, that can be derived by a mass balance. The volumetric quotient $Q = 1 + \left[(1 - \zeta_r)/(\zeta_r m_{\mathcal{A}})\right]$ and the excess factor $\psi = \left[(\nu_{\mathcal{B}} c_{r,\mathcal{A}}^0)\right]/(c_{e,\mathcal{B}}^0 \nu_{\mathcal{A}})(\zeta_r/1 - \zeta_r)$ appear. The excess factor relates the chemical reservoir of solutes $\mathcal{A}$ and $\mathcal{B}$, taking the initial concentrations $c_{r,\mathcal{A}}^0$ and $c_{e,\mathcal{B}}^0$, the stochiometric coefficients $\nu_{\mathcal{A}}$ and $\nu_{\mathcal{B}}$ and the volume fraction ζ_r into account.

As described in before, see two-phase micro capillary reactor, the mass flux $\dot{c}_{r,\mathcal{A}}^{IF}$ and the driving concentration difference $\Delta c_{\mathcal{A}}$ decrease along the reactor axis, i.e. with increasing mass-transfer time τ_m. Mass transport is a transient process. If the local concentration distribution and their temporal evolutions inside the solvents are available, the volumetric mass-transfer coefficient can directly be evaluated from the mass flux $\dot{c}_{r,\mathcal{A}}^{IF}$ at the interface and the average solvent concentrations rather the local mass flux at the free interface to

$$ka = \frac{\dot{c}_{r,\mathcal{A}}^{IF,\tau_m}}{\Delta c_{\mathcal{A},ln}} = \frac{1}{\tau_m} \int_{\tau_m} \frac{\dot{c}_{r,\mathcal{A}}^{IF}}{\Delta c_{\mathcal{A}}} \, d\tau_m = \frac{1}{\tau_m} \int_{\tau_m} Ka \, d\tau_m. \tag{1.18}$$

Examples for this approach can be found for spherical rising or falling droplets, cf. Kronig and Brink (1951) or Newman (1931), and in particular for the slug flow, compare Irandoust and Andersson (1989), Harries et al. (2003), Shao et al. (2010), Sobieszuk et al. (2011) or Tsaoulidis and Angeli (2015), evaluating the mass flux at the free interface based on Fick's law, cf. Fick (1855).

Further, the volumetric mass-transfer coefficient can be derived from a mass balance at the co-current mass contactor. The assignment of the raffinate solvent to the continuous phase is used exemplary for the description of the volumetric mass-transfer coefficient, as shown in figure 1.6.

It is useful to reference the driving concentration difference $\Delta c_{\mathcal{A}}$ to the equilibrium concentration $c_{r,\mathcal{A}}^{eq,\tau_m}$, in dependence to the progress of a chemical reaction at mass-transfer time τ_m, adapted from Russell et al. (2008), to

$$\Delta c_{\mathcal{A}} = Q\left(\bar{c}_{r,\mathcal{A}} - c_{r,\mathcal{A}}^{eq,\tau_m}\right), \tag{1.19}$$

$$c_{r,\mathcal{A}}^{eq,\tau_m} = \frac{1}{Q}\left(c_{r,\mathcal{A}}^0 - \frac{c_{e,\mathcal{A}}^{\iota,\tau_m}}{m_{\mathcal{A}}}\right), \tag{1.20}$$

$$\bar{c}_{e,\mathcal{A}}^{\iota,\tau_m} = \int_{\tau_m} \frac{1}{V_e}\int_{V_e}\iota_{e,\mathcal{A}}\ dV d\tau_m. \tag{1.21}$$

The ratio $c_{r,\mathcal{A}}^0/Q$ represents the equilibrium concentration for the pure physical mass-transport system, while the second term $c_{e,\mathcal{A}}^{\iota}/\left(Qm_{\mathcal{A}}\right)$, captures the influence of a chemical reaction to the transfer process, i.e. a change of the physical equilibrium concentration in dependence to a chemical reaction. To derive the volumetric mass-transfer coefficient the change of driving
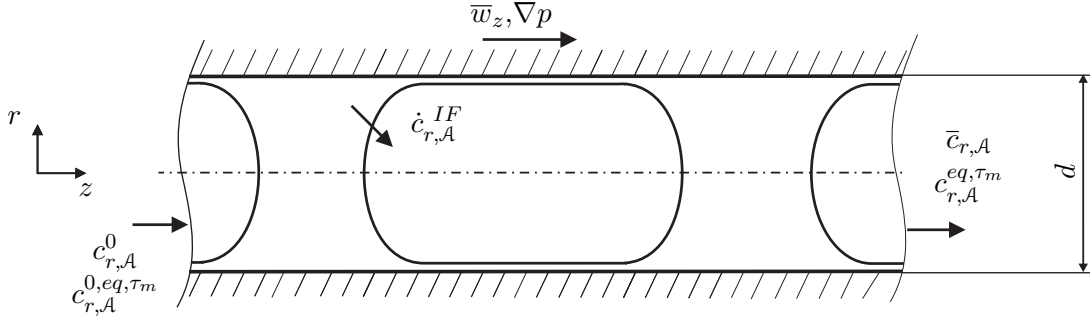
Figure 1.6: Mass balance at the co-current mass contractor with assignment of the raffinate solvent to the continuous phase.

concentration differences at the inlet $\Delta c_{r,\mathcal{A}}^0 = Q\left(c_{r,\mathcal{A}}^0 - c_{r,\mathcal{A}}^{0,eq,\tau_m}\right)$ and current position, i.e. the current mass-transfer time $\Delta c_{r,\mathcal{A}}^{\tau_m} = Q\left(\bar{c}_{r,\mathcal{A}} - c_{r,\mathcal{A}}^{eq,\tau_m}\right)$, are balanced with the mean mass flux at the free interface $\dot{c}_{r,\mathcal{A}}^{IF,\tau_m} = (1/\tau_m)\left(\bar{c}_{r,\mathcal{A}} - c_{r,\mathcal{A}}^0\right)$, transferred during the mass-transfer time τ_m. For a reactor length l_{re} the mass-transfer time is calculated to $\tau_m = \mathcal{Z}/\overline{w}_z$, while $\mathcal{Z}$ represents the actual position along the reactor axis. Following, assuming constant volumetric properties, the volumetric mass-transfer coefficient, cf. Russell et al. (2008), Zhao et al. (2006), Kashid et al. (2011), or Susanti et al. (2016), appears to

$$ka = \frac{Q}{\tau_m}\frac{\bar{c}_{r,\mathcal{A}} - c_{r,\mathcal{A}}^0}{\Delta c_{\mathcal{A},ln}}, \quad \text{with}\quad \Delta c_{\mathcal{A},ln} = \frac{\left(c_{r,\mathcal{A}}^{0,eq,\tau_m} - c_{r,\mathcal{A}}^0\right) - \left(c_{r,\mathcal{A}}^{eq,\tau_m} - \bar{c}_{r,\mathcal{A}}\right)}{\ln\left(\frac{c_{r,\mathcal{A}}^{0,eq,\tau_m} - c_{r,\mathcal{A}}^0}{c_{r,\mathcal{A}}^{eq,\tau_m} - \bar{c}_{r,\mathcal{A}}}\right)}. \tag{1.22}$$

Here, $c_{r,\mathcal{A}}^0$ and $c_{r,\mathcal{A}}^{0,eq,\tau_m}$ are the initial concentrations at the inlet, rather the beginning, and $\bar{c}_{r,\mathcal{A}}$ and $c_{r,\mathcal{A}}^{eq,\tau_m}$ are the corresponding concentrations at the actual position, rather mass-transfer time τ_m, and $\Delta c_{\mathcal{A},ln}$ is the driving logarithmic-mean concentration difference. The approach captures the mass-transfer inside the reactor, considering the influence of axial dispersion due to the unequal residence times of the solvents in the micro reactor result in unequal equilibrium concentrations $c_{r,\mathcal{A}}^{0,eq,\tau_m} \neq c_{r,\mathcal{A}}^{eq,\tau_m}$. Neglecting the effect of axial dispersion and prescribing ideal plug-flow behavior, i.e. $c_{r,\mathcal{A}}^{0,eq,\tau_m} = c_{r,\mathcal{A}}^{eq,\tau_m}$, is in common practice, cf. Dummann et al. (2003), van Baten and Krishna (2004), Kashid et al. (2007b), Di Miceli Raimondi et al. (2008), Dessimoz et al. (2008), or Kurt et al. (2016), since its influence to the evaluation of the volumetric mass-

transfer coefficient appears to be weak, cf. van Baten and Krishna (2004) and Plouffe et al. (2016). Accordingly, the volumetric mass-transfer coefficient simplifies to

$$ka = \frac{Q}{\tau_m} \ln \left(\frac{c_{r,\mathcal{A}}^{eq,\tau_m} - c_{r,\mathcal{A}}^0}{c_{r,\mathcal{A}}^{eq,\tau_m} - \bar{c}_{r,\mathcal{A}}} \right). \tag{1.23}$$

The efforts evaluating the mass-transfer performance have been summarized mainly by the reviews of Kashid et al. (2011), Sotowa (2014), Sobieszuk et al. (2012), and Assmann et al. (2013). Mvolumetric mass-transfer coefficients that are reported are mainly in the range of $10^{-2} \lesssim ka \lesssim 1/s$, see e.g. Burns and Ramshaw (2001), Kashid et al. (2007b), Fries et al. (2008), Kashid et al. (2011), Jovanovic (2011), Kaske et al. (2016) or Susanti et al. (2016). Also extreme values up to $ka \approx 10/s$ can appear for modified systems, cf. Assmann and von Rohr (2011), or very short mass-transfer times, cf. Zhao et al. (2007). The transfer rate consists of a magnitude of the specific interfacial areas of $10^3 \lesssim a \lesssim 10^5/m$, cf. Yue et al. (2007), Di Miceli Raimondi et al. (2008), Ghaini et al. (2010), Jovanović et al. (2011) and the related mass-transfer coefficients $10^{-5} \lesssim k \lesssim 10^{-3}m/s$, cf. Burns and Ramshaw (2001), Kashid et al. (2007b), Ghaini et al. (2010), Sobieszuk et al. (2011).

1.3.2 Local mass transfer

Only a few investigations have been performed so far to investigate the local mass transfer at the free interface and the underlying mass transport in detail. Firstly, Irandoust and Andersson (1989) derive from numerical simulations, that the wall film provides the largest contribution to the mass transfer in a gas/liquid flow, related to the flow topology and the shear induced vortices. Later, Irandoust et al. (1992) set up an idealized theoretical model. The interface of the slug flow is idealized to a cylindrical body with spherical caps. The model confirms the previously observed behavior for short mass-transfer times. In contrast, Bercic and Pintar (1997) derive that the wall film plays a subordinated role due to accumulation of mass inside the wall film, that hinders the local mass transfer in a gas/liquid slug flow. Accordingly, the main amount of mass is transferred at the cap regions. A computational model is set up by van Baten and Krishna (2004) to investigate the mass transfer within a gas/liquid slug flow with idealized interfacial contour in a circular capillary. The variation of several parameters suggests, that the liquid film amounts up to $60 - 80\%$ of the overall volumetric mass-transfer coefficient. Vandu et al. (2005) set up a correlation that takes only the contribution of the wall film into account. Good agreement with experimental data is obtained. Hence, the authors suggest that the wall film provides the main portion of the volumetric mass-transfer coefficient. For a gas/liquid slug flow Pohorecki (2007) traces back the role of the wall film to the local mass-transfer conditions. If the convective transport inside the wall film is small compared to the radial transport by diffusion, mass accumulates inside the wall film and hinders the mass-transfer locally, since the driving concentration difference decreases locally. Dessimoz et al. (2008) and Roudet et al. (2011) neglect the contribution of the wall film to the mass transfer, due to the small total volume of the wall film, if compared with the continuous phase. They argue, that a „quick saturation" of the wall film should be the consequence. Di Miceli Raimondi et al. (2008) use numerical simulations to investigate the transfer in a liquid/liquid slug flow within a square micro-channel. Results show a large concentration in the wall film that even overshoots the reactive equilibrium concentration for long contact times. The time scale for accumulation or exhaustion in the wall film can be much shorter than for the overall process. Ghaini (2011) investigates the effective interfacial area for mass transfer in the liquid/liquid

slug flow using fluorescence microscopy in circular capillaries. The results suggest that a large amount of mass is transferred through the wall film between the solvent bulks. Liu and Wang (2011) investigate the mass transfer in a gas/liquid slug flow for an idealized shape of the disperse slug and for a circular cross-section by means of numerical simulation. Results show, that the mass-transfer is represented by the portion of the wall film in good approximation, independent of all combinations of model parameters. Hence, the contributions of the cap regions remains small in all cases. Sobieszuk et al. (2011) investigate the mass transfer in a gas/liquid slug flow experimentally, using Danckwert's chemical method. The interfacial area is derived based on the assumption of an idealized shape of the disperse phase. Results show, that major amount of mass is transferred at the wall-film portion of the free interface. Tan et al. (2012) suggest that the flow topology is responsible for the local distribution of the mass transfer at the free interface. A long wall film, i.e., long periodic elements and large volume fractions result in a hindered mass transfer in the wall film.

To summarize, the free interface and the flow topology have a strong influence onto the spatial distribution of the volumetric mass-transfer coefficient at the free interface. The local mass transfer, the underlying mass transport, and especially the contribution of the portion of the free interface related to the wall film within the slug flow are not understood in detail so far, also emphasized in several reviews, c.f. Kashid et al. (2011), Sobieszuk et al. (2012) or Sotowa (2014). The spatial distribution of the volumetric mass-transfer coefficient has not been investigated in detail so far. The spatial distribution of the volumetric mass-transfer coefficient at the free interface is probably dominated by the local transport conditions inside the wall film in conjunction with the large portion of the area of the free interface. The free interface can be separated into portions of the free interface a^P, with portions $P = F, WF, B$ designating the front cap (F), the wall film (WF), and the back cap (B), for the evaluation of the contribution of the caps and the wall film, compare section 1.3.1.

For the investigation of the contribution of the wall film and the caps to the mass transfer the interfacial portion of the volumetric mass-transfer coefficient $(ka)^P$ can be used, defined to

$$\int_{a^P} d(ka) = (ka)^P. \tag{1.24}$$

The sum of the portions has to correspond to integral of the local volumetric mass-transfer coefficient over the whole specific interface, being the volumetric mass-transfer coefficient, i.e.

$$(ka)^F + (ka)^{WF} + (ka)^B = \int_a \frac{d\dot{c}_{r,\mathcal{A}}^{IF,\tau_m}}{\Delta c_{\mathcal{A},ln}} \, da = ka. \tag{1.25}$$

Furthermore, the transport conditions inside the wall film and the appearance of the free interface can be estimated from the typical values of flow and mass transport, compare section 1.3.1, based on an idealized interfacial contour, as summarized in figure 1.7.

Accordingly, the wall film (WF) and its interfacial portion, defined in between the saddle points (SF,SB) of the flow topology, represents about $a^{WF}/a = 68\%$ of the interfacial area, indicating a high potential for mass transfer, while the caps (F,B) only occupy a portion of about $(a^F + a^B)/a = 32\%$. The wall film describes here the volume between the saddle points, while extended wall film (EWF) represents overall volume of the wall film along the axial direction. The transport conditions inside the wall film can be characterized by the local ratio of convection
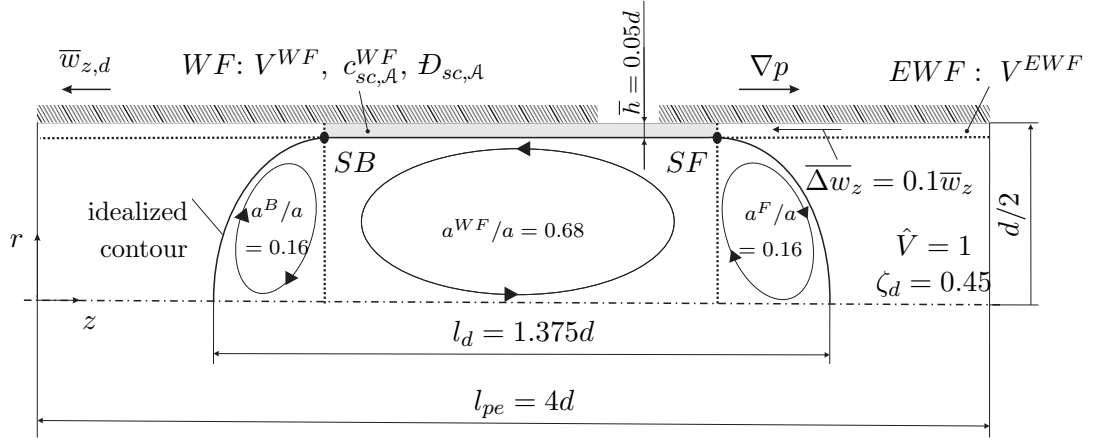
Figure 1.7: Estimation of the transport conditions inside the wall film, based on an idealized interface contour and the derived typical values of the slug-flow micro-capillary reactor, in half section.

and diffusion, described by a wall-film Péclet number

$$Pe^{WF} = \frac{\overline{\Delta w_z}\,\overline{h}}{\mathcal{D}_{sc,\mathcal{A}}}. \tag{1.26}$$

Here, the average wall-film height $\overline{h}$ is used as characteristic length, the relative flow is captured by the velocity difference $\overline{\Delta w_z}$, and $\mathcal{D}_{sc,\mathcal{A}}$ is the diffusion coefficient of solute $\mathcal{A}$ within the solvent, that is assigned to the continuous phase. Assuming the typical values, derived in section 1.3.1, the magnitude of the wall-film Péclet number can be estimated to $Pe^{WF} \sim 10^1$. Hence, the local ratio of convection and diffusion is about two orders of magnitude smaller than the global ratio, estimated to $Pe \sim 10^3$. This indicates a more pronounced influence of diffusion within the wall film. Accumulation or depletion of mass inside the wall film may appear, in dependence to the direction of mass transfer at the free interface. A hindered mass transfer results in small local volumetric mass-transfer coefficients at the wall-film portion of the free interface. Additionally, the average concentration of solute $\mathcal{A}$ of the solvent, that is assigned to the continuous phase, inside the wall film $\overline{c}_{sc,\mathcal{A}}^{WF}$, related to the volume of the wall film V^{WF}, has to deviate from the average solvent concentration $\overline{c}_{sc,\mathcal{A}}$. The deviation can be evaluated by means of the relative wall-film concentration

$$\Gamma = \frac{1}{\tau_m}\int_{\tau_m}\frac{\overline{c}_{sc,\mathcal{A}}^{WF}}{\overline{c}_{sc,\mathcal{A}}}d\tau_m, \tag{1.27}$$

representing the mean concentration inside the wall film compared to the average concentration in the solvent that is assigned to the continuous phase. A strict definition of a hindered mass transfer is not present in literature. Di Miceli Raimondi et al. (2008) compares the wall film concentration to the equilibrium concentration for long mass-transfer times, while Bercic and Pintar (1997), Kreutzer et al. (2005a), and Jovanovic (2011) argue with a saturation concentration.

1.3.3 Direct numerical simulation of mass transfer at free interfaces

The investigation of the spatially-resolved transfer process induces the need of direct numerical simulation of the mass transfer at a free interface. In general, Eulerian and Lagrangian methods can be distinguished for the numerical description of a free interface, reviewed in the following regarding their potential to capture the local mass transfer based on the case of mass transfer

from a spherical droplet rising at terminal velocity in creeping flow.

Eulerian methods

Within Eulerian methods fixed positions in space are used for the description of the fluid volumes, see figure 1.8a, cf. Wörner (2012). The spatial distribution and the temporal evolution of the free interface is described by some kind of marker or phase function $\delta(r, \varphi, z, \tau)$, that is transported through space, while the function values indicate the phases, i.e. $\delta = 1$ for the disperse phase and $\delta = 0$ for the continuous phase. The position of the free interface is implicitly derived from the position of the phase volumes, where the phase function transits from one to another value. Accordingly, the description of a two-phase system is decoupled from the underlying computational mesh, based e.g. on a Cartesian mesh with rectangular cell topology, cf. Rusche (2002). At the interface also the fluid and transport properties transit from one value to another. Numerically, the handling of a sharp interface with jump transitions of the marker function and the fluid and transport properties appears to be problematic. Hence, it is numerically of advantage to smear all transitions over a short distance normal to the interface, cf. Ferziger and Peric (2008), within an one-field formulation of the governing transport equations, cf. Peskin (2002). This allows e.g. the application of the interfacial pressure jump, cf. Brackbill et al. (1992), or source terms, compare e.g. Özkan et al. (2016) or Marschall et al. (2012), in a stable numerical solution procedure.

The Eulerian approach has in general a strong influence onto the description of the mass transport, since the local transport direction of the mesh is not aligned with the local transport direction of mass at the free interface, illustrated in figure 1.8b. The mesh transport directions are sketched by the normal vectors at the cell faces, generalized to $\vec{n}_{mesh}$, while the local transport directions for mass, given by the flow vector $\vec{u}$ is always tangential to the free interface, and the diffusion vector $\vec{D}$, acts normal to the free interface, from the raffinate into the extract solvent, i.e. here from the disperse into the continuous phase. The misalignment, which can be measured for each cell by

$$\min\left(\vec{n}_{mesh} \cdot \vec{u}\right) \neq 0, \tag{1.28}$$

certainly enhances numerical inaccuracies within any numerical method. The magnitude of the numerical error is proportional to the magnitude of the misalignment, the local concentration gradient $\nabla c_{\mathcal{A}}$, the mass flux $\dot{c}_{r,\mathcal{A}}^{IF}$, and the local edge length of the mesh e, cf. Jasak (1996). In detail, these accuracies are introduced by the discretization of the convective term in the transport equations, cf. Hirsch (2007), enhancing artificially the diffusion, also termed numerical diffusion, cf. Patankar (1980). Accordingly, its influence is especially strong close to the free interface, where steep concentration gradients can be expected. Numerical diffusion can be in the same magnitude as physical diffusion close to the free interface substantially reducing the quality of the numerical transport, cf. Ferziger and Peric (2008). Different techniques, such as high-level discretization of the convective terms, cf. Huh et al. (1986), local mesh refinement, cf. Jasak and Gosman (2000), or coordinate transformations, cf. Ryskin and Leal (1983), have been developed for compensation. Further, the concentration at the free interface is not directly accessible due to the fact that the free interface and the mesh lines do not coincide.

Eulerian methods are also termed volume-tracking methods, cf. Ferziger and Peric (2008), immersed-boundary methods, cf. Peskin (2002), or diffusive-interface methods, cf. Anderson et al. (1998). Most popular methods, emerging from the Eulerian approach are the marker-cell-method, cf. Harlow and Welch (1965), the volume-of-fluid method, cf. Hirt and Nichols (1981),
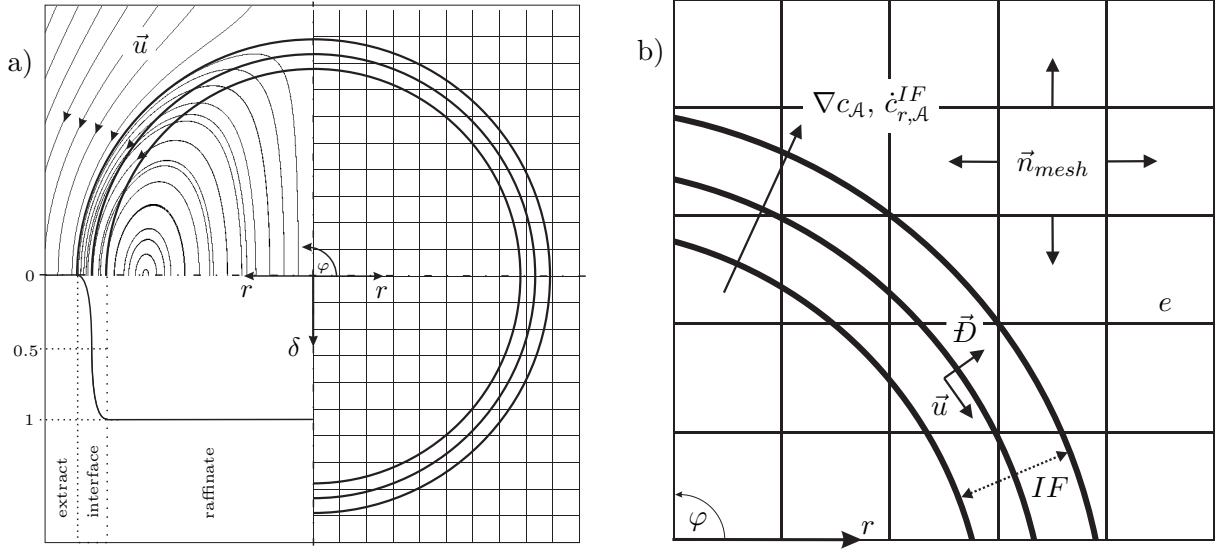
Figure 1.8: Eulerian approach with mass transport at free interfaces: a) Principle sketch of the Eulerian method within a spatially-fixed computational domain, the stream lines and the assignment of the phases by the phase-field function δ; b) Mass transfer at the free interface: poor alignment of the mesh and the mass transport direction in conjunction with a smeared interface.

and the level-set method, cf. Osher and Sethian (1988). Branching into sub-methods can also be observed, cf. Sussman et al. (2007), Tryggvason et al. (2001), or Olsson and Kreiss (2005). Based on the handling of the flow, different approaches have been developed for the interfacial coupling of the concentration fields at the free interface, e.g. Yang and Mao (2005), Alke et al. (2010), or Marschall et al. (2012). Eulerian methods are advantageous for the computational handling of deformation, coalescence and break-up of the phases and computationally cheap, since the transport of the phases is in general decoupled from the underlying mesh structure, cf. Ferziger and Peric (2008). Disadvantages arise from the smeared interface, that provides a low spatial resolution at the free interface and introduces the need for compensation techniques for an acceptable numerical quality of the mass transfer at the free interface, cf. Elgeti and Sauerland (2016).

Lagrangian methods

Within Lagrangian methods the evolution of the free interface is directly described, cf. Wörner (2012), see figure 1.9a. The temporal evolution and the spatial distribution of the phase volumes, represented by separate computational domains, is derived from the known position of the sharp interface, where the fluid and transport properties transit from one value to another, cf. Hirt et al. (1997) and Gueyffier et al. (1999). Again, $\delta = 1$ in the disperse phase and $\delta = 0$ in the continuous phase is prescribed as for Eulerian methods. Accordingly, the interface appears as a boundary for separate phase-fitted computational meshes and the separate fields inside the domains are coupled via interfacial coupling conditions at the free interface, cf. Muzaferija and Perić (1997). A change of the free interface contour results in a related change of the mesh topology and a deformation of the domains, cf. Ryskin and Leal (1984a), Ryskin and Leal (1984b), Ryskin and Leal (1984c), or Tuković and Jasak (2012). The Lagrangian approach shows in general a weak influence on the accuracy of the description of the mass transfer at the free interface. A fixed assignment of the mesh cells to the phases results in the possibility of the local alignment of the transport directions of the mesh with the transport directions of mass, see figure 1.9b. Hence, the miss alignment, described by the minimum value of the scalar products
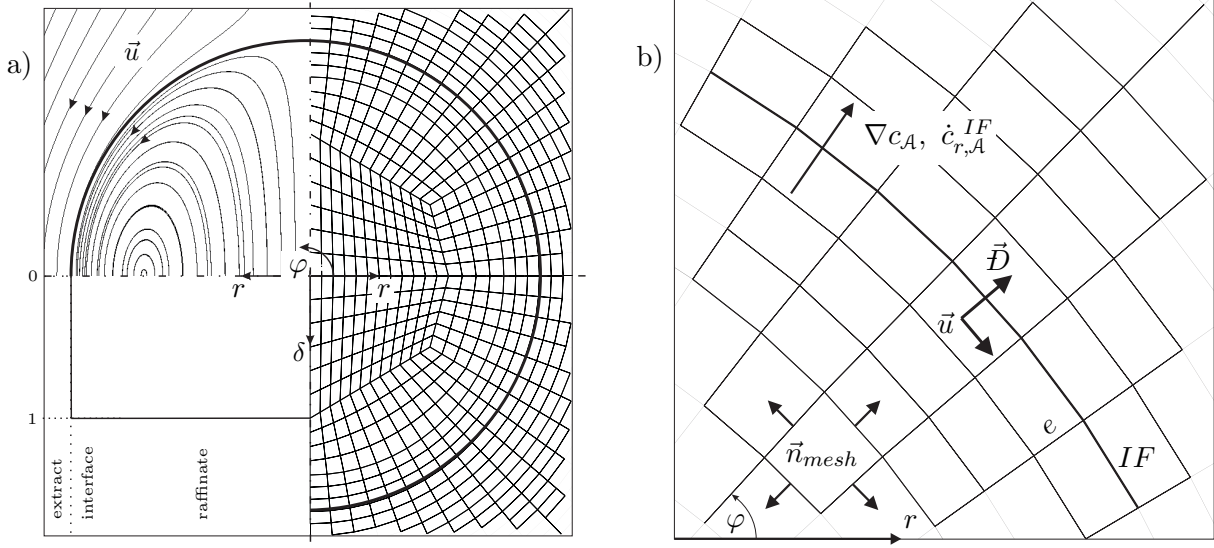
Figure 1.9: Lagrangian approach for mass transport at free interfaces: a) Principle sketch of the interface-tracking method with phase-fitted computational domains, the stream lines and the phase-field function δ; b) Mass transfer at the free interface: alignment of the mesh and the mass-transport direction in conjunction with the sharp interface.

for each cell

$$\min(\vec{n}_{mesh} \cdot \vec{u}) \approx 0, \tag{1.29}$$

vanishes in good approximation close to the free interface, where steep concentration gradients $\nabla c_{\mathcal{A}}$ can be expected, present in the direction of the interfacial mass flux $\dot{c}_{r,\mathcal{A}}^{IF}$, cf. Jasak (1996). Here, the normal vectors at the cell faces, generalized to $\vec{n}_{mesh}$, and the transport directions of mass, described by the flow vector $\vec{u}$, that is always tangential to the free interface, and the diffusion vector $\vec{D}$, that acts normal to the free interface, from the raffinate into the extract solvent, i.e. here from the disperse into the continuous phase, are used for the calculation of the miss alignment. In consequence, the discretization of the convective terms is of higher accuracy and the influence of numerical diffusion is minimized, cf. Patankar (1980), and the local edge length of the mesh e, the concentration gradient $\nabla c_{\mathcal{A}}$, and the magnitude of the interfacial mass flux $\dot{c}_{r,\mathcal{A}}^{IF}$ are of lower influence compared to Eulerian methods, cf. Elgeti and Sauerland (2016). A direct access to the concentration at the free interface and high spatial resolution of the transfer process at the free interface is achieved.

Lagrangian methods are also termed interface-tracking methods. The Lagrangian description of the evolution of the free interface is advantageously with an Eulerian approach for the flow field and the related transport processes, cf. Hirt et al. (1970) and Hirt et al. (1997), to achieve a reasonable handling. As the evolution of the free interface is directly coupled to the topology of the computational domains, deformation, coalescence, and break up of the phases can only be handled to a limited extend. Since high cell distortions lead to bad numerical properties, cf. Schmidt et al. (2002), the need of remeshing can be expected, implying high computational efforts, cf. Ryskin and Leal (1984c), compared to Eulerian methods. Lagrangian methods are still not developed to a high level and with only a small number of applications so far, cf. Elgeti and Sauerland (2016), but provide simultaneously a high spatial resolution at the free interface, and lower numerical diffusion, cf. Ferziger and Peric (2008).

2

Modeling

A reactor model is set up for the investigation of the spatial distribution of the volumetric mass-transfer coefficient within a liquid/liquid slug-flow micro-capillary reactor, inspired by the literature review. Further, the fundamental relationships for the two-phase flow and the reactive mass transport in the two-solvent system, with and without an irreversible chemical reaction, are presented and the approach is scaled.

2.1 Reactor model

The local mass transfer at the free interface and in particular the mass transport within the slug-flow micro-capillary reactor can be understood by focusing on a periodic element inside the residence-time unit, see figure 2.1. The periodic element of length l_{pe} and with diameter d of the circular capillary tube is subjected to the disperse and continuous volumetric flow rates $\dot{V}_d$ and $\dot{V}_c$, with ratio $\hat{V} = \dot{V}_d/\dot{V}_c = \mathcal{F}(\zeta_d)$. The global cylindrical coordinate system moves with the average velocity of the disperse phase $\overline{w}_{z,d}$. The velocity difference $\overline{\Delta w}_z$ appears. A periodic coupling of the boundary conditions at the left and the right boundary appears for all velocity components, while the driving pressure decreases in the axial direction with pressure gradient ∇p. The two-phase flow is modeled assuming a laminar flow of two immiscible,

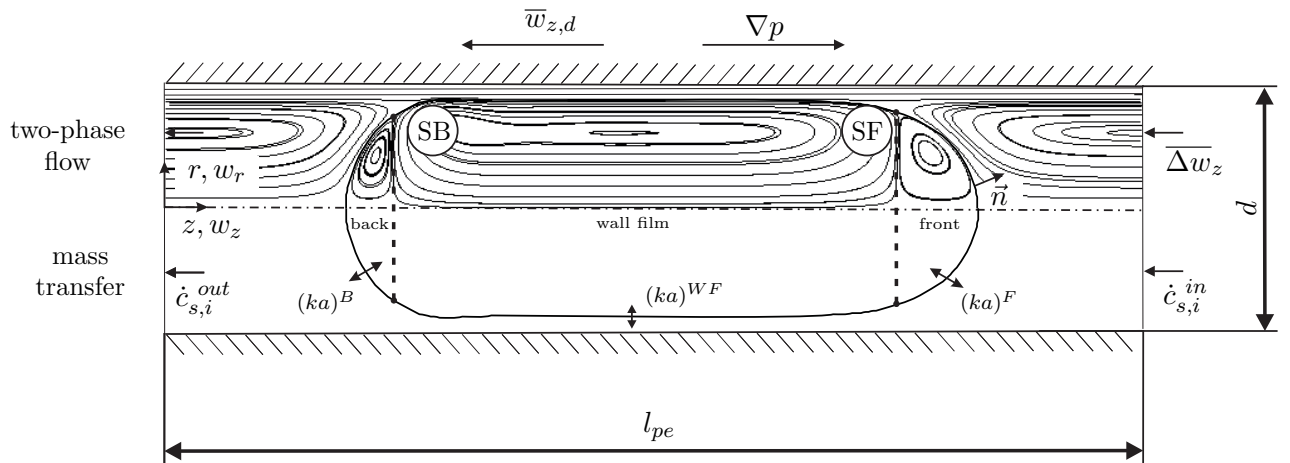**Figure 2.1:** Reactor model for the investigation of the local mass transfer in a liquid/liquid slug-flow micro-capillary reactor.

incompressible and isothermal liquids. A clean interface with a constant interfacial tension σ is present and gravity is not taken into account. The local interfacial normal vector $\vec{n}$ points into the continuous phase. The mass transport is investigated for a steady-state two-phase flow,

based on infinite dilute solutions of the solutes $\mathcal{A}$ and $\mathcal{B}$ and in conjunction with a clean interface without additional mass-transfer resistance. Mutual interactions between the solvents and the solutes do not appear. An isothermal second-order chemical reaction, with constant reaction velocity governs the consumption of the solutes $\mathcal{A}$ and $\mathcal{B}$ inside the extract solvent. Hence, a back coupling of the mass transport to the two-phase flow is not present and constant diffusion coefficients, densities, and viscosities appear.

For an assignment of the raffinate solvent to the continuous phase the mass balances for solute $\mathcal{A}$ can be written to:

$$\text{raffinate} \quad \frac{\partial \overline{c}_{r,\mathcal{A}}}{\partial \tau_m} = \dot{c}_{r,\mathcal{A}}^{in} - \dot{c}_{r,\mathcal{A}}^{out} - \dot{c}_{r,\mathcal{A}}^{IF}, \tag{2.1}$$

$$\text{extract} \quad \frac{\partial \overline{c}_{e,\mathcal{A}}}{\partial \tau_m} = \dot{c}_{r,\mathcal{A}}^{IF} \frac{\zeta_r}{1-\zeta_r} + \iota_{e,\mathcal{B}}. \tag{2.2}$$

Both balances are coupled by the interfacial mass fluxes, with $\dot{c}_{e,\mathcal{A}}^{IF} = \dot{c}_{r,\mathcal{A}}^{IF} \ (\zeta_r/(1-\zeta_r))$. The change of the concentration inside the raffinate solvent depends on the actual mass flux $\dot{c}_{r,\mathcal{A}}^{IF}$ and the net mass flux across the periodic element $\Delta \dot{c}_{r,\mathcal{A}}^{in,out} = \dot{c}_{r,\mathcal{A}}^{in} - \dot{c}_{r,\mathcal{A}}^{out} \neq 0$. The net mass flux across the periodic element results from the disperse flow structure in combination with the consecutive generation of the flow pattern and the related temporal offset for the beginning of the transfer process in each element. A general solution to the mass balance of the raffinate solvent is not known, cf. Russell et al. (2008). But, the influence of the net mass flux $\Delta \dot{c}_{r,\mathcal{A}}^{in,out}$ may be estimated. Therefore, a group of consecutive periodic elements is investigated, see figure 2.2. If the mass transfer starts in all periodic elements at the time, the temporal offset would
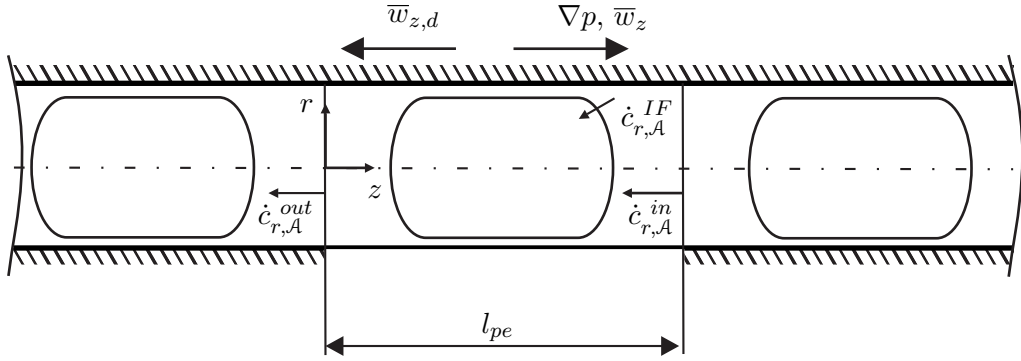
Figure 2.2: Influence of axial dispersion to the description of mass transfer at consecutive periodic elements.

vanish and $\dot{c}_{r,\mathcal{A}}^{in} = \dot{c}_{r,\mathcal{A}}^{out}$ would hold. This is also the case in good approximation, when the time to travel the length of a periodic element $l_{pe}/\overline{w}_z$, characterizing the time-scale for the consecutive generation and the shifted beginning of the transfer process, is much shorter than the characteristic diffusion-time scale $\mathcal{D}/d^2$, relevant to describe the progress of the transfer process, i.e.

$$\frac{l_{pe}}{\overline{w}_z} \frac{\mathcal{D}}{d^2} = \frac{L_{pe}}{Pe} \ll 1. \tag{2.3}$$

On basis of the estimated values in section 1.3, the ratio appears to $L_{pe}/Pe \sim 4 \cdot 10^{-3}$. Here, the enhanced interfacial mass flux due to a chemical reaction is assumed to be still in the same magnitude as for the pure physical mass flux, cf. Levenspiel (2007). Accordingly, the condition is fulfilled for a transport system that is characterized by a large ratio of convection

to diffusion. Hence, the influence of axial dispersion to the description of the volumetric mass-transfer coefficient vanishes, i.e. $\dot{c}_{r,\mathcal{A}}^{in} = \dot{c}_{r,\mathcal{A}}^{out}$, and the system converges to periodically coupled boundaries with a periodic mass flux $\dot{c}_{r,\mathcal{A}}^{per} = \dot{c}_{r,\mathcal{A}}^{in} = \dot{c}_{r,\mathcal{A}}^{out}$. Hence, the volumetric mass-transfer coefficient in the pseudo closed system can be described by the solution of the mass balance, or the direct evaluation of the mass flux at the steady-state free interface and the related portions of the volumetric mass-transfer coefficient

$$ka = \frac{Q}{\tau_m} \ln \left(\frac{c_{r,\mathcal{A}}^{eq,\tau_m} - c_{r,\mathcal{A}}^0}{c_{r,\mathcal{A}}^{eq,\tau_m} - \overline{c}_{r,\mathcal{A}}} \right) = \int_a \frac{d\dot{c}_{r,\mathcal{A}}^{IF,\tau_m}}{\Delta c_{\mathcal{A},ln}} da = (ka)^F + (ka)^{WF} + (ka)^B. \tag{2.4}$$

The presented train of thoughts extends the plug-flow approach, compare section 1.3.1, to a slug-flow approach, that considers the influence of axial dispersion for a large ratio of convection to diffusion. Further, the interface is separated into the wall film (WF) and the caps, with Front (F) and Back (B), based on the saddle points of the underlying flow structure at the free interface (SF,SB), as shown in figure 2.1.

2.2 Two-phase flow

The relationships governing the two-phase flow system can be separated into conservation laws governing the fluid motion and interfacial coupling conditions.

2.2.1 Fluid motion

The flow of an incompressible, isothermal, Newtonian fluid phase p, with $p = c, d$, of constant density, is governed by the Navier-Stokes equations and the continuity equation, presented for example in Bird et al. (2007),

$$\rho_p \left(\frac{\partial \vec{u}_p}{\partial \tau} + (\vec{u}_p \cdot \nabla) \vec{u}_p \right) = -\nabla p_p + \mu_p \nabla^2 \vec{u}_p, \tag{2.5}$$

$$\nabla \cdot \vec{u}_p = 0. \tag{2.6}$$

In these equations, τ is the time, $\vec{u}_p$ is the velocity vector, p_p is the pressure, the density is presented by ϱ_p and the dynamic viscosity is μ_p. Within the momentum equations, there are no unsymmetrical forces and an axial symmetric flow field is present, as the influence of gravity is negligible, compare section 1.3.1.

2.2.2 Interfacial conditions

The free interface separates the two liquid phases as a thin layer and acts as a free boundary for each phase. A local Cartesian coordinate system (n, t_1, t_2), see figure 2.3, is introduced for the description of the circumstances at the free interface, with the corresponding velocities (u, v, w). The normal direction coincides with the local interfacial normal vector $\vec{n}$. The interfacial conditions may be divided into kinematic and dynamic conditions, coupling the disperse and the continuous phase, cf. Clift et al. (1978). The kinematic interfacial condition provides continuity of the velocity vectors

$$\vec{u}_c^{IF} = \vec{u}_d^{IF} \tag{2.7}$$

at both sides of the interface, with the local Cartesian velocity vector at the free interface $\vec{u}_p^{IF} = \left(u_p^{IF}, v_p^{IF}, w_p^{IF} \right)^T$. The dynamic condition is a stress balance at the free interface. The
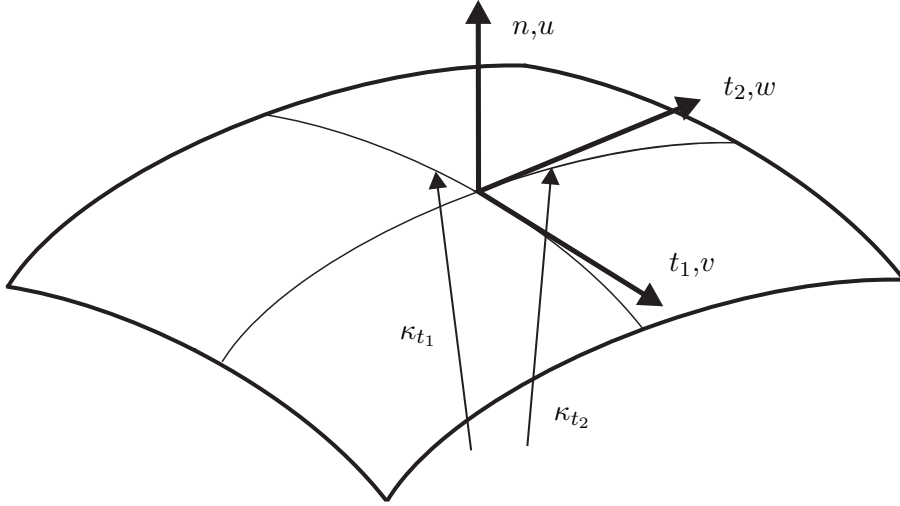
Figure 2.3: Local interfacial coordinate system with curvatures.

normal stresses are balanced with the pressure on either side, i.e.

$$p_c^{IF} + 2\mu_c \left.\frac{\partial u_c}{\partial n}\right|^{IF} + \kappa\sigma = p_d^{IF} + 2\mu_d \left.\frac{\partial u_d}{\partial n}\right|^{IF}. \tag{2.8}$$

Here, p_p^{IF} is the pressure at the interface, $\partial u_p/\partial n|^{IF}$ represents the derivative of the normal velocity with respect to the normal direction and μ_p is the dynamic viscosity, all related to the phase p. The interfacial pressure jump appears as the product of surface tension σ and local mean curvature of the interface

$$\kappa = \kappa_{t_1} + \kappa_{t_2}, \tag{2.9}$$

where κ_{t_1} and κ_{t_2} are the curvatures along the local Cartesian coordinates t_1 and t_2. In the tangential directions, the viscous shear stresses have to be equal, presented by

$$\mu_d \left(\left.\frac{\partial u_d}{\partial t_1}\right|^{IF} + \left.\frac{\partial v_d}{\partial n}\right|^{IF} \right) = \mu_c \left(\left.\frac{\partial u_c}{\partial t_1}\right|^{IF} + \left.\frac{\partial v_c}{\partial n}\right|^{IF} \right), \tag{2.10}$$

$$\mu_d \left(\left.\frac{\partial u_d}{\partial t_2}\right|^{IF} + \left.\frac{\partial w_d}{\partial n}\right|^{IF} \right) = \mu_c \left(\left.\frac{\partial u_c}{\partial t_2}\right|^{IF} + \left.\frac{\partial w_c}{\partial n}\right|^{IF} \right). \tag{2.11}$$

Here, $\partial u_p/\partial t_1|^{IF}$ is the derivative of the normal velocity u with respect to the tangential direction t_1, $\partial v_p/\partial n|^{IF}$ is the derivative of the tangential velocity v with respect to the normal direction, $\partial u_p/\partial t_2|^{IF}$ is the derivative of the normal velocity u with respect to the tangential direction t_2 and $\partial w_p/\partial n|^{IF}$ is the derivative of the tangential velocity component w with respect to the normal direction.

2.3   Reactive mass transport

The relationships governing the mass transport, the chemical reaction, and the interfacial coupling are introduced.

2.3.1 Mass transport

The transport of a solute i, with $i = \mathcal{A}$ or $\mathcal{B}$, present in a solvent s, with $s = r$ or e, at infinite dilute volumetric concentration $c_{s,i}$ is governed by the mass transport equation, cf. Baehr and Stephan (2006)

$$\frac{\partial c_{s,i}}{\partial \tau_m} + \nabla \vec{u}_s \cdot c_{s,i} = \mathcal{D}_{s,i} \nabla^2 c_{s,i} + \iota_{s,i}. \tag{2.12}$$

Beyond the mass-transfer time τ_m and the spatial coordinates, the influence parameters are the constant velocity field in the corresponding solvent $\vec{u}_s$, the Fickian diffusion coefficient $\mathcal{D}_{s,i}$ and the chemical reaction rate $\iota_{s,i}$, which will be described in detail below. Due to the infinite dilute solution, i.e. $c_{s,i} \to 0$, the density, the viscosity and the overall molar composition are quasi constant in each solvent, i.e. $\nabla (c_{s,i} \vec{u}_s) = \vec{u}_s \cdot \nabla c_{s,i}$ holds.

2.3.2 Chemical reaction

The irreversible elementary reaction equation, cf. Levenspiel (2007),

$$\nu_{\mathcal{A}} \mathcal{A} + \nu_{\mathcal{B}} \mathcal{B} \longrightarrow \text{Products} \tag{2.13}$$

governs the consumption of the solutes $\mathcal{A}$ and $\mathcal{B}$ and the generation of products in the extract solvent. Here, the stoichiometric coefficients are $\nu_{\mathcal{A}}$ and $\nu_{\mathcal{B}}$. On this basis, the reaction rate for a second-order chemical reaction is described using the isothermal reaction velocity constant ϑ and the local concentrations $c_{e,\mathcal{A}}$ and $c_{e,\mathcal{B}}$, as well as the stoichiometric coefficients by the product approach, cf. Levenspiel (2007),

$$\iota_{e,i} = -\nu_i \, \vartheta \, c_{e,\mathcal{A}} \, c_{e,\mathcal{B}}. \tag{2.14}$$

The incorporation of the reaction rate in the corresponding mass transport equation for the extract solvent allows the description of reactive mass transport of both solutes, i.e.

$$\begin{aligned}
\frac{\partial c_{e,\mathcal{A}}}{\partial \tau_m} + \vec{u}_e \cdot \nabla c_{e,\mathcal{A}} &= \mathcal{D}_{e,\mathcal{A}} \nabla^2 c_{e,\mathcal{A}} - \nu_{\mathcal{A}} \vartheta \, c_{e,\mathcal{A}} \, c_{e,\mathcal{B}}, \\
\frac{\partial c_{e,\mathcal{B}}}{\partial \tau_m} + \vec{u}_e \cdot \nabla c_{e,\mathcal{B}} &= \mathcal{D}_{e,\mathcal{B}} \nabla^2 c_{e,\mathcal{B}} - \nu_{\mathcal{B}} \vartheta \, c_{e,\mathcal{A}} \, c_{e,\mathcal{B}}.
\end{aligned} \tag{2.15}$$

The dependency of the chemical reaction on both solutes introduces a coupling of both equations.

2.3.3 Interfacial conditions

Similar to the two-phase flow, interfacial conditions for the concentration fields of both solvents have to be formulated at the free interface, see figure 2.4. The local adapted normal direction n_m, coinciding with the local normal vector $\vec{n}$ and pointing from the raffinate into the extract solvent, is used for the formulation. A relation for the local concentrations at the free interface, derived from the continuity of the chemical potential across the interface is

$$c_{r,i}^{IF} \, m_i = c_{e,i}^{IF}. \tag{2.16}$$

Here, the ratio of the concentrations at the free interface, i.e. of the raffinate phase $c_{r,i}^{IF}$ and of the extract solvent $c_{e,i}^{IF}$ is expressed by the constant distribution coefficient m_i, cf. Nernst (1891). The second constrain is given by the continuity of the diffusive mass flux at the free
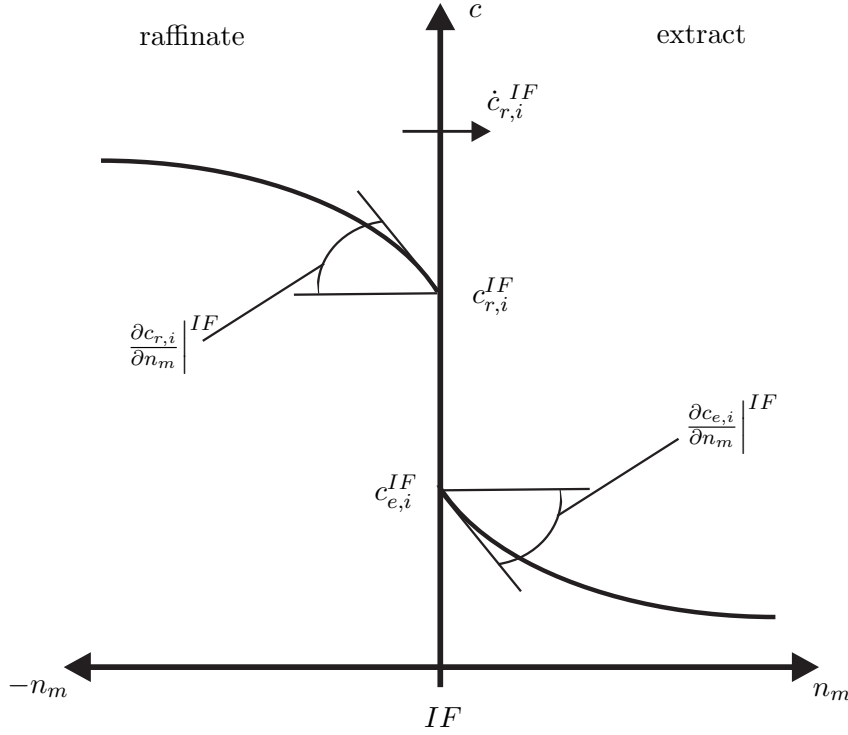
Figure 2.4: Mass transfer across the free interface.

interface, by engaging Fick's law, cf. Fick (1855), i.e.

$$\mathcal{D}_{r,i} \left.\frac{\partial c_{r,i}}{\partial n_m}\right|^{IF} = \mathcal{D}_{e,i} \left.\frac{\partial c_{e,i}}{\partial n_m}\right|^{IF}. \tag{2.17}$$

The local derivatives of the concentrations $\partial c_{r,i}/\partial n_m|^{IF}$ and $\partial c_{e,i}/\partial n_m|^{IF}$ in the normal direction n_m, taken at the free interface and the Fickian diffusion coefficients $\mathcal{D}_{r,i}$ and $\mathcal{D}_{e,i}$ are present.

2.4   Scaling

The complete model and the fundamental relationships for the two-phase flow and the reactive mass transport are scaled. The capillary diameter is used as characteristic length scale for the coordinates and length, resulting in: $R = r/d$, $Z = z/d$, $N = n/d$, $T_1 = t_1/d$, $T_2 = t_2/d$, $N_m = n_m/d$, $L_{pe} = l_{pe}/d$, and the dimensionless diameter $D = 1$. The volumetric mass-transfer coefficient, referenced to the raffinate solvent, and the portions are scaled with the diameter and the diffusion coefficient of the raffinate solvent, i.e.

$$Si = Sh\alpha = \frac{kad^2}{\mathcal{D}_{r,\mathcal{A}}} = \int_\alpha dSi = Si^F + Si^{WF} + Si^B, \tag{2.18}$$

Here, the dimensionless volumetric mass-transfer coefficient Si appears as product of the Sherwood number $Sh = kd/\mathcal{D}_{r,\mathcal{A}}$, referenced to the raffinate solvent, and the dimensionless interfacial area $\alpha = ad$, with its portions and the dimensionless local volumetric mass-transfer coefficient dSi. All other scales will be introduced below in the respective sections.

2.4.1 Two-phase flow

In addition to the geometric scaling, the velocities of the phases are scaled by the average velocity of the capillary, i.e. $\vec{U}_p = \vec{u}_p/\overline{w}_z$, the pressure is scaled by the inertial pressure, i.e. $P_p = p_p/\varrho\overline{w}_z^2$, the dimensionless curvature is $K = \kappa d$, and the dimensionless time is $T = \tau\overline{w}_z/d$. Hence, the dimensionless formulation of the Navier-Stokes equations and the continuity for each fluid phase p is

$$\frac{\partial\vec{U}_p}{\partial T} + \left(\vec{U}_p \cdot \nabla\right)\vec{U}_p = -\nabla P_p + \frac{1}{Re_p}\nabla^2\vec{U}_p, \tag{2.19}$$

$$\nabla \cdot \vec{U}_p = 0. \tag{2.20}$$

In this dimensionless form the Reynolds-numbers $Re_p = \varrho_p\overline{w}_{z,d}d/\mu_p$ occur, while $Re_c = Re_d \cdot \hat{\varrho}/\hat{\mu}$, with the density ratio $\hat{\varrho} = \varrho_d/\varrho_c$ and the viscosity ratio $\hat{\mu} = \mu_d/\mu_c$ holds.

The scaling is also applied to the interfacial conditions. The dimensionless form of the kinematic condition is

$$\vec{U}_c^{IF} = \vec{U}_d^{IF}. \tag{2.21}$$

The dimensionless forms of the dynamic condition are

$$P_c^{IF} + \frac{2}{Re_c}\frac{\partial U_c}{\partial N}\bigg|^{IF} + \frac{K}{Re_c \cdot Ca_c} = \hat{\rho}\left(P_d^{IF} + \frac{2}{Re_d}\frac{\partial U_d}{\partial N}\bigg|^{IF}\right), \tag{2.22}$$

$$\left(\frac{\partial V_c}{\partial N}\bigg|^{IF} + \frac{\partial U_c}{\partial T_1}\bigg|^{IF}\right) = \hat{\mu}\left(\frac{\partial V_d}{\partial N}\bigg|^{IF} + \frac{\partial U_d}{\partial T_2}\bigg|^{IF}\right), \tag{2.23}$$

$$\left(\frac{\partial W_c}{\partial N}\bigg|^{IF} + \frac{\partial U_d}{\partial T_2}\bigg|^{IF}\right) = \hat{\mu}\left(\frac{\partial W_d}{\partial N}\bigg|^{IF} + \frac{\partial U_d}{\partial T_2}\bigg|^{IF}\right). \tag{2.24}$$

Here, the capillary number of the continuous phase $Ca_c = \mu_c\overline{w}_z/\sigma$ is present, additionally to the Reynolds numbers Re_d and Re_c.

2.4.2 Reactive mass transport

The concentration of solute $\mathcal{A}$ is scaled by its initial concentration in the raffinate solvent, i.e. the dimensionless concentration appears to $C_{r,\mathcal{A}} = c_{r,\mathcal{A}}/c_{r,\mathcal{A}}^0$, while the concentration of solute $\mathcal{B}$ is scaled by its initial concentration in the extract solvent, i.e. $C_{e,\mathcal{B}} = c_{e,\mathcal{B}}/c_{e,\mathcal{B}}^0$. The Fourier number $Fo_{s,i} = \tau_m d^2/\mathcal{D}_{s,i}$ is found as dimensionless mass-transfer time. The solvent velocity is scaled with the average capillary velocity, i.e. $\vec{U}_s = \vec{u}_s/\overline{w}_z$. Introducing the scaling into the equation for the mass transport results in

$$\frac{\partial C_{s,i}}{\partial\left(Pe_{s,i}Fo_{s,i}\right)} + \vec{U}_s \cdot \nabla C_{s,i} = \frac{1}{Pe_{s,i}}\nabla^2 C_{s,i} + I_{s,i}. \tag{2.25}$$

Here, $Pe_{s,i} = \overline{w}_z d/\mathcal{D}_{s,i}$ is the Péclet number and $I_{s,i}$ is the dimensionless reaction rate, which only has influence within the extract solvent. The convective species transport rate is used for the scaling of the reaction rate $\iota_{e,i}$, namely $d/c_{e,\mathcal{B}}^0\overline{w}_z$ for solute $\mathcal{A}$ and $d/c_{e,\mathcal{A}}^0\overline{w}_z$ for solute $\mathcal{B}$. Hence, the dimensionless reaction rate is

$$I_{e,i} = -\nu_i\frac{Ha_{e,i}^2}{Pe_{e,i}}C_{e,\mathcal{A}}C_{e,\mathcal{B}}. \tag{2.26}$$

Here, $Ha_{e,\mathcal{A}} = d\sqrt{\vartheta c_{e,\mathcal{B}}^0/\mathcal{D}_{e,\mathcal{A}}}$ and $Ha_{e,\mathcal{B}} = d\sqrt{\vartheta c_{e,\mathcal{A}}^0/\mathcal{D}_{e,\mathcal{B}}}$ are the modified Hatta numbers of both solutes, with $c_{e,\mathcal{A}}^0 = c_{r,\mathcal{A}}^0 \, \zeta_r/(1-\zeta_r)$. The dimensionless form of the coupled system of equations inside the extract solvent can then be written with reference to the raffinate solvent to

$$\frac{\partial \left(C_{e,\mathcal{A}} \, \hat{\mathcal{D}}_{\mathcal{A}}^2\right)}{\partial \left(Pe_{r,\mathcal{A}} Fo_{r,\mathcal{A}}\right)} + \vec{U}_e \cdot \nabla C_{e,\mathcal{A}} = \frac{\hat{\mathcal{D}}_{\mathcal{A}}}{Pe_{r,\mathcal{A}}} \left(\nabla^2 C_{e,\mathcal{A}} - Ha_{e,\mathcal{A}}^2 C_{e,\mathcal{A}} C_{e,\mathcal{B}}\right),$$

$$\frac{\partial \left(C_{e,\mathcal{B}} \, \mathcal{D}_{\mathcal{A}}^2 \, \lambda\right)}{\partial \left(Pe_{r,\mathcal{A}} Fo_{r,\mathcal{A}}\right)} + \vec{U}_e \cdot \nabla C_{e,\mathcal{B}} = \frac{\mathcal{D}_{\mathcal{A}} \, \lambda}{Pe_{r,\mathcal{A}}} \left(\nabla^2 C_{e,\mathcal{B}} - \psi Ha_{e,\mathcal{A}}^2 C_{e,\mathcal{A}} C_{e,\mathcal{B}}\right). \tag{2.27}$$

The given formulation is referenced to the properties of solute $\mathcal{A}$ in the raffinate solvent. The ratio of the diffusion coefficients is $\mathcal{D}_{\mathcal{A}} = \hat{\mathcal{D}}_{e,\mathcal{A}}/\mathcal{D}_{r,\mathcal{A}}$, the ratio of the Péclet numbers is $\lambda = Pe_{e,\mathcal{A}}/Pe_{e,\mathcal{B}}$, that gives a relation for the diffusion of the solutes in the extract solvent and $\psi = \left[\nu_{\mathcal{B}} c_{r,\mathcal{A}}^0/(\nu_{\mathcal{A}} c_{e,\mathcal{B}}^0)\right] \, \zeta_r/(1-\zeta_r)$ incorporates the ratio of the stoichiometric coefficients, the initial concentrations and the phase fraction of raffinate solvent, i.e. the volume ratio.

Further, the scaling of the interfacial conditions gives the dimensionless forms

$$C_{r,i}^{\ IF} \, m_i = C_{e,i}^{\ IF}, \tag{2.28}$$

$$\left.\frac{\partial C_{r,i}}{\partial N_m}\right|^{IF} = \hat{\mathcal{D}}_i \left.\frac{\partial C_{e,i}}{\partial N_m}\right|^{IF}. \tag{2.29}$$

Here, $\hat{\mathcal{D}}_i = \mathcal{D}_{e,i}/\mathcal{D}_{r,i}$ represents the ratio of the diffusion coefficients.

3

Numerical method

Focusing on the numerical simulation of the spatial distribution of the mass transfer at the free interface an interface-tracking method is chosen for the numerical description, compare section 1.3.3. Besides the idea of the method, the computational approach, and performed numerical tests are described.

3.1 Interface-tracking method

In the present application, the separate phase-fitted domains are arranged around an imported steady-state interface contour, based on the specific measurements of the periodic element in a moving frame of reference, that is fixed to the disperse phase, see figure 3.1. The cells close to the
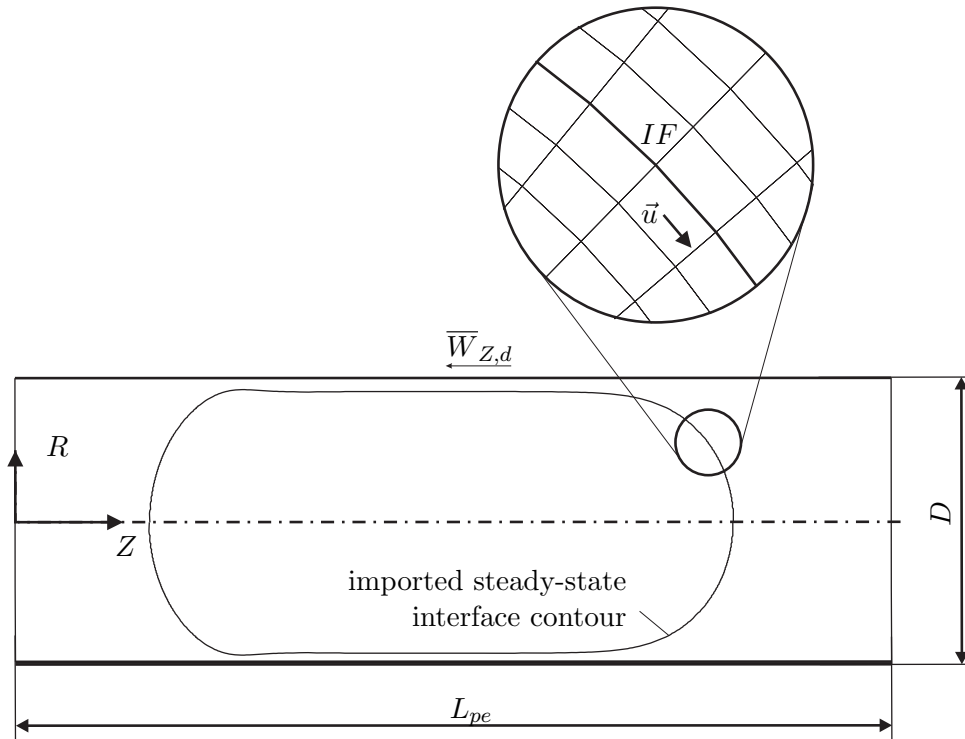
Figure 3.1: Interface-tracking method: Import of a known steady-state interface contour into the periodic element to set up static phase-fitted domains based on a moving reference frame.

free interface can be aligned with the main transport directions to minimize numerical diffusion. The governing equations are solved inside the computational domains, while the interfacial conditions are used couple the field variables across the sharp interface. Since the two-phase

flow is in steady-state and only dilute solutions are present, the computational domains do not change during the simulation of the the two-phase flow and the mass transport. Accordingly, an elaborate and computational expensive adaption of the computational domains is not present. Static phase-fitted domains can be used for the simulation of the mass transport, preserving the advantages of the interface-tracking method while getting rid of the disadvantages. Similar approaches have been used by Farmer et al. (1994) for the simulation of a two-phase flow and in conjunction with free rising spherical droplets and mass transport by Adekojo Waheed et al. (2002), Schulze (2007), Wegner (2009), a parallel flow, cf. Wolf (1998) or slug flows by for example Harries et al. (2003), Irandoust and Andersson (1989), Liu and Wang (2011), or Tsaoulidis (2015) based on an idealized interface. The specific computational approach is detailed below.

3.2   Computational approach

The computational approach is presented, based on the implementation in *OpenFOAM 2.1.0*, using the finite-volume method, cf. Weller et al. (1998). The computational domain and the simulation concept are introduced and the single concepts steps are described in detail.

Derived from the modeling approach, the examination of a radial slice of the periodic element appears to be sufficient for the numerical description, due to the axial symmetry of the flow and concentration fields, the related free interface and the circular cross-section of the capillary flow channel, illustrated in figure 3.2. According to the introduced geometrical scaling, the
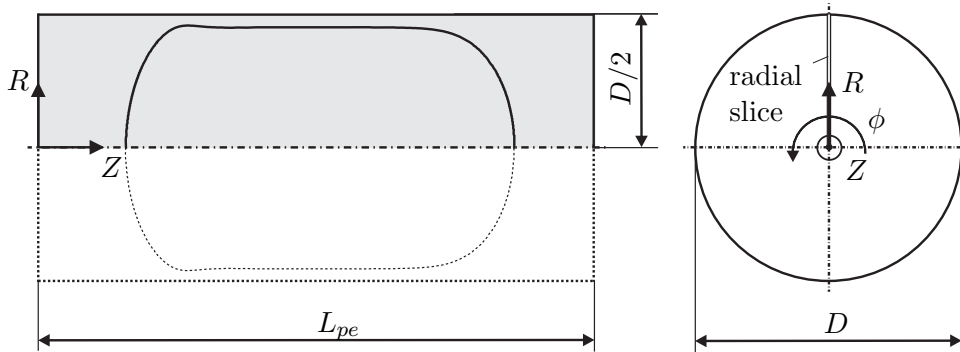
Figure 3.2: Reduction of the examined scales periodic element to a radial slice and the computational domains.

computational domain has the diameter $D = 1$, i.e. the radius $D/2$, and the length L_{pe}. A wedge is used for the specific implementation in *OpenFOAM*, since the governing equations are solved in Cartesian coordinates. The radial slice, with cylindrical coordinate system, is used for the descriptions of the thesis.

The simulation concept consists of five steps, see figure 3.3: (1) A steady-state interface is generated based on an existing volume-tracking simulation model, provided by Dittmar (2015). For this, a modified level-set method is engaged and all computations are done for a given set of dimensionless flow parameters. (2) The interface and the velocity difference $\overline{\Delta W}_z$ are extracted. The interface is used to (3) arrange separate phase-fitted domains, that are discretized by means of the finite-volume method. Both domains are coupled at the free interface by means of the field values of both phases. The interface is a sharp boundary for both domains. (4) The discretized domains are used to simulate the steady-state two-phase flow, providing the basis for (5) the simulation of the transient mass transport, with and without chemical reaction.
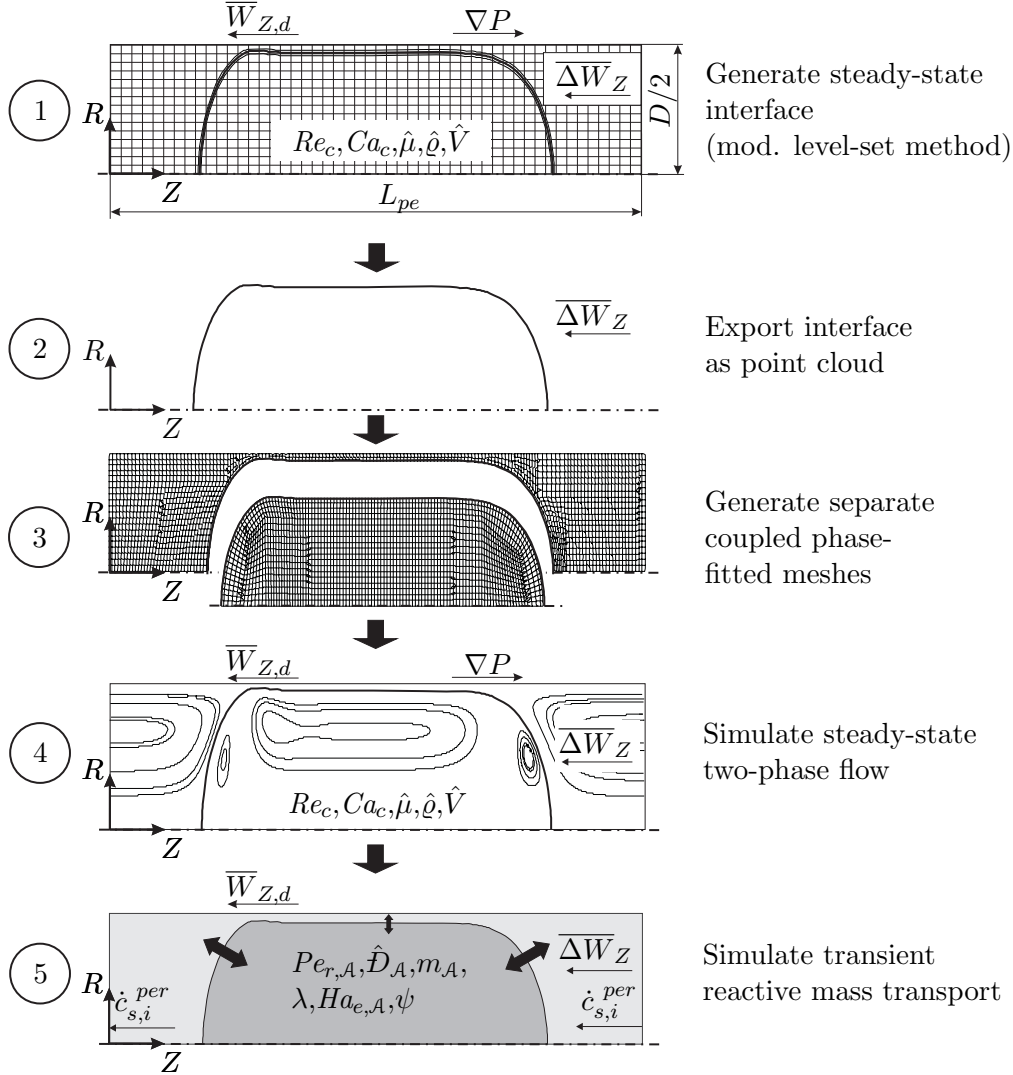
Figure 3.3: Simulation concept: 1.) Generation of the steady-state interface, using a modified level-set method, cf. Dittmar (2015). 2.) Export of the steady-state interface. 3.) Generation and discretization of separate coupled phase-fitted domains. 4.) Simulation of the steady-state two-phase flow. 5.) Simulation of the transient mass transport, with and without chemical reaction.

3.2.1 Steady-state interface - generation and export

The steady-state interface is generated in the first step of the numerical concept based on an existing simulation model of a periodic element of the liquid/liquid slug-flow micro-capillary reactor, using a volume-tracking method, cf. Dittmar (2015), illustrated in figure 3.4. The two-phase flow and the evolution of the free interface is computed with a conservative level-set method, cf. Olsson and Kreiss (2005) and Olsson et al. (2007), using a pressure driven flow, implemented in *OpenFOAM* 1.4.1.

The governing dimensionless parameters Re_c, Ca_c, $\hat{\mu}$, $\hat{\varrho}$, the periodic element length L_{pe}, and a phase fraction ζ_d are prescribed, since the ratio of volumetric flow rates $\hat{V}$ cannot be prescribed directly. The phase function $\delta(R, \phi, Z, \tau = 0)$ is initialized with an idealized shape, consisting of a cylinder with spherical caps, occupying a volume corresponding to the volume fraction ζ_d.

The set of governing equations is solved until the steady-state is achieved during the numerical

procedure, in dependence to the driving pressure gradient ∇P, that is split into a driving volume force ∇P_{stat} and a dynamic pressure field ∇P_{dyn}. Convergence is achieved, when the change of the driving pressure gradient becomes small between two consecutive iterations. Finally, the simulated flow rate ratio $\hat{V}$ can be evaluated according to equation 1.9, derived from the phase fraction ζ_d and the phase velocities $\overline{W}_{Z,d}$ and $\overline{W}_{Z,c}$. The procedure may be repeated until the desired ratio of volumetric flow rates is achieved. The steady-state interface is exported as point cloud from the steady-state phase field at $\delta(R, \Phi, Z, \tau \to \infty) = 0.5$ by interpolation to the cells centers and used for the further concept, based on a *paraView* routine and the *contour plot* filter. The point cloud is filtered by means of a low pass filter to compensate inaccuracies in conjunction with the interpolation of the point cloud.
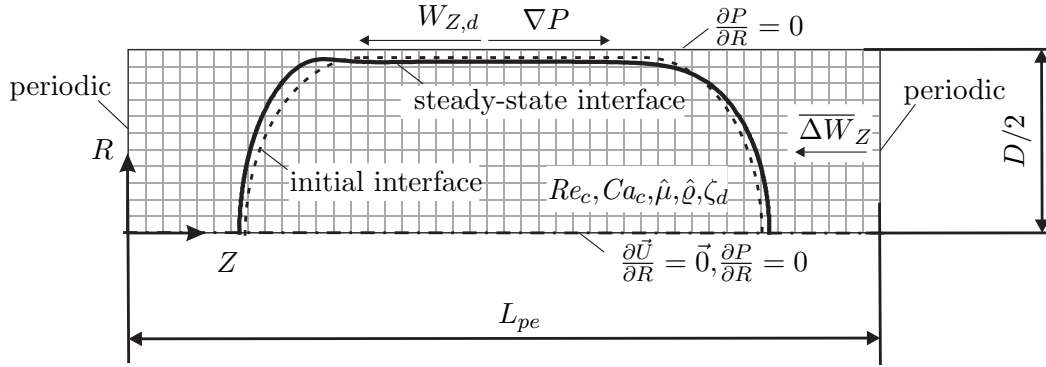

Figure 3.4: Steady-state interface: Schematic generation of the steady-state interface using the existing simulation model developed by Dittmar (2015) in dependence to the dimensionless flow parameters, including boundary conditions.

3.2.2 Separate coupled phase-fitted meshes

The steady-state interface is used to define the boundaries of two separate meshes, generated with the *blockMesh* utility. The interface is imported into a separate meshing tool, where the blocking is performed and the meshing files, i.e. *blockMesh.txt*, are created, based on *OpenOffice Calc*. The separate two-dimensional meshes are created, stitched, extruded to a wedge, and a baffle is created at the position of the free interface.

The overall computational domain is therefore divided into two domains, that are arranged around the imported steady-state interface, see figure 3.5a. The domains are further divided into blocks and cells with a quadrilateral cell topology, based on an O-grid structure. Additionally, regions where steep gradients are expected are prioritized regarding the block arrangement and their mesh qualities. The aim is to achieve a homogeneous square cell topology over the whole domain and to allow a direction-independent resolution of the gradients. The blocking is classified into three regions, according to their numerical influence to the mass transfer: The free interface (I), the wall film (II), and the bulk (III). First priority is on the interface and its immediate surroundings. The blocks and the quadrilateral cells are locally aligned with the normal direction of the free interface, that can be seen in the resulting mesh, see figure 3.6. A high numerical resolution and quality near to the interface is achieved, minimizing the influence of numerical diffusion, cf. Jasak (1996). The second priority is given to the wall-film region. Small changes of the wall-film thickness along the axial direction can cause large deviations from the desired square cell topology. Therefore, the film region is divided into several separate blocks, to adapt the cell topology. The blocks in the bulk, in certain distance to the interface, are of subordinated priority compared to the other two regions.
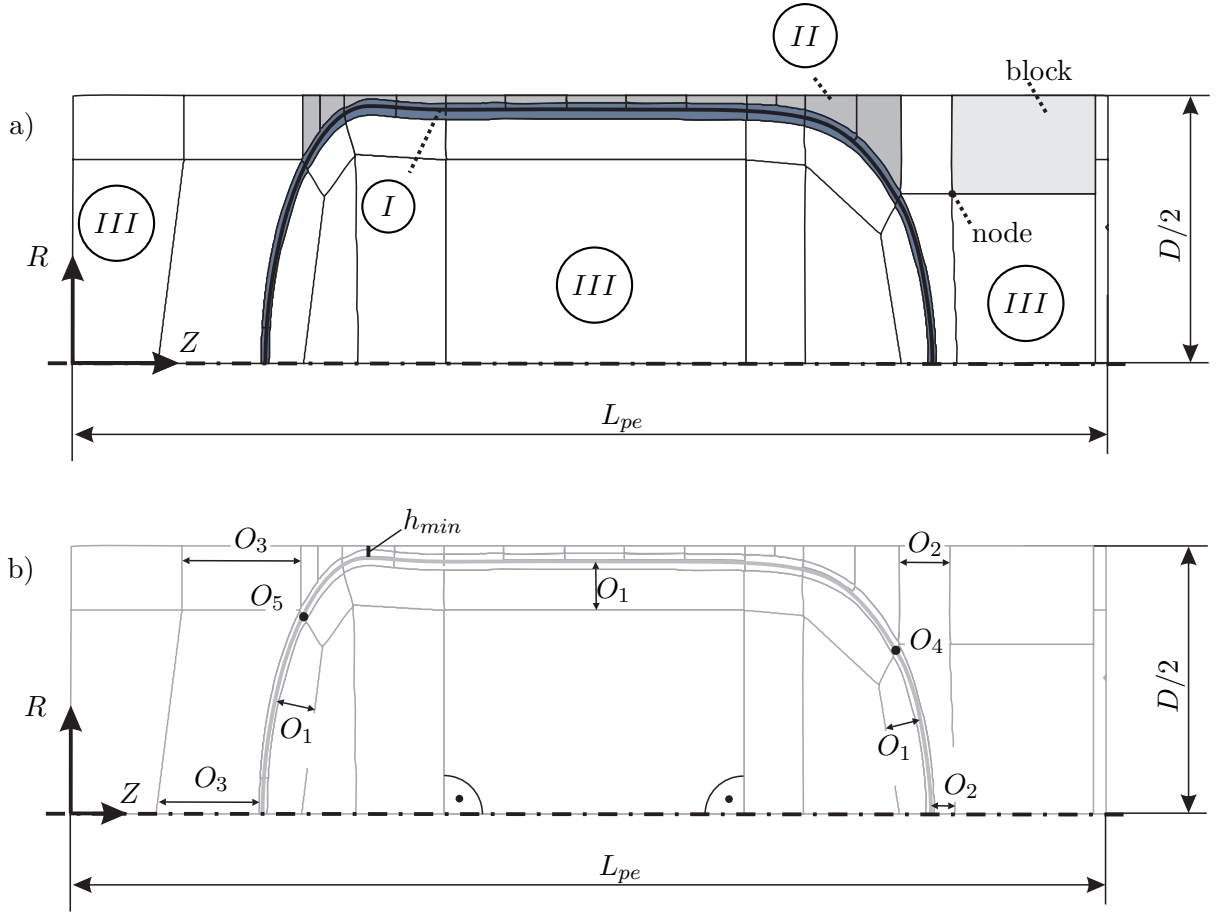
Figure 3.5: Discrete computational domain (R-axis scaled by factor of 2): a) Block structure, pointing out the priorities, namely the interface (I), the wall film (II), and the bulk (III); b) Main meshing parameters, based on heuristic lengths and angular conditions.

The strategic arrangement of each node of a block, in relation to an imported interface, is done using a meshing algorithm for the spatial arrangement of the nodes based on heuristic rules. Therefore, the meshes for three interfaces are examined in detail, namely for the capillary numbers of $Ca_c = 10^{-3}$, $Ca_c = 10^{-2}$, and $Ca_c = 10^{-1}$, while the other flow parameters, i.e. $\hat{\mu} = 1$, $\hat{\varrho} = 1$, $Re_c = 10$, and $\hat{V} = 1$, are kept constant. An optimized node arrangement is derived for each blocking and used to set up heuristic rules for the general node arrangement. The main driving parameters are illustrated in figure 3.5b, with the main meshing lengths O_1, O_2, and O_3 and conditions for a slope of $\Delta R / \Delta Z = 1$ at the points O_4 and O_5 on the free interface. An optimized heuristic arrangement of the blocks and the underlying nodes is derived from a detailed analysis of three interfaces, by means of an automated parameter variation. Optimization parameters are the cell skewness (maximum 10), the aspect ratio (maximum 5), the growth rate of two neighboring cells (maximum 2), and the mesh non-orthogonality (maximum 60°). All limits are chosen in relation to the quality measurements provided by *OpenFOAM*, cf. Weller et al. (1998). The cells near the interface are locally refined to provide a reasonable balance of numerical quality and computational time.

Figure 3.6: Numerical mesh with detailed view of the cell topology and the refinement at the free interface close to the wall film, pointing out the prescribed square cell topology with a spatial resolution of $E^{IF} = 4 \cdot 10^{-3}$, driving the overall spatial resolution.

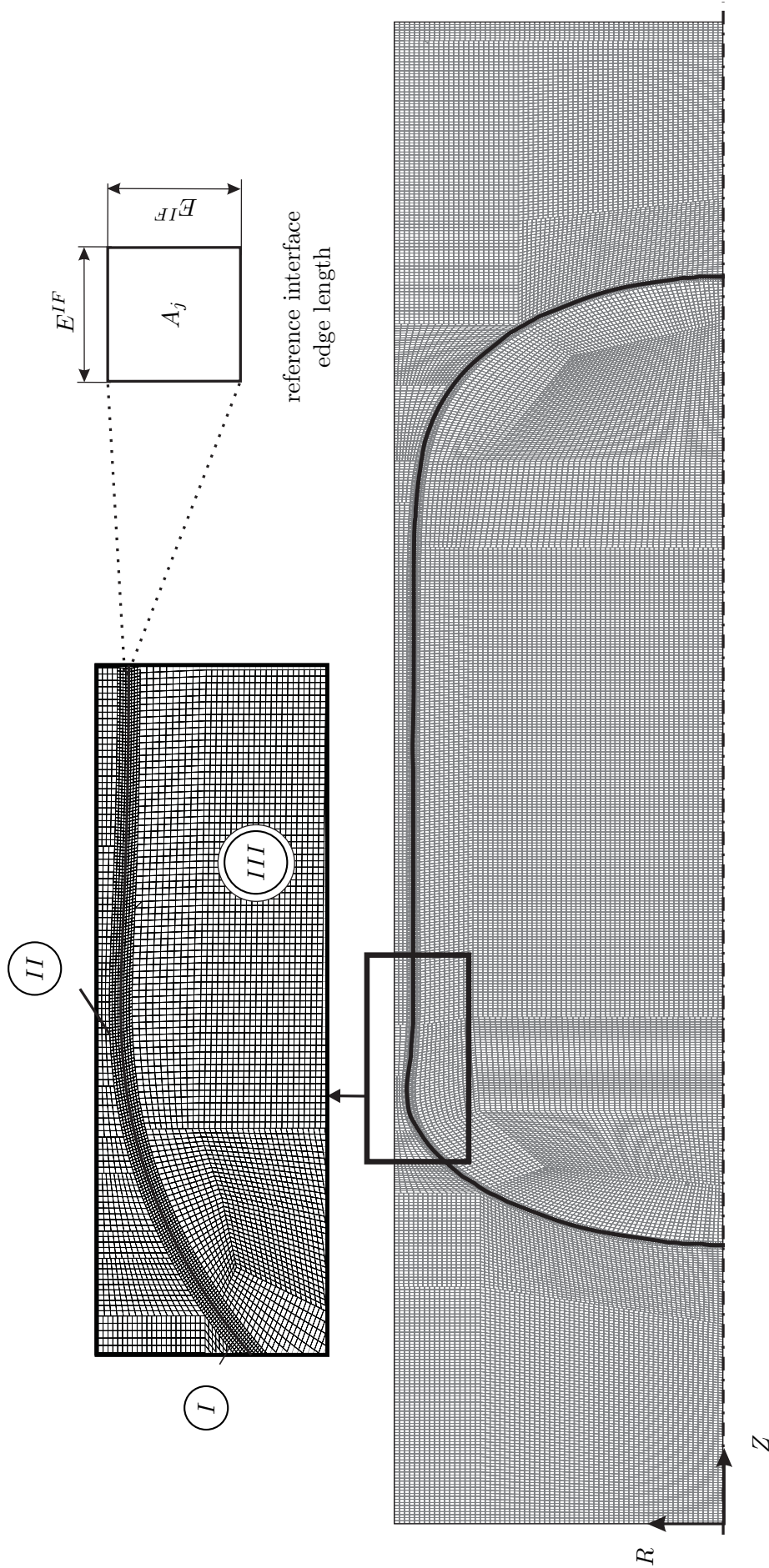The overall spatial resolution of the computational mesh is driven by the cell edge length at the free interface E^{IF}, see figure 3.6. Additionally the interfacial cell area A_j is marked in the figure. The resolutions of all other blocks and cells are automatically chosen in dependence to the prescribed interface resolution and the underlying block topology, depending on the introduced quality measures. At least three cells have to be present in the aligned blocks immediately at the free interface and at least five cells at the smallest height of the wall-film blocks to provide a reasonable number of cells for the resolution of gradients. The exact number of cells, i.e. the resolution, is derived from experience. A typical dimensionless edge length of $E^{IF} = 4 \cdot 10^{-3}$ results in a global mesh consisting of approximately 10^5 cells, giving a reasonable ratio of effort to benefit, proven in section 3.3. The discrete domains, i.e. the numerical mesh, are used for the simulation of the steady-state two-phase flow and the reactive mass transport.

3.2.3 Steady-state two-phase flow

The scaled governing equations are used for the computation of the steady-state two-phase flow. A transient numerical procedure is conducted, until a steady-state flow is achieved in the periodic element, related to the numerical handling of the pressure driven flow. The sequence of the algorithm is shown in figure 3.7. The solution procedure consists of several steps, described below:

1. **Initialization**
   Initially, the set of dimensionless flow parameters, Ca_c, Re_c, $\hat{\mu}$, $\hat{\varrho}$, as well as the corresponding discrete domains, the field data and the boundary conditions are loaded. The field data for the pressure and the velocity are mapped from the underlying volume-tracking simulation to provide initial conditions close to the desired steady-state solution. The boundary conditions are sketched in figure 3.8. The capillary wall moves with the velocity of the dimensionless disperse phase $\overline{W}_{Z,d}$ in negative Z-direction, while in flow direction the boundaries are coupled periodically and the velocity difference $\overline{\Delta W}_Z$ is prescribed, taken over from the reference simulation. Symmetry conditions apply for all field data at the center line ($R = 0$). The coupling conditions at the free interface are enforced during the simulation. The outer iteration loop starts with the first iteration $it = 1$. Unless otherwise noted, the field data of the previous iteration $it - 1$ are used for the actual iteration, while in the first iteration the field data from the volume-tracking simulation are adapted.

2. **Adjust time-step width ΔT**
   The explicit Euler-scheme is used for the temporal discretization, because of its simplicity, robustness and easy handling for parallel simulations, cf. Anderson and Wendt (2009). One global convective time step ΔT is used for both domains. The stability of the scheme is governed by two criteria, holding for each cell j of the overall computational domain, cf. Ferziger and Peric (2008). Hence, the time-step criteria, based on the cell diffusion number Di_j and the cell Courant number Co_j, appear to

$$Di_j < 0.5, \quad \text{with} \quad Di_j = \frac{\Delta T}{Re_j E_j{}^2} \tag{3.1}$$

$$Co_j < 2Di_j, \quad \text{with} \quad Co_j = \max\left(\frac{|\vec{U}_j|\Delta T}{E_j}\right). \tag{3.2}$$

In accordance to common practice, the second criterion is even set stricter to $Co_j < Di_j$. Both dimensionless parameters are evaluated at each cell of both computational domains
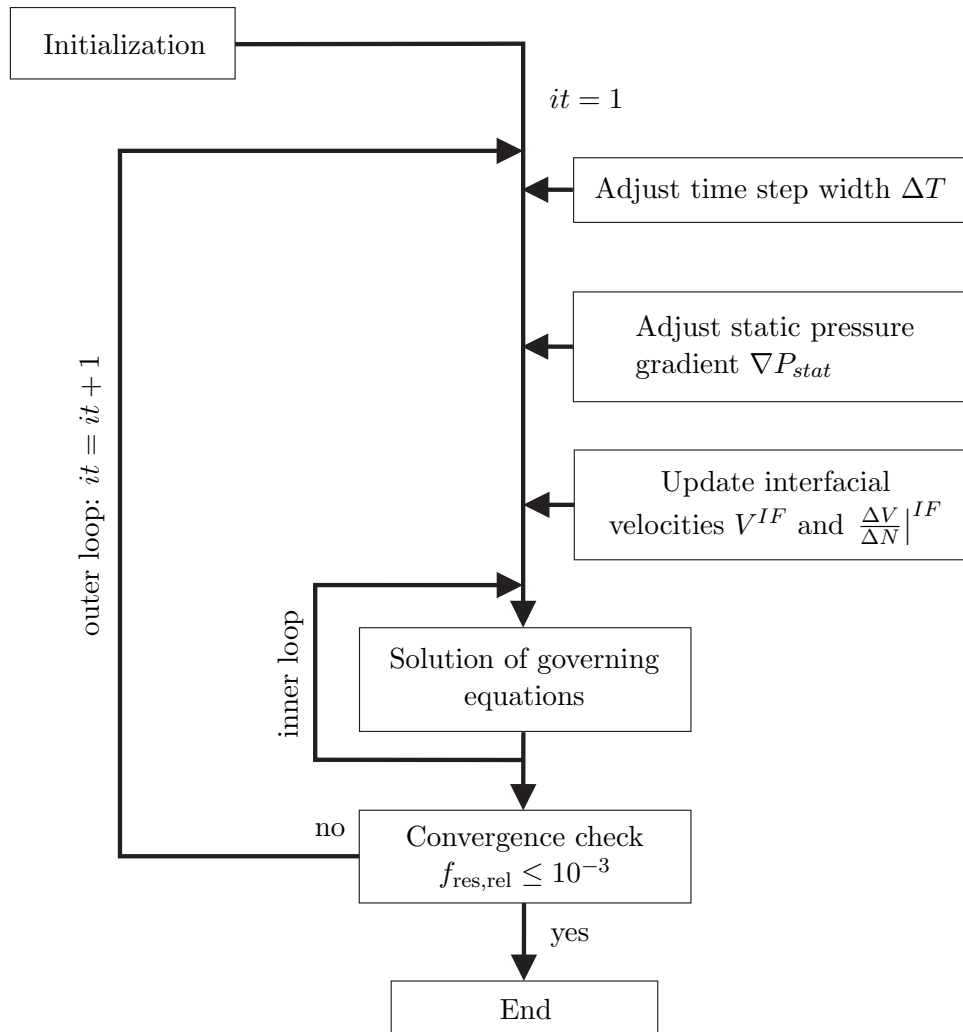
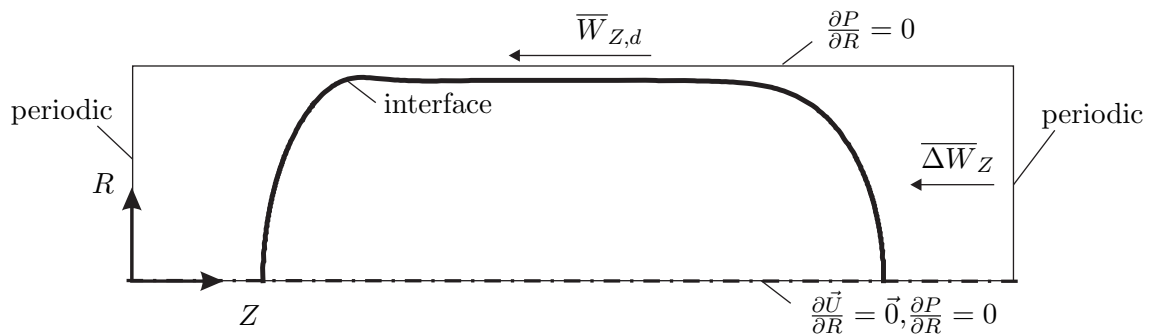**Figure 3.7:** Scheme of the steady-state two-phase flow algorithm.

Figure 3.8: Boundary conditions for the steady-state two-phase flow algorithm.

using the actual global convective time step ΔT, that is derived for the actual iteration to be

$$\Delta T = \min \left[\frac{Re_c \cdot \Delta E_{min}^2}{2} \min \left(1, \frac{\hat{\rho}}{\hat{\mu}}\right), \min \left(\frac{2E_j}{|\vec{U}_j|}\right) \right]. \tag{3.3}$$

3. **Adjust static pressure gradient** ∇P_{stat}
   The dimensionless pressure gradient ∇P is split into a static driving portion ∇P_{stat} and a dynamic portion ∇P_{dyn} to adjust the flow inside the periodic element

   $$\nabla P = \nabla P_{stat} + \nabla P_{dyn}. \tag{3.4}$$

   The adjustment of the static pressure gradient in flow direction, is used to control the velocity difference of the previous iteration $\overline{\Delta W}_{Z,it}$ in the periodic element, calculated to

   $$\overline{\Delta W}_{Z,it} = \frac{1}{\sum A_j R_j} \sum_j \left(\vec{U}_{j,it-1} \cdot \vec{e}_Z\right) R_j A_j, \tag{3.5}$$

   with A_j being the cell area, illustrated in figure 3.6, the velocity vector $\vec{U}_{j,it-1}$, $\vec{e}_z$ being the unit vector in the axial direction, and R_j being the radial position of the cell center of cell j. The actual average velocity difference is used to adapt the static pressure gradient simultaneously for all cells. The difference of the actual velocity difference $\overline{\Delta W}_{Z,it}$ and the prescribed velocity difference $\overline{\Delta W}_Z$ is directly used for the control of the static pressure gradient, due to the dimensionless formulation

   $$\nabla P_{stat,it} = \nabla P_{stat,it-1} + \left(\overline{\Delta W}_Z - \overline{\Delta W}_{Z,it-1}\right) \Omega. \tag{3.6}$$

   The relaxation factor $\Omega = 0.9$ is applied to ensure a stable numerical procedure and to prevent overshoots of the estimated value. If the relative velocity is higher than desired, the static pressure gradient is decreased, vice versa. The new estimate for the global static pressure gradient is used for the actual iteration.

4. **Update coupling conditions** V^{IF} **and** $\frac{\Delta V}{\Delta N}\Big|^{IF}$
   The discrete form of the interfacial conditions, compare section 2.1, is used for the local coupling of the velocity fields inside the domains, see figure 3.9. Since the free interface is static, the dynamic coupling condition in the normal direction is not taken into account and the normal component of the velocity vector is $U^{IF} = 0$. The remaining tangential coupling conditions are used to update the velocity fields at the free interface. In accordance to common practice in numerical calculations, a linear approximation is used for the representation of gradients normal to a boundary. The tangential interface velocity V^{IF} is interpolated, following the proposal of Schmidt et al. (2002), using the velocities and the viscosities of both domains to

   $$V^{IF} = \frac{\frac{\hat{\mu}}{\Delta N_d} V_d^{ad} + \frac{1}{\Delta N_c} V_c^{ad}}{\frac{\hat{\mu}}{\Delta N_d} + \frac{1}{\Delta N_c}}. \tag{3.7}$$

   Here, V_d^{ad} and V_c^{ad} are the tangential velocity components in the cells adjacent to the free interface within the corresponding phases, while ΔN_d and ΔN_c are the interpolation distances from the interface to the cell center. Further, the dynamic coupling condition, balancing the shear stress, gives a relation for the normal gradients of the tangential
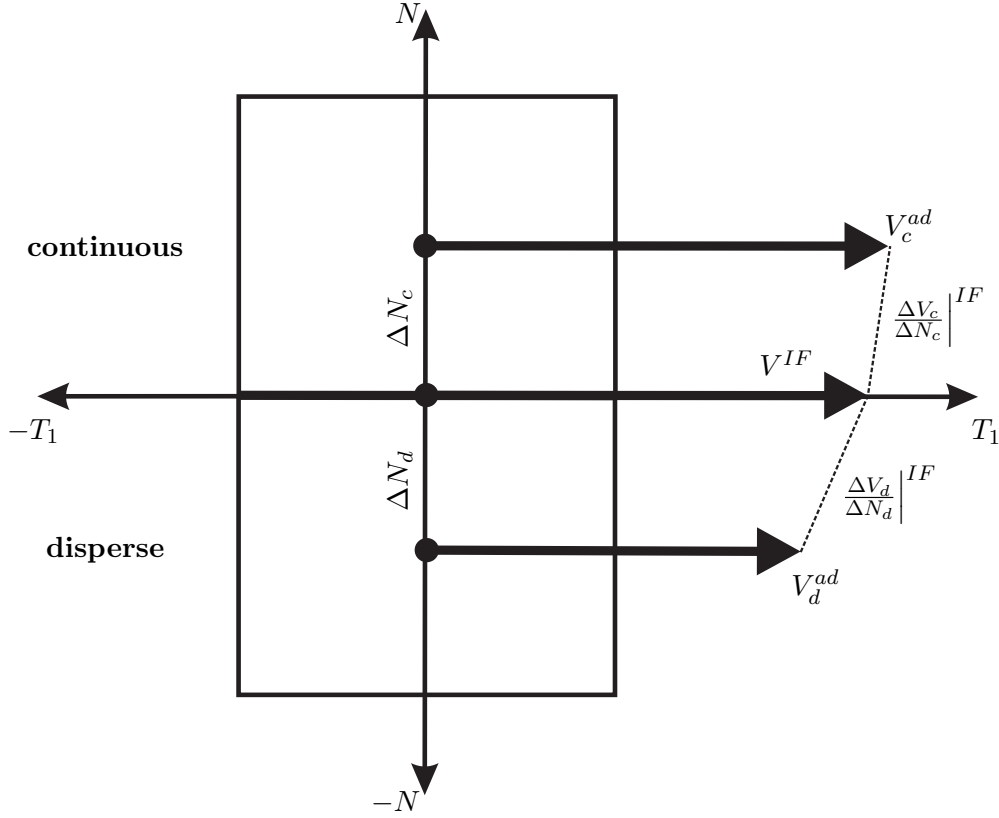
Figure 3.9: Local velocities and gradients at the discrete free interface based on the local Cartesian coordinate system.

velocity at the interface $\Delta V_d^{IF}/\Delta N_d|^{IF}$ and $\Delta V_c^{IF}/\Delta N_c|^{IF}$, in the respective phase.

The interface velocity and the gradient of the tangential velocity normal to the free interface are used to couple the domains. Assuming a viscosity ratio $\hat{\mu} \leq 1$, the velocity

$$\vec{U}_d^{IF} = \begin{pmatrix} 0 \\ V^{IF} \\ 0 \end{pmatrix} \tag{3.8}$$

is prescribed as boundary condition at the interface in the disperse phase. The shear stress balance is used to prescribe the discrete normal gradient of the tangential velocity as boundary condition at the interface of the continuous phase domain

$$\left.\frac{\Delta V_c}{\Delta N_c}\right|^{IF} = \hat{\mu} \left.\frac{\Delta V_d}{\Delta N_d}\right|^{IF} \tag{3.9}$$

using the shear-stress balance at the free interface, with $\Delta V_c/\Delta N_c|^{IF}$ and $\Delta V_d^{IF}/\Delta N_d|^{IF}$, appearing as gradients of the tangential velocity normal to the interface. If a viscosity ratio $\hat{\mu} > 1$ is present, the velocity is prescribed in the in the continuous phase and the normal gradient of the tangential velocity is used for back coupling in the disperse phase.

5. **Solution of governing equations**

The system of governing equations is set up and solved using a modified version of the pressure-implicit-split-operator (PISO) algorithm, provided by *OpenFOAM 2.1.0*, cf. Weller et al. (1998). Therefore, the Navier-Stokes equations are set up for each phase,

using the splitted pressure gradient, appearing to

$$\left[\frac{\partial \vec{U}_p}{\partial T} + \left(\vec{U}_p \cdot \nabla \right) \vec{U}_p \right] = -\nabla P_{p,dyn} + \frac{1}{Re_p} \nabla^2 \vec{U}_p - \nabla P_{p,stat}. \tag{3.10}$$

The momentum balances are inserted directly into the continuity equation of the corresponding domain and the systems of equations are collected in one matrix. In the inner iteration loop, a Gauss-algebraic-multi-grid (GAMG) solver is used to solve for the dynamic pressure field, until the absolute residuum of $Res \leq 10^{-7}$ is reached. The governing system of equations is set up four times to compensate for the mesh skewness. Each time it is solved four times to compensate for the mesh non-orthogonality to the numerical solution, as proposed by Ferziger and Peric (2008). Afterwards the velocity field is reconstructed.

The following discretization schemes are used for the single terms: As mentioned before, the explicit Euler scheme is used for the temporal discretization, achieving a first-order accuracy in time. The spatial derivatives within the convection and the diffusion, the gradients, and the interpolations are all discretized using a linear interpolation approach, giving second-order accuracy of the numerical solution in space. The oscillating behavior of the spatial scheme is compensated by a limiting approach, while the influence of the mesh skewness to the evaluation of gradients is fully corrected. Both options are provided by *OpenFOAM*, cf. Weller et al. (1998).

6. **Convergence check**
   At the end of the iteration loop, the numerical solution is checked for convergence. Therefore, the forces acting on the interface are balanced in axial direction, see figure 3.10. In
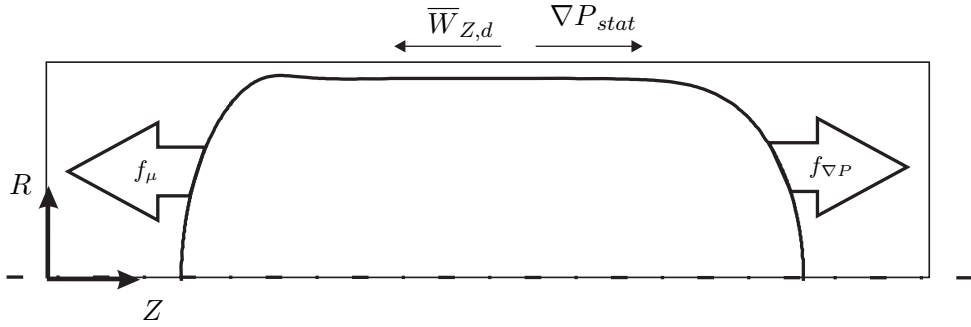
Figure 3.10: Schematic force balance at the steady-state free interface.

steady-state, the axial pressure force $f_{\nabla P}$ has to be in balance with the axial frictional force f_μ at the free interface. The solution converges towards the steady-state, when the sum of forces in axial direction

$$\begin{aligned}
f_{res} &= f_{\nabla P} + f_\mu, \\
f_{\nabla P} &= \sum_{E^{IF}} P^{IF} \ E^{IF} \ R^{IF} \left(\vec{n} \cdot \vec{e}_Z \right), \\
f_\mu &= \frac{-1}{Re_c} \sum_{E^{IF}} \frac{\Delta V^{IF}}{\Delta N_c} \ E^{IF} \ R^{IF} \left(\vec{n} \cdot \vec{e}_Z \right),
\end{aligned} \tag{3.11}$$

converges towards $f_{res} \to 0$ for $it \to \infty$. Convergence is achieved, when the relative sum

of forces decrease for at least three orders of magnitudes, cf. Ferziger and Peric (2008),

$$f_{res,rel} = \frac{f_{res,it}}{f_{res,1}} \leq 10^{-3}. \tag{3.12}$$

Here, $f_{res,1}$ represents the initial value for the first iteration $it = 1$. If the relative sum of forces does not fulfill the condition further iterations are performed, following the scheme in figure 3.7.

The steady-state velocity fields $\vec{U}_d$ and $\vec{U}_c$ are used for the simulation of the reactive mass transport.

3.2.4 Reactive mass transport

The transient reactive mass transport is simulated in the last step of the simulation concept. The discrete domains and the corresponding steady-state velocity fields $\vec{U}_d$ and $\vec{U}_c$ are used. A detailed description of the steps of the solution procedure, sketched in figure 3.11, is given
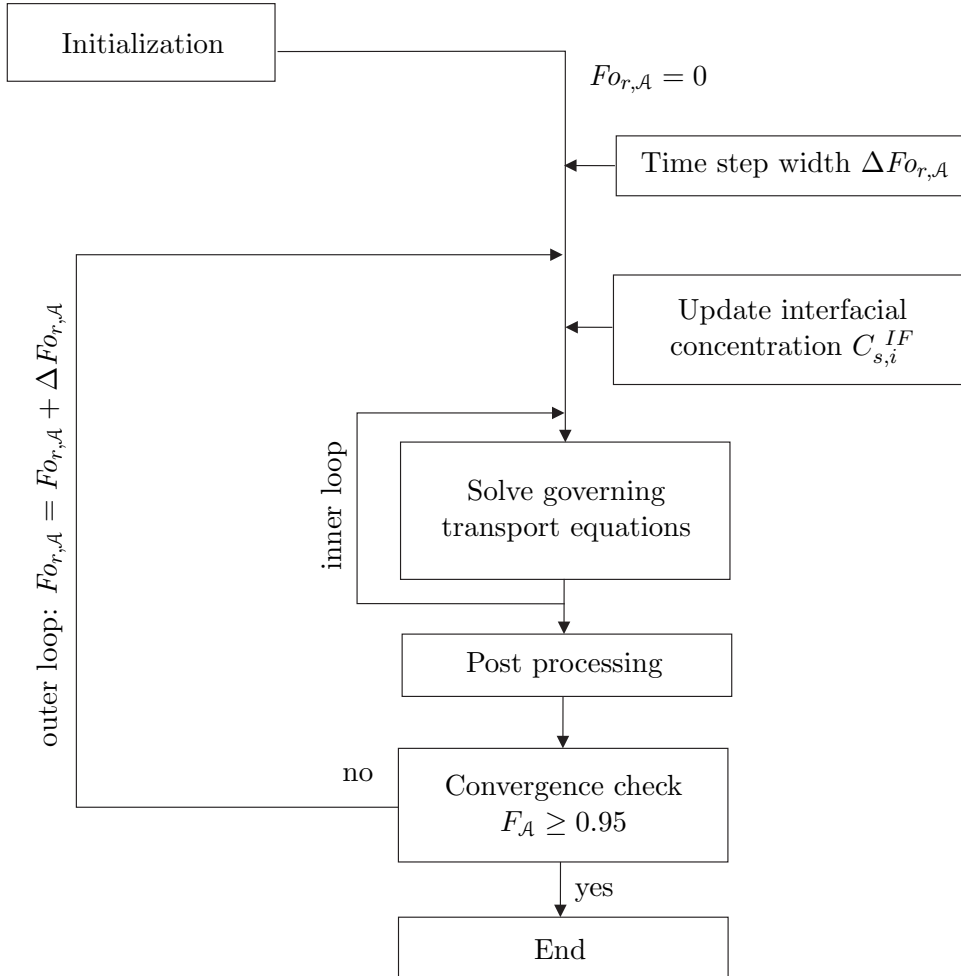
Figure 3.11: Scheme of the reactive mass transport algorithm.

below:

1. **Initialization**
   At the beginning, $Fo_{r,\mathcal{A}} = 0$ is set, the set of dimensionless parameters, i.e. $Pe_{r,\mathcal{A}}$, $\hat{D}_{\mathcal{A}}$, $m_{\mathcal{A}}$, λ, ψ and $Ha_{e,\mathcal{A}}$, is loaded, as well as the corresponding discrete domains, the steady-state

velocity fields of the assigned solvents $\vec{U}_e$ and $\vec{U}_r$, the initial field data and the boundary conditions for the concentration fields of solutes $\mathcal{A}$ and $\mathcal{B}$, see figure 3.12. The solutes cannot be transported through the capillary wall. The boundaries in flow direction are periodically coupled and the symmetry condition holds at the center line. Each solute is dissolved homogeneously in the raffinate respectively the extract solvent, at the beginning i.e. $C^0_{r,\mathcal{A}} = 1$ and $C^0_{e,\mathcal{B}} = 1$, if a chemical reaction is present, otherwise $C^0_{e,\mathcal{B}} = 0$ is prescribed.
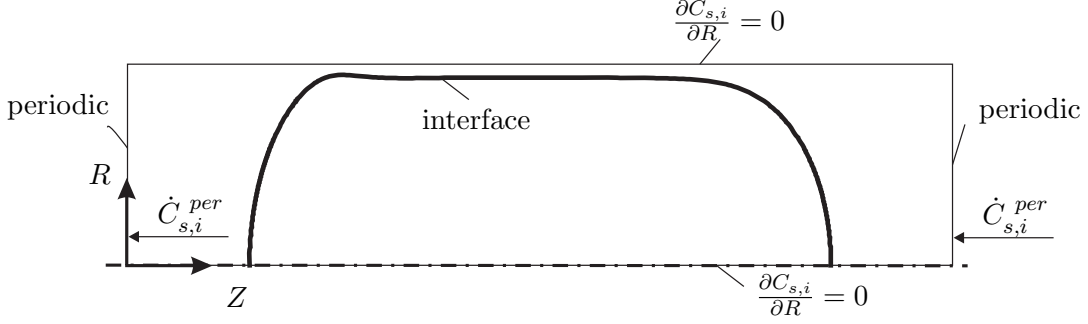
Figure 3.12: Boundary conditions for each solute for the simulation of the mass transport.

2. **Time step $\Delta Fo_{r,\mathcal{A}}$**

   Again, the explicit Euler-scheme is used for the temporal discretization, compare equation 3.3, and one global time step $\Delta Fo_{r,\mathcal{A}}$ is used for both domains. Adapted to the mass transport, only the diffusion number Di_j, for each cell j changes to $Di_j = \Delta T / \left(Pe_j E_j^2 \right)$, with Pe_j being the Péclet number assigned to the cell j. With the same stability criteria as for the steady-state two-phase flow, the global time step is derived, cf. Ferziger and Peric (2008), to

   $$\Delta Fo_{r,\mathcal{A}} = \frac{1}{Pe_{r,\mathcal{A}}} \min \left[\frac{Pe_{r,\mathcal{A}} E_{min}^2}{2} \min \left(1, \frac{1}{\hat{D}_\mathcal{A}}, \frac{\lambda}{\hat{D}_\mathcal{A}} \right), \min \left(\frac{2E_j}{|\vec{U}_j|} \right) \right]. \tag{3.13}$$

   Here, both solvents are engaged to determine one global time step. The global time step is kept constant for the transient simulation, since the underlying velocity fields and all other influencing parameters remain constant.

3. **Update interfacial concentrations**

   The concentrations of solutes $\mathcal{A}$ and $\mathcal{B}$ at the free interface are updated in relation to the interfacial conditions. The discrete formulation of the interfacial conditions is used, exemplary shown in figure 3.13 for solute i. Gradients normal to the interface are described by a linear approximation, according to the common numerical practice. By combination of both interfacial coupling constraints, formulations for the dimensionless interface concentration for the solute i are derived to

   $$C^{IF}_{r,i} = \frac{\frac{\hat{D}_i}{\Delta N_e} C^{ad}_{e,i} + \frac{1}{\Delta N_r} C^{ad}_{r,i}}{\frac{1}{m_i \, \Delta N_r} + \frac{\hat{D}_i}{\Delta N_e}}, \quad C^{IF}_{e,i} = \frac{\frac{\hat{D}_i}{\Delta N_e} C^{ad}_{e,i} + \frac{1}{\Delta N_r} C^{ad}_{r,i}}{\frac{1}{\Delta N_r} + \frac{m_i \, \hat{D}_i}{\Delta N_e}}. \tag{3.14}$$

   Here, $C^{IF}_{r,i}$ and $C^{IF}_{e,i}$ are the concentrations at the interface of the corresponding solvent and $C^{ad}_{r,i}$ and $C^{ad}_{e,i}$ are the concentrations adjacent to the free interface, i.e. at the cell centers next to the interface. Further, ΔN_r and ΔN_e are the interpolation distances from the interface to the cell centers.

Figure 3.13: Local discrete concentrations and gradients at the free interface, depicted for solute i.

The presence of solute $\mathcal{B}$ is restricted to the extract solvent, by engaging an appropriate distribution coefficient. Hence, the solubility is modeled based on the underlying physical principles.

The formulation of the interface concentrations of each domain is independent of the transport direction and the transport parameters, i.e. the diffusion coefficients. The coupling procedure is mass conservative, as the conservation of fluxes at the interface is taken into account.

4. **Solve transport equations**
   The transport equations are set up for each solute in both solvents and summarized in solute specific matrices. The Gauss-algebraic-multi-grid (GAMG) iterative solution algorithm is used for the iterative solution of the concentration fields of both solutes. Each matrix is solved until the residuum proves to be below $Res \leq 10^{-8}$. Both matrices are solved in series, each set up four times to compensate for the mesh skewness, in the inner iteration loop. Each time the equations are solved again four times with constant matrix coefficients to compensate for the mesh non-orthogonality and the mesh skewness, cf. Ferziger and Peric (2008).

   The following discretization schemes are used: As mentioned before the explicit Euler-scheme is used for the temporal discretization, providing first-order accuracy in time, while a linear approach is used for the discretization in space, ensuring second-order accuracy. A limiting approach, provided by *OpenFOAM*, cf. Weller et al. (1998), is used for

the convective term, to prevent oscillations during the numerical solution.

5. **Post processing**

   In each time step $\Delta Fo_{r,\mathcal{A}}$, the dimensionless local volumetric mass-transfer coefficient dSi, the dimensionless volumetric mass-transfer coefficient Si, and the local portions Si^P with $P = F, WF, B$, compare figure 2.1, are evaluated based on Fick's law, cf. Fick (1855), to

$$dSi = \frac{1}{Fo_{r,\mathcal{A}}} \sum_{\Delta Fo_{r,\mathcal{A}}} \left(\frac{\left. \frac{\Delta C_{r,\mathcal{A}}}{\Delta N_r} \right|^{IF}}{\Delta C_{\mathcal{A}}} E^{IF} R^{IF} \right) \Delta Fo_{r,\mathcal{A}}, \tag{3.15}$$

$$Si^P = \sum_{E^{IF,P}} (dSi), \tag{3.16}$$

$$Si = \sum_{E^{IF}} dSi. \tag{3.17}$$

The spatial distribution of the interfacial portions is derived from the saddle points with the tangential interfacial velocity $V^{IF}(Z) = 0$. In the formulations, the discrete gradient $\Delta C_{r,\mathcal{A}}/\Delta N_r|^{IF}$ at the interface is used. Further, the relative wall-film concentration is evaluated to

$$\Gamma = \frac{1}{Fo_{r,\mathcal{A}}} \frac{1}{\sum_{j^{WF}} A_j^{WF} R_j^{WF}} \sum_{\Delta Fo_{r,\mathcal{A}}} \left[\left(\sum_{j^{WF}} C_{sc,\mathcal{A},j}^{WF} A_j^{WF} R_j^{WF} \right) \Delta Fo_{r,\mathcal{A}} \right], \tag{3.18}$$

with j^{WF} assigning the cells inside the wall film, with cell area A_j^{WF}, the radial position R_j^{WF}, the dimensionless concentration in the solvent assigned to the continuous phase inside the wall film $C_{sc,\mathcal{A},j}^{WF}$.

6. **Convergence check**

   At the end of each iteration loop, the extraction rate $F_{\mathcal{A}}$ is calculated to evaluate the progress of the transient process, compare equation 1.17. Convergence is achieved, when $F_{\mathcal{A}} \geq 0.95$ is reached. If the extraction rate is below the threshold, another iteration loop is performed.

3.3 Numerical tests

Numerical tests are performed to validate the implementation of the interface-tracking method and to examine the numerical quality. First, the steady-state two-phase flow and then the reactive mass transport are investigated.

3.3.1 Steady-state two-phase flow

The coupling scheme and the pressure loop are investigated using the theoretical test case of a parallel gap flow between two semi-infinite plates, before the slug flow is examined.

Parallel flow between two semi-infinite plates

The incompressible, immiscible and Newtonian steady parallel two-phase flow between two semi-infinite plates with a plain interface is chosen for the validation of the pressure driven flow and the coupling scheme, since an analytical steady-state solution is known, see e.g. Bird et al. (2007). The scaled two-dimensional test case is sketched in figure 3.14, including geometric properties,

velocities, flow parameters and boundary conditions. A Cartesian coordinate system fixed to
the interface (Z, Y) with velocities (W, V) is used as sketched in the problem definition. The gap
height g, the average gap velocity $\overline{w}$ and the according flow parameters are used as references
for the scaling. The interface-tracking method is applied to the test case. An Cartesian mesh,
with a spatial reference resolution of $E^{IF} = 10^{-2}$, is used to simulate the two-dimensional flow.
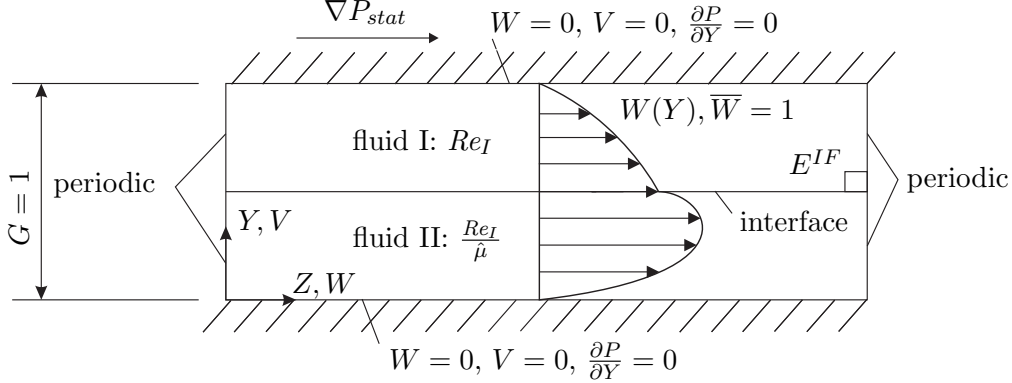The dimensionless analytical solution for a straight interface is

Figure 3.14: Two-dimensional parallel gap flow between two semi-infinite plates, including the
geometric properties, velocities, flow parameters and boundary conditions.

$$W_{I,ana}(Y) = \frac{1}{2}\nabla P_{stat} Re_I \left(-Y^2 + \frac{3}{2}Y - \frac{1}{1+\hat{\mu}}(0.5 - Y) \right), \qquad (3.19)$$

$$W_{II,ana}(Y) = \frac{1}{2}\nabla P_{stat} Re_I \frac{1}{\hat{\mu}} \left(-Y^2 + \frac{1}{2}Y + \frac{1}{1+\frac{1}{\hat{\mu}}}Y \right). \qquad (3.20)$$

The spatial velocity profiles $W(Y)$ depend on the ratio of the viscosities $\hat{\mu} = \mu_I/\mu_{II}$ and the
Reynolds number Re_I. For comparison the numerical and the analytical velocity profiles for
$W_{num}(Y)$ and $W_{ana}(Y)$ for $Re_I = 1$, $\hat{\mu} = 0.1$, and $Re_I = 20$, $\hat{\mu} = 2$ are plotted in figure 3.15.
The simulation results are hardly influenced by the spatial discretization and perfect agreement
is achieved. The examination of the influence of the spatial distribution is therefore not presented
here. The maximum local deviation of the solutions

$$\epsilon_W = \left| 1 - \frac{W_{num}(Y)}{W_{ana}(Y)} \right| \qquad (3.21)$$

is as little as $\epsilon_W \leq 0.1\%$ in both phases. Further, the absolute static pressure gradients of the
numerical solutions give $|\nabla P_{stat,num}| = 4.381$ and $|\nabla P_{stat,num}| = 0.875$, with a relative deviation
of $\epsilon_{\nabla P} \leq 0.01\%$ compared to the analytical solution, with $\epsilon_{\nabla P}$ defined analogous to equation
3.21. The implementations of the coupling scheme and the pressure loop appear to be perfectly
validated.

Slug flow

The implementation is now applied to the slug flow. A slug flow configuration with $Ca_c = 10^{-2}$,
$Re_c = 10$, $\hat{\mu} = 1$, $L_{pe} = 4$ and $\hat{V} = 1$ is chosen. Further, the spatial resolution at the free
interface of $E^{IF} = 4 \cdot 10^{-3}$ is prescribed. The flow topology, shown in figure 3.16, is in good
agreement with reports from literature, compare with the simulation results by Dittmar (2015)
illustrated in figure 1.4b. The convergence of the numerical simulation model can be detected
from the evolution of the relative sum of forces $f_{res,rel}$ at the interface, plotted as a function of
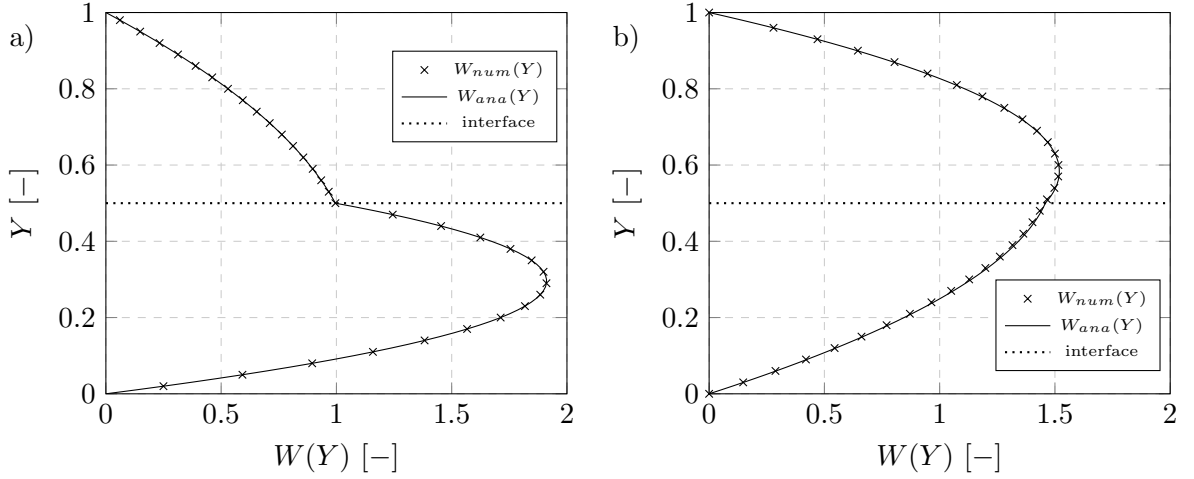
Figure 3.15: Local gap flow velocities $W_{num}(Y)$ and $W_{ana}(Y)$ as function of the coordinate Y: a) Comparison of velocity distributions for $Re_I = \overline{w}g/\mu_I = 1$ and $\hat{\mu} = 0.1$; b) Comparison of velocity distributions for $Re_{II} = 20$ and $\hat{\mu} = 2$.
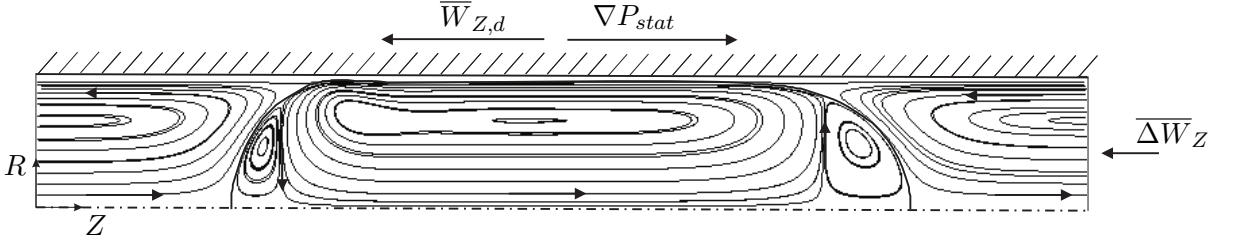

Figure 3.16: Slug flow stream lines resulting from the steady-state two-phase flow algorithm for $Ca_c = 10^{-2}$, $Re_c = 10$, $\hat{\mu} = 1$, $L_{pe} = 4$ and $\hat{V} = 1$ in half section.

the relative number of iterations it/it_{max} in figure 3.17a. The sum of forces decreases by three orders of magnitude as the number of iterations increases and the solution converges towards a steady-state solution, cf. Ferziger and Peric (2008). The absolute value of the static pressure gradient $|\nabla P|_{stat}$ at the end of the simulation is practically independent of the spatial resolution at the free interface E^{IF}, see figure 3.17b. This can be derived from the small slope of the linear regression. The mesh independent solution can be extrapolated from the regression for $E^{IF} = 0$ and the largest deviation is about $\epsilon_{\nabla P,max} = 5\%$ for the lowest resolution. Hence, the simulation results are hardly influenced by the spatial discretization. The magnitude of the steady-state static pressure gradient $|\nabla P|_{stat}$ of the reference flow configuration is compared to the simulation results from Dittmar (2015), which provide the steady-state interface. Moreover, the experimental correlation of Jovanović et al. (2011) is included for this comparison, given in dimensionless form by

$$|\nabla P|_{stat} = \left| \frac{\Delta P}{L_{pe}} \right| = \frac{8\hat{\mu} \left(\frac{1}{\frac{1}{\varsigma_d}+1} \right) \overline{W}_{Z,d}}{Re_c \left(1 - \overline{H} \right)} + \frac{32 \left(\frac{1}{\frac{1}{\varsigma_d}+1} \right)}{Re_c} + \frac{7.16}{L_d} \left(3Ca_c \right)^{(2/3)} \frac{1}{Re_c^2 \, Ca_c}, \qquad (3.22)$$

with the dimensionless length of the disperse phase $L_d = l_d/d$. The slug length is directly extracted from the interface. In figure 3.18a all results for the static pressure gradient are plotted as a function of the Reynolds number Re_c. The simulation results of Dittmar (2015) show a deviation of $\epsilon_{\nabla P} \leq 0.1\%$, while also the correlation is in perfect agreement. Further, the change of the static pressure gradient due to a change of the viscosity ratio, the volumetric
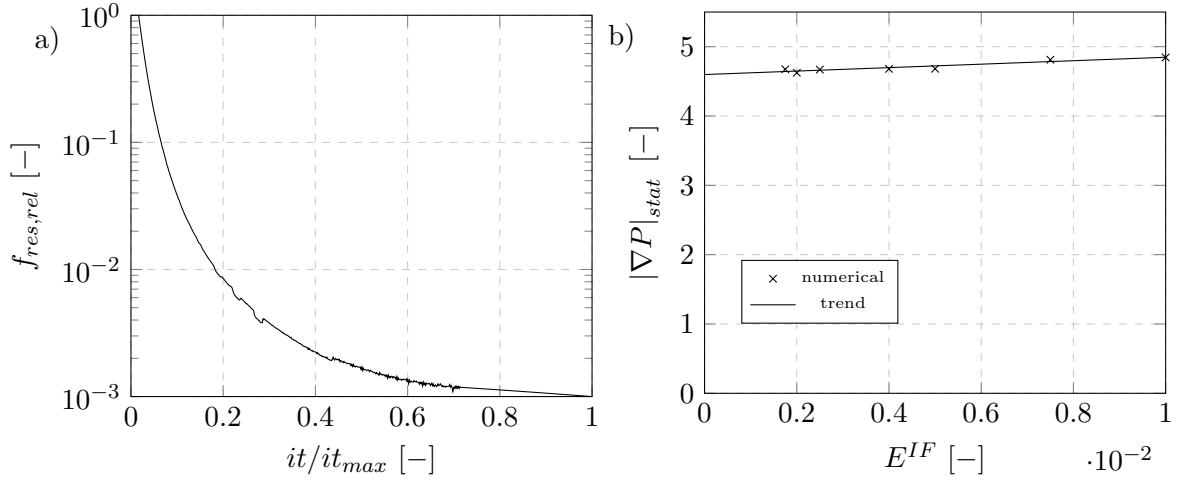
Figure 3.17: Slug flow steady-state two-phase flow algorithm: a) Relative sum of forces $f_{res,rel}$ as function of the relative number of iterations it/it_{max}; b) Driving static pressure gradient $|\nabla P|_{stat}$ as function of the spatial resolution E^{IF}.

Figure 3.18: Slug flow steady-state two-phase flow algorithm: a) Comparison of the static pressure gradient $|\nabla P|_{stat}$ as a function of the Reynolds number Re_c; b) Comparison of the static pressure gradient $|\nabla P|_{stat}$ as a function of the viscosity ratio $\hat{\mu}$.

ratio and the element length is investigated and compared to the experimental correlation of Jovanović et al. (2011). The results of this comparison are collected in figures 3.18b, 3.19a, and 3.19b. A maximum error of $\epsilon_{\nabla P} = 38\%$ is present in comparison to the correlation of Jovanović et al. (2011) for the lowest viscosity ratio. All trends are predicted properly by the numerical method. It must be kept in mind that the experimental correlation, equation 3.22, may also contain errors to some degree. The perfect agreement of the present simulations with the simulations by Dittmar (2015), see figure 3.18a, gives confidence that, despite the different numerical methods, both simulations reflect the physics correctly. The corresponding driving pressure gradients from the reference simulation model, cf. Dittmar (2015), are further in a perfect agreement and not shown therefore in the diagrams.
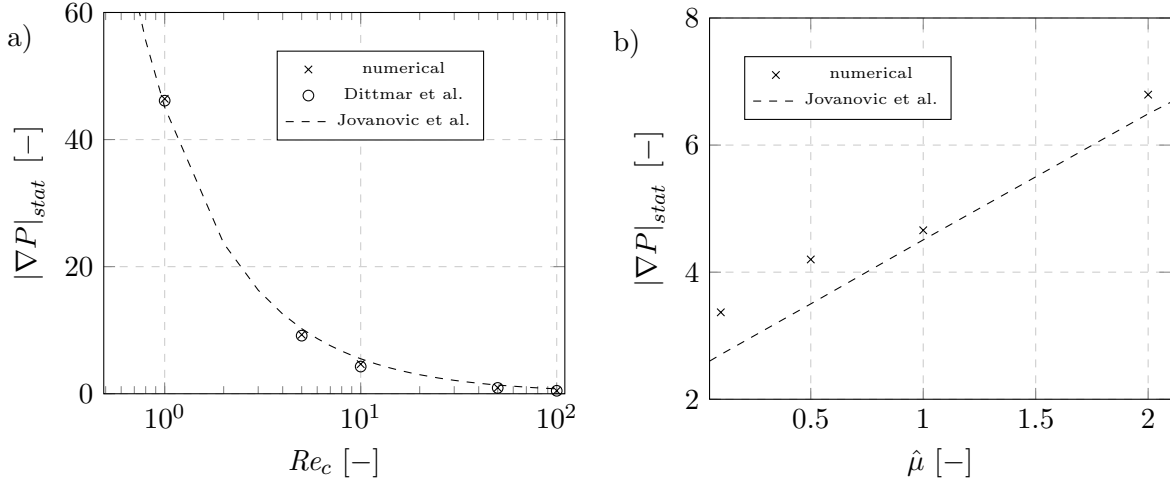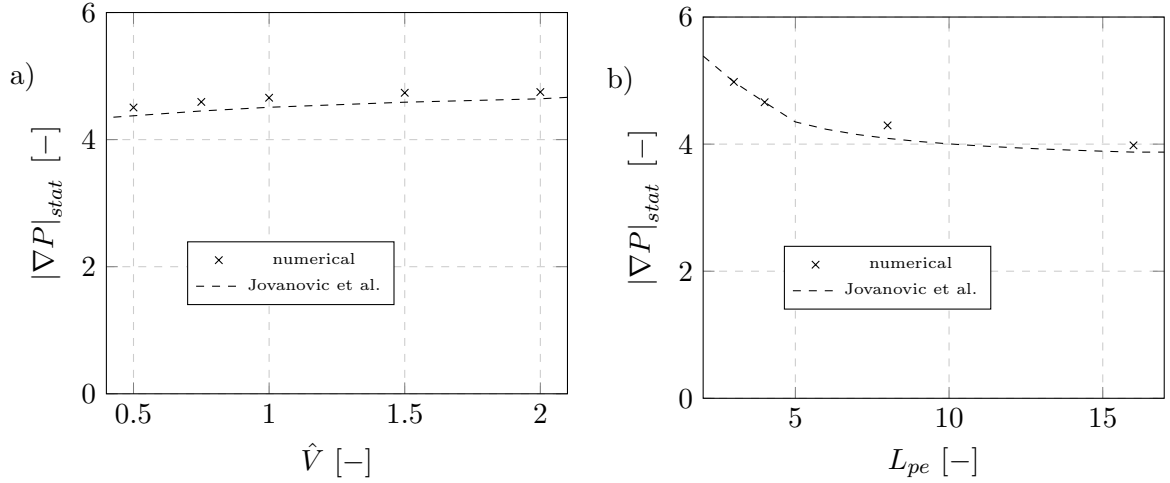
Figure 3.19: Slug flow steady-state two-phase flow algorithm: a) Comparison of the static pressure gradient $|\nabla P|_{stat}$ as a function of the ratio of volumetric flow rates $\hat{V}$; b) Comparison of the static pressure gradient $|\nabla P|_{stat}$ as a function of the periodic element length L_{pe}.

3.3.2 Reactive Mass Transport

Similar to the two-phase flow, the reactive mass transport is validated in two steps: The reactive mass transport algorithm is validated on basis of the mass transport in a parallel gap flow, where an analytical solution is available. Further, the method for the mass transport is applied to the slug flow to study the evolution of the volumetric mass-transfer coefficient and the influence of the spatial resolution.

Reactive mass transport in parallel flow

Due to the presence of an analytical solution the test case of reactive mass transport in a parallel flow with a plane interface is chosen for the validation of the mass transfer coupling scheme and the influence of the reaction rate. The test case, including boundary and initial conditions, geometric as well as the dimensionless parameters, is presented in figure 3.20. Solute $\mathcal{A}$ enters the raffinate solvent and is then transferred into the extract solvent, where is can react with solute $\mathcal{B}$. The gap height g, the constant velocity profile w, and the transport and chemical parameters of solute $\mathcal{A}$ are used for scaling. A spatial resolution of $E^{IF} = 4 \cdot 10^{-3}$ is used. For
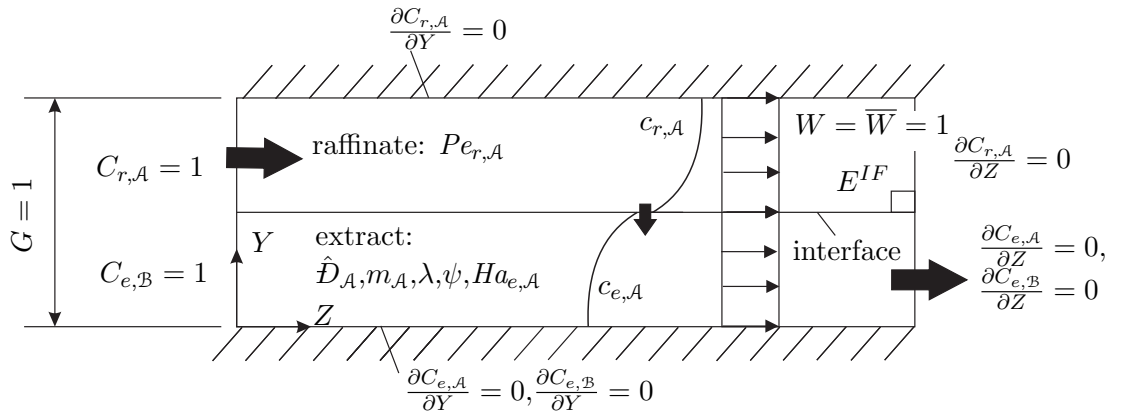

Figure 3.20: Two-dimensional reactive mass transport in parallel flow, including variables, boundary conditions, and dimensionless parameters.

a large ratio of convection and diffusion, i.e. for a large Péclet number, an analytical solution

can be derived, cf. Wolf (1998) or Crank (1976). The analytical solution for the concentration field is

$$C_{r,\mathcal{A},ana}(Z,Y) = \frac{1}{1 + m_\mathcal{A}} \left[1 + m_\mathcal{A} \; \mathrm{erf} \left(\frac{Y - 0.5}{4\sqrt{\frac{Z}{Pe_{r,\mathcal{A}}}}} \right) \right], \tag{3.23}$$

$$C_{e,\mathcal{A},ana}(Z,Y) = \frac{m_\mathcal{A}}{1 + m_\mathcal{A}\sqrt{\hat{D}_\mathcal{A}}} \left[1 + m_\mathcal{A} \; \mathrm{erf} \left(\frac{0.5 - Y}{4\sqrt{\frac{Z\hat{D}_\mathcal{A}}{Pe_{r,\mathcal{A}}}}} \right) \right]. \tag{3.24}$$

The analytical solution for the concentration of solute $\mathcal{A}$ depends on the Péclet number $Pe_{r,\mathcal{A}}$, the ratio of the diffusion coefficients $\hat{D}_\mathcal{A}$, and the distribution coefficient $m_\mathcal{A}$. Two configurations are investigated to study the coupling and the influence of the reaction rate. For the physical mass transfer, $Pe_{r,\mathcal{A}} = 10^3$, $m_\mathcal{A} = 2$, and $\hat{D}_\mathcal{A} = 2$ are chosen, while a quasi first-order chemical reaction is used with the additional parameters $\psi = 10^{-3}$, $\lambda = 1$ and $Ha_{e,\mathcal{A}} = 10^4$ for the investigation of the influence of a chemical reaction. Here, the concentration fields have to converge against the analytical solutions for $\hat{D}_\mathcal{A} \to \infty$ in conjunction with the instantaneous chemical-reaction system of quasi first order. The concentration profiles along the Y-axis are compared to the analytical solutions at a certain position $Z = 0.5$, see figure 3.21a and 3.21b. Perfect agreement is achieved, as the maximum error ϵ_C, defined analogously to equation 3.21,
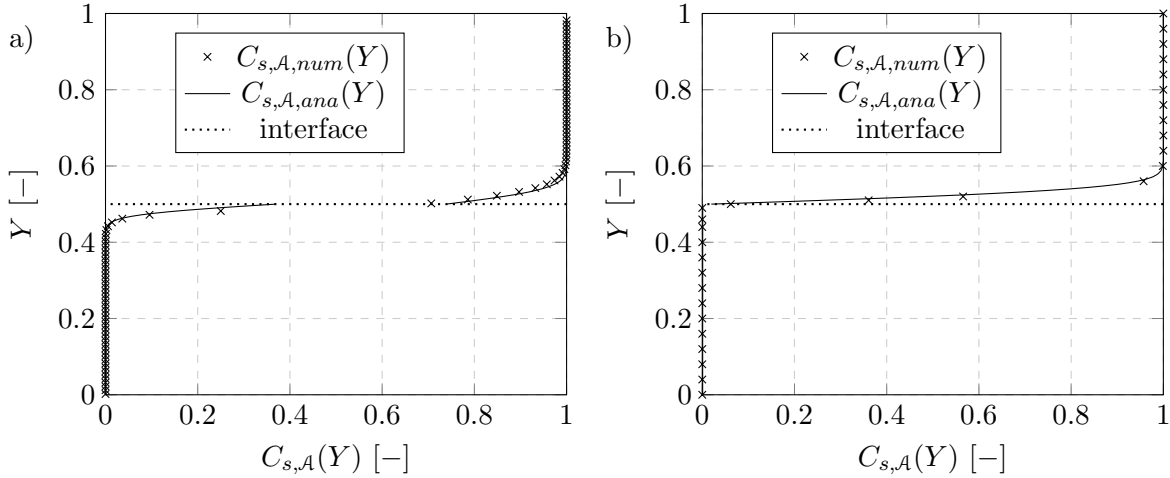

Figure 3.21: Local parallel flow concentration profile $C_{s,\mathcal{A},num}$ and $C_{s,\mathcal{A},ana}$ as function of the coordinate Y: a) Physical mass transport with $Pe_{r,\mathcal{A}} = 10^3$, $\hat{D}_\mathcal{A} = 2$, $m_\mathcal{A}=2$. b) Reactive mass transport with $Pe_{r,\mathcal{A}} = 10^3$, $\hat{D}_\mathcal{A} = 2$, $m_\mathcal{A}=2$, $\lambda = 1$, $\psi = 10^3$, $Ha_{e,\mathcal{A}} = 10^4$.

is as low as $\epsilon_C \leq 1\%$ for both cases. Further, the numerical method allows access of the local values at the free interface for the derivation of the spatial distribution of the local dimensionless volumetric mass-transfer coefficient dSi along the interface, i.e. along the dimensionless Z-axis, normalized to its maximum value dSi_{max}. The result is given in figure 3.22 for $Fo_{r,\mathcal{A}} \to \infty$, such that in all cases a steady-state solution is attached, since the extraction rate cannot be used as abort criteria. Both cases provide almost the same normalized spatial distribution. The deviations to the analytical solution, defined again analogously to equation 3.21, are $\epsilon_{Si,max} = 3\%$ and $\epsilon_{dSi,max} = 18\%$. The largest deviation appears near to the singular point at the inlet, i.e. for $Z = 0$, as expected. In summary, the implementation of the numerical algorithm for the simulation of the reactive mass transfer appears to be valid and suitable for the investigation of
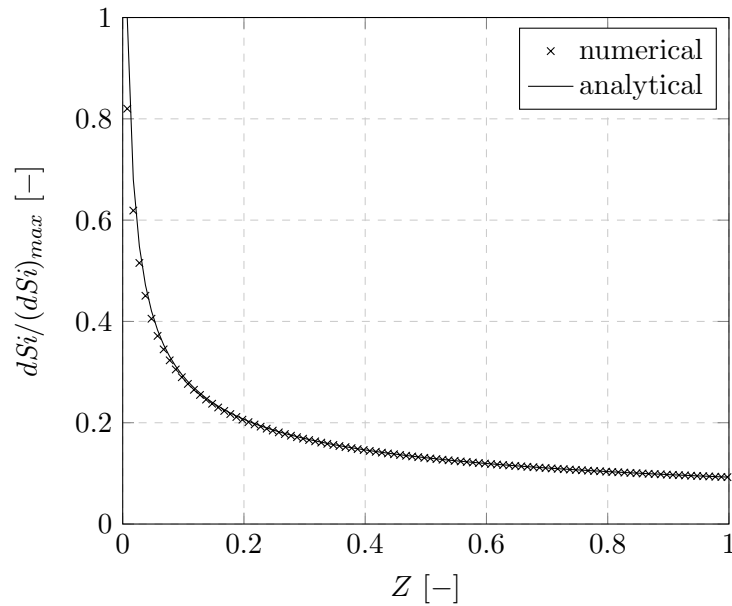
Figure 3.22: Parallel flow validation of reactive mass-transport algorithm: Local dimensionless volumetric mass-transfer coefficient dSi, normalized to its maximum $(Si)_{max}$ as function of the dimensionless coordinate Z.

the local mass transfer at the free interface.

Slug flow

The reactive mass transport algorithm is applied to the slug flow to study the temporal evolution and the influence of the spatial discretization. Corresponding to the two-phase flow tests, the slug flow configuration with $Ca_c = 10^{-2}$, $Re_c = 10$, $\hat{\mu} = 1$, $L_{pe} = 4$ and $\hat{V} = 1$ is used as basis for the simulation of the reactive mass transport, with and without chemical reaction, and a spatial resolution of $E^{IF} = 4 \cdot 10^{-3}$. The raffinate solvent is assigned to the disperse phase. Firstly, the temporal evolution of the mass transport is investigated for the limiting parameters $Pe_{r,\mathcal{A}} = 10^5$, $m_{\mathcal{A}} = 1$ and $\hat{D}_{\mathcal{A}} = 1$, without chemical reaction, i.e. $C^0_{e,\mathcal{B}} = 0$ (I). The extraction rate $F_{\mathcal{A}}$ is plotted as a function of the Fourier number $Fo_{r,\mathcal{A}}$ in figure 3.23a, simulated until $F_{\mathcal{A}} = 1$ in contrast to the threshold presented for the description of the algorithm. The extraction rate increases towards $F_{\mathcal{A}} = 1$, while the relative amount of transferred mass decreases as time increases. The extraction rate $F_{\mathcal{A}} = 0.95$ is reached at approximately half of the extraction time and the second half of the extraction time is spent for the last 5% of the transient process. The transient process is further characterized by the dimensionless volumetric mass-transfer coefficient Si, that is plotted against the extraction rate $F_{\mathcal{A}}$ in figure 3.23b. Coming from infinity, the graph decreases and converges towards a limiting value, as expected from other results in literature, cf. Clift et al. (1978). The value $Si(F_{\mathcal{A}} = 0.95)$ deviates less than $\epsilon_{Si} < 4\%$ from the limiting value for $F_{\mathcal{A}} = 1$. In conclusion, in the following the dimensionless volumetric mass-transfer coefficient $Si(F_{\mathcal{A}} = 0.95)$ represents the mass transport process at good accuracy. This result justifies the use of $F_{\mathcal{A}} = 0.95$ as abort criteria for the reactive mass-transport algorithm.

At last, the influence of the spatial discretization onto the reactive mass transport is studied. Therefore, two additional configurations are considered: The case of moderate convection (II), i.e. $Pe_{r,\mathcal{A}} = 10^4$, $m_{\mathcal{A}} = 1$, $\hat{D}_{\mathcal{A}} = 1$, and the same case with additionally a fast second-order chemical reaction (III), i.e. $\psi = 1$, $\lambda = 1$, and $Ha_{e,\mathcal{B}} = 10^4$. The evolutions of the dimensionless volumetric mass-transfer coefficients are shown in figure 3.23b and the dimensionless volumetric
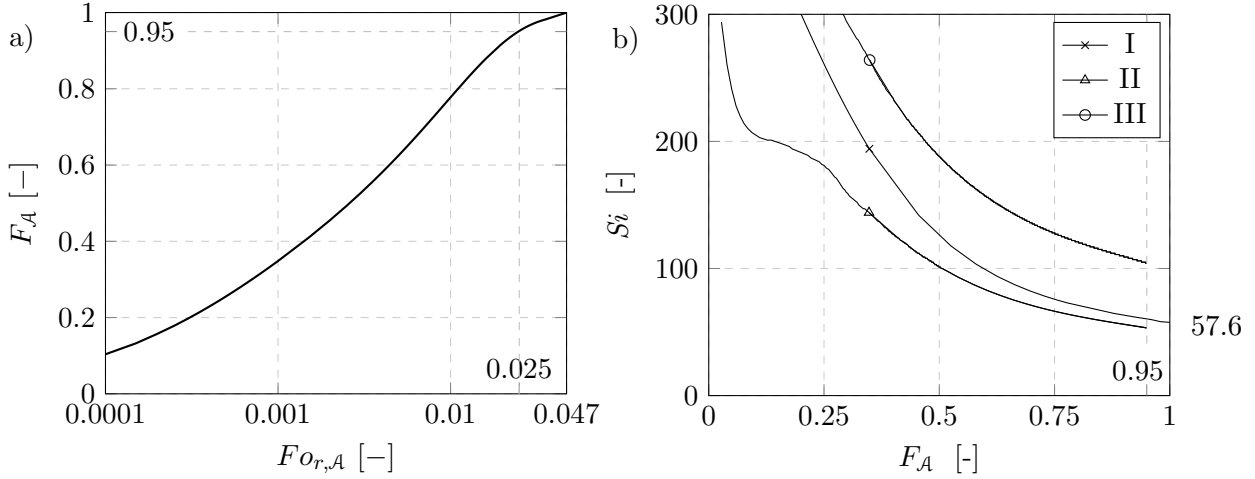
Figure 3.23: Slug-flow reactive mass-transport algorithm: a) Extraction rate $F_{\mathcal{A}}$ as a function of the Fourier number $Fo_{r,\mathcal{A}}$ for test case (I); b) Dimensionless volumetric mass-transfer coefficient Si as a function of the extraction rate $F_{\mathcal{A}}$ for all test cases.
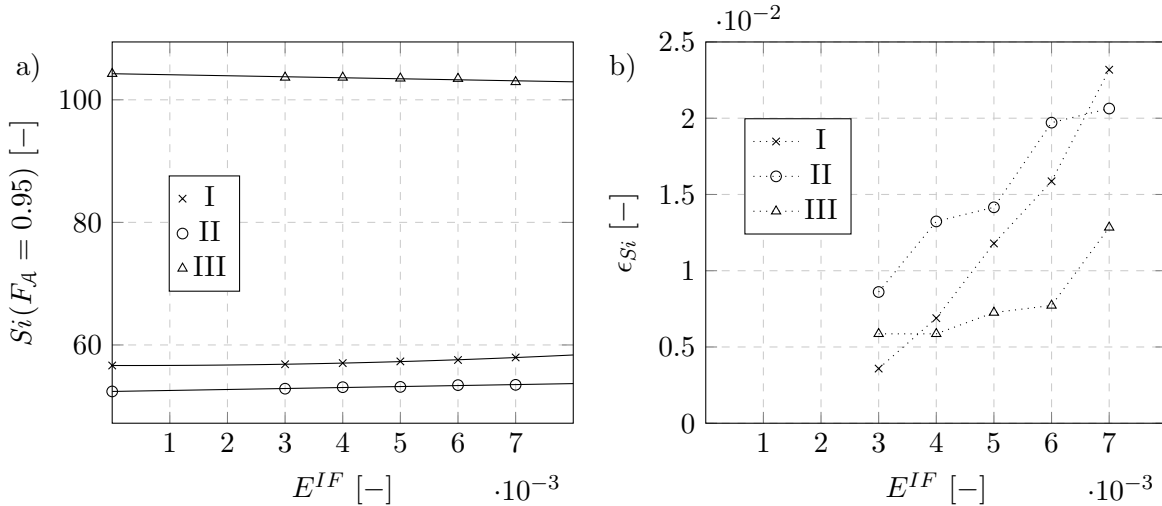

Figure 3.24: Slug-flow reactive mass-transport algorithm: a) Dimensionless volumetric mass-transfer coefficient at the end of the transfer process $Si(F_{\mathcal{A}} = 0.95)$ as a function of E^{IF} for all test cases; b) Deviation ϵ_{Si} as a function of the spatial resolution E^{IF} for all test cases.

mass-transfer coefficient $Si(F_{\mathcal{A}} = 0.95)$ is plotted in figure 3.24a as function of the spatial resolution $Si(E^{IF} = 0)$ for the three cases. The extrapolated values for $E^{IF} = 0$ represent the mesh-independent solutions, cf. Ferziger and Peric (2008). The mesh independent solution $Si(E^{IF} = 0)$ is used for the calculation of the error

$$\epsilon_{Si} = \left| \frac{Si(E^{IF})}{Si(E^{IF} = 0)} \right|, \tag{3.25}$$

defined analogue to equation 3.21, shown in figure 3.24b. The symbols are connected by dotted lines to allow for a graphical interpretation of the graphs. The configuration with intense convection (I) shows the strongest dependency on the spatial discretization, while the other two cases with moderate convection (II), and a fast chemical reaction (III), show a weaker dependency. Considering the simulation time, that increases about quadratically when the spatial resolution is increased, cf. Anderson and Wendt (2009), and the requirement to arrange at least five cells in the radial direction in the wall film at each position Z, results in the choice of a spatial

resolution of $E^{IF} = 4 \cdot 10^{-3}$. With this spatial resolution the transient reactive mass transfer at the free interface is sufficiently represented, giving an overall error of $\epsilon_{Si,max} < 2\%$.

In summary, the interface-tracking method and its implementation proves to represent the reactive mass transport and the local mass transfer in the liquid/liquid slug flow micro-capillary reactor at very good accuracy almost independent of numerical diffusion. The benefit of the methodical effort is emphasized here, since the effect of numerical diffusion is minimized compared to similar studies using the volume-tracking approach, cf. Kashid et al. (2010) or Di Miceli Raimondi et al. (2008).

4

Test systems

The evolution of the volumetric mass-transfer coefficient in the liquid/liquid slug-flow micro-capillary reactor is examined experimentally for two test systems and compared to the results of the adapted simulation model. The used experimental setup and the measurement procedure are described and the flow, transport and chemical parameters are derived. Finally, the experimental volumetric mass-transfer coefficients are compared to the adapted numerical simulation model.

4.1 Experimental setup

The experimental setup is in accordance with the structure of a two-phase micro channel, compare section 1.3.1. A flow diameter of $d = 1$ mm is used throughout the slug-flow micro-capillary reactor and the operation with a liquid/liquid extraction system consisting of a polar and a non-polar liquid solvent, i.e. practically immiscible, is given. A T-junction, manufactured at TU Dortmund, and made of Poly-Ether-Ether-Ketone (PEEK), is used for the generation of the slug flow in two different arrangements. Figure 4.1 shows the two arrangements with the main measurements and phase feeds. In configuration (a) both phases meet in counter-flow, while in configuration (b) a co-flow arrangement is used. For configuration (b) a hypodermic needle of steel is introduced into the T-junction, which has an inner diameter of 0.6 mm with a tip cut normal to the axis to ensure a stable generation of the slug flow. The developed co-flow arrangement is emerges from the evaluated experimental data in conjunction with the physical mass-transfer system and shows a high influence to the data evaluation and the comparison with the simulated data, compare section 4.4. The phases enter the junction with the volumetric flow rates of the disperse phase $\dot{V}_d$ and the continuous phase $\dot{V}_c$, with $\dot{V}_{tot} = \dot{V}_d + \dot{V}_c$. A piston pump module, Fischer Scientific KDS200P with Fortuna Optima glass syringes, is used. The residence-time unit consists of a straight Fluorinated-Ethylene-Propylene (FEP) tube, CS-
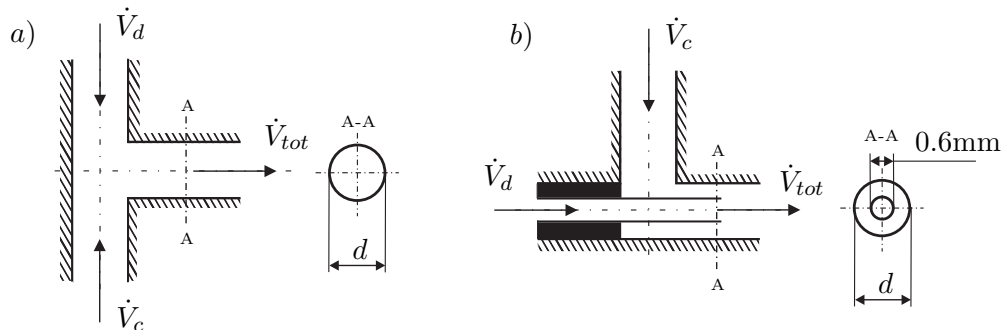

Figure 4.1: Mixing junction arrangements: a) Counter-flow T-junction configuration; b) Co-flow T-junction arrangement, with a hypodermic needle, with tip cut normal to the axis.

Chromatographie Service Gmbh Germany, a transparent polymeric compound, with constant circular cross-section. Thus, the continuous phase is formed by the nonpolar liquid and the polar liquid forms the disperse phase.

The separation unit is developed by Hohmann et al. (2016), manufactured at TU Dortmund, and engages the wetting properties for the phase splitting. As shown in the sketch in figure 4.2, the flow pattern enters the splitting unit through a connection made of PEEK and is directed onto a steel sleeve, that separates the phases. The steel sleeve is preferentially wetted by the polar phase and passes the sleeve preferentially, while the nonpolar phase is directed into the opposed outlet. The wetting properties of the surfaces at the outlets, in form of steel and Polychlortriflourethylen (PCTFE), supports the splitting. The degree of separation is better than 98% and the time scale for separation is small compared to the time for mass transfer in the residence-time unit, cf. Kurt et al. (2016).

The whole setup is operated inside a temperature controlled water bath to ensure isothermal
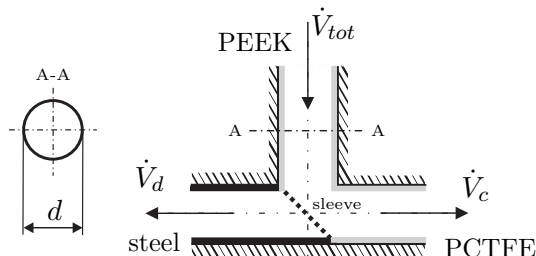
Figure 4.2: Schematic sketch of separation unit, with the disperse phase being the polar liquid.

conditions at $20°C$. Due to the small diameter of the residence-time unit, an almost uniform temperature distribution can be assumed inside the cross-sectional flow area, cf. Jensen (1999); Scheiff (2015).

Additionally, a camera is present for the optical measurement of the periodic-element length, see figure 4.3. Photos are taken during the steady-state operation and an automated algorithm is used to evaluate the length of the periodic elements. For this, the position of the free interface is detected from light refection. An automated algorithm evaluates the distance of two consecutive
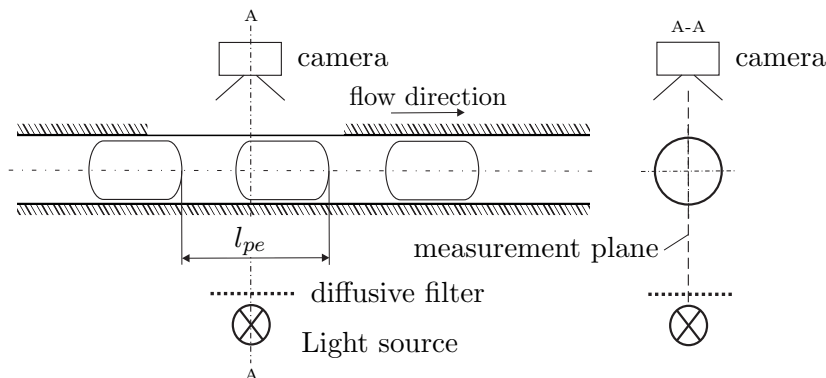
Figure 4.3: Schematic sketch of the camera unit for the optical measurement of the periodic element length. The measurement plane coincides with the axis of the capillary to exclude the influence of light reflection.

slug fronts along the center-line of the capillary, providing the length of the periodic element l_{pe}. The measurement along the center-line excludes the projection error due to the light reflection of the circular cross-sectional geometry. The estimated relative measurement error for

the measurement of the length is about 0.1% of the length of a periodic element, resulting from the projection onto the digital camera chip, and the camera unit appears to be sufficient for the investigation.

The experimental setup with related units and the single mechanical device show tolerances, that are in the same range as in other micro reactor investigations involving multiphase applications, see e.g. Kashid et al. (2007b), Scheiff et al. (2011), Jovanović et al. (2012), Hohmann et al. (2016), or Kurt et al. (2016). Accordingly, all tolerances are assumed to be within sufficient limits for the present measurement purpose and only checked specifically when errors or doubts occur.

4.2 Measurement procedure

The measurement procedure is illustrated in figure 4.4. The role of the phases is assigned to the solvents by the initial presence of the solutes $\mathcal{A}$ and $\mathcal{B}$, corresponding to the initial dilute concentrations $c_{r,\mathcal{A}}^0$ and $c_{e,\mathcal{B}}^0$, that are set with a laboratory balance, which provides a sufficient tolerance for the solvents preparation. The transferred amount of mass is evaluated from taken samples for the corresponding section length l_S, varied between the minimum length l_{min} and the reactor length l_{re}. The minimum length l_{min} is chosen as close as possible to the generation unit, ensuring a developed slug flow is ensured before the separation unit is entered. The reactor length l_{re} is derived from the design criterion for a extraction rate of $F_{\mathcal{A}} = 0.95$, that is derived initially from a separate set of experiments. The adaption of the length of the polymeric capillary appears to be easy adaptable with in combination with the modular structure, with an acceptable tolerance of 1 mm. The transferred amount of solute $\mathcal{A}$
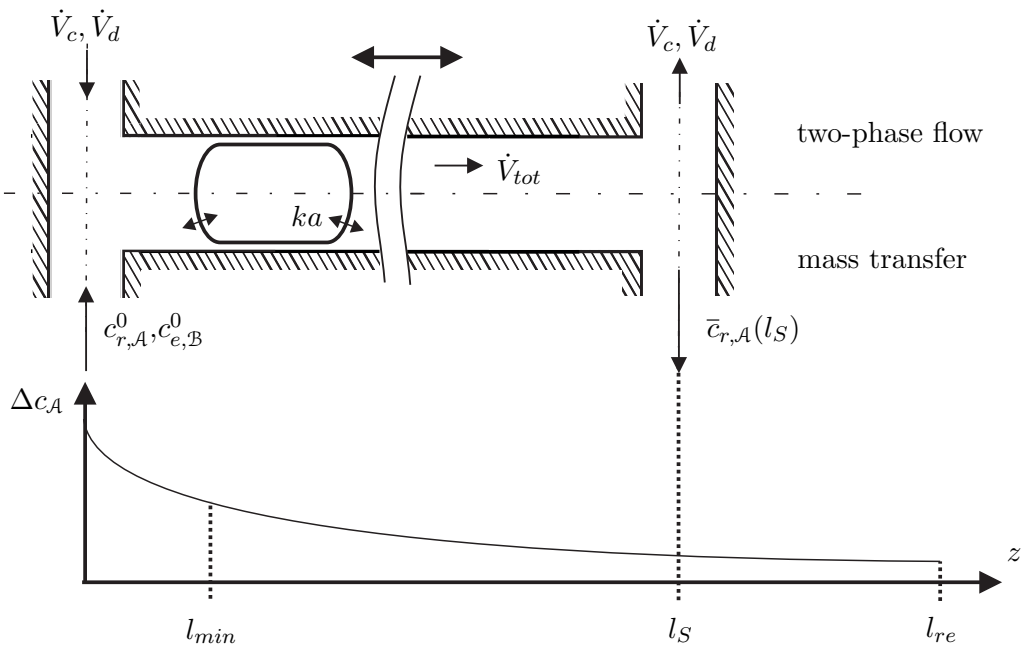

Figure 4.4: Schematic measurement procedure: Access evolution of the transfer process by adaption of the reactor section length, at constant total volumetric flow rate and ratio of volumetric flow rates.

is evaluated at the outlet of the micro reactor for each reactor section l_S via chemical analysis

for the given mass-transfer test system, based on a representative volumetric amount of the taken samples, i.e. at least 2 ml. The volumetric average concentration $\bar{c}_{r,\mathcal{A}}(l_S)$ of solute $\mathcal{A}$ is evaluated considering at least three samples for each section length during three separate runs, ensuring a reasonable accuracy of the measurement. The corresponding mass-transfer time can be derived from $\tau_m(l_S) = 4\dot{V}_{tot}/(d^2\pi l_S)$, with $\dot{V}_{tot} = \dot{V}_d + \dot{V}_c$ as total volumetric flow rate. The volumetric mass-transfer coefficient $ka(\tau_m)$ and the extraction rate $F_{\mathcal{A}}(\tau_m)$ are evaluated based on the slug flow modeling approach, presented in chapter 2. The possible measurement error, that appears from the adaption of the section length has only a weak influence, compare with used section length in section 4.3.

4.3   Mass-transfer systems and process parameters

Two mass-transfer test systems, a physical and a reactive test system, are chosen for the investigation of the evolution of the mass transfer with the described experimental setup and in conjunction with the measurement procedure. The flow, transport and chemical parameters of the mass-transfer systems, experimental and process conditions, and sample analysis are described below for each test system.

4.3.1   Physical mass transfer

The physical mass transfer is studied using a standard mass-transfer system, proposed by Misek and Berger (1985), consisting of butyl acetate (CAS:123-86-4), demineralized water, and acetone (CAS:67-64-1). In the present application, the acetone is initially dissolved in water, forming the raffinate solvent, and transferred into the butyl acetate, the extract solvent. Due to the wetting properties of the polymeric tube, the butyl acetate forms the continuous phase, due to its nonpolar character, and water the disperse phase. Initially, the small specific acetone load of $\omega_{r,\mathcal{A}} = 0.04$ kg/kg is set in the raffinate solvent, corresponding to a initial concentration of $c_{r,\mathcal{A}}^0 = 0.0684$ mol/l. The initial load appears as reasonable ratio of a small initial concentration to the measurement error, as derived from test measurements. Since only the physical mass transfer is in the focus, the solute $\mathcal{B}$ is not present, i.e. $c_{e,\mathcal{B}}^0 = 0$ mol/l. The influence of Marangoni convection can be ignored, because of the small concentrations, cf. Wolf (1998).

The physical mass-transfer system is used in conjunction with the counter-flow arrangement of the slug generation unit, see figure 4.1a. A gas chromatograph, 7820A, Agilent Technologies, Switzerland, is used for the chemical analysis of the samples of the raffinate and the extract solvent. Each sample is evaluated three times to compensate the tolerances of the gas chromatograph and the evolution routine.

All flow and transport properties are obtained by a weighted average, whereas the weighting is based on the mass fractions and the respective properties of the mutual saturated solvents. For the raffinate solvent, the mean mass fraction of $\omega_{r,\mathcal{A}} = 0.03$ kg/kg is used, while the mean mass fraction of the extract solvent is $\omega_{e,\mathcal{A}} = 0.01$ kg/kg, cf. Misek and Berger (1985). Only the distribution coefficient is derived from own measurements. All fluid and transport properties are collected in table 4.1, as basis for subsequent studies. Binary diffusion coefficients are derived based on the modeling approach.

Three different total volumetric flow rates are used, while the ratio of both flow rates remains $\hat{V} = \dot{V}_d/\dot{V}_c = 1$. These total volumetric flow rates are $\dot{V}_{tot} = 2$ ml/min, $\dot{V}_{tot} = 4$ ml/min, and $\dot{V}_{tot} = 6$ ml/min. The reference flow rate is selected to be $\dot{V}_{ref} = 4$ ml/min. Based on the reference flow rate, the reactor length is derived to be $l_{re} = 600$mm and the minimal

Table 4.1: Physcial mass transfer: Flow and transport properties, derived from Misek and Berger (1985), besides the distribution coefficient, that is estimated by own batch experiments.

ϱ_c kg/m^3	ϱ_d kg/m^3	μ_d 10^{-3}kgm/s	μ_c 10^{-3}kgm/s	σ 10^{-3}kg/s^2	$\mathcal{D}_{r,\mathcal{A}}$ 10^{-9}m^2/s	$\mathcal{D}_{e,\mathcal{A}}$ 10^{-9}m^2/s	$m_{\mathcal{A}}$ -
994	881	1.13	0.732	11.5	0.998	2.20	0.997

length is given by $l_{min} = 100$ mm. In total, $S = 8$ different section lengths in the range 100 mm $\leq l_S \leq 600$ mm are used for the experimental investigation, namely $l_1 = l_{min} = 100$ mm, $l_2 = 150$ mm, $l_3 = 225$ mm, $l_4 = 300$ mm, $l_5 = 375$ mm, $l_6 = 450$ mm, $l_7 = 525$ mm and $l_{re} = 600$ mm.

The periodic element lengths are determined for each total volumetric flow rate based on the three different section lenghts $l_4 = 300$ mm, $l_5 = 375$ mm, and $l_6 = 450$ mm. At least 15 measurements of the periodic element length l_{pe} are averaged for each section and each volumetric flow rate, as summarized in figure 4.5, including the standard deviation error bars. The average length of the periodic elements $\bar{l}_{pe}$ decreases slightly with increasing volumetric flow rate, as reported by de Menech et al. (2008). The deviation is calculated to

$$\epsilon_{l_{pe,max}} = max \left| 1 - \frac{l_{pe}}{\bar{l}_{pe}} \right|, \tag{4.1}$$

and the average length appears as arithmetic average of the deviation for a volumetric flow rate. The reason for this behavior is directly derived from continuity, in particular shown by equation 1.9. As the average flow velocity increases, due to an increasing volumetric flow rate, the wall-film thickness and the velocity of the disperse phase increase. Accordingly, the volume fraction of the disperse phase ζ_d decreases as an constant volumetric flow rate is prescribed. The maximum spread of the measured periodic element lengths for each section length is $\epsilon_{l_{pe,max}} = 31\%$. The average deviation is $\bar{\epsilon}_{l_{pe}} = 15\%$. Indeed, these considerable deviations of the single and average periodic element lengths have been observed during the experiment for the counter-flow mixing junction, c.f figure 4.1a. The average periodic element length is $\bar{l}_{pe} \approx 4.80$ mm in all cases. The derived dimensionless parameters are summarized in tables 4.2 and 4.3, separated into dimensionless parameters that depend on the volumetric flow rate and constant dimensionless parameters. The dimensionless periodic-element length is calculated based on the averaged periodic element length for each volumetric flow rate. The modeling assumption $L_{pe}/Pe_{r,\mathcal{A}} \ll 1$ of the slug-flow approach is obviously fulfilled, compare chapter 2.

Table 4.2: Physical mass transfer: dimensionless flow and transport parameters, that depend on the volumetric flow rate.

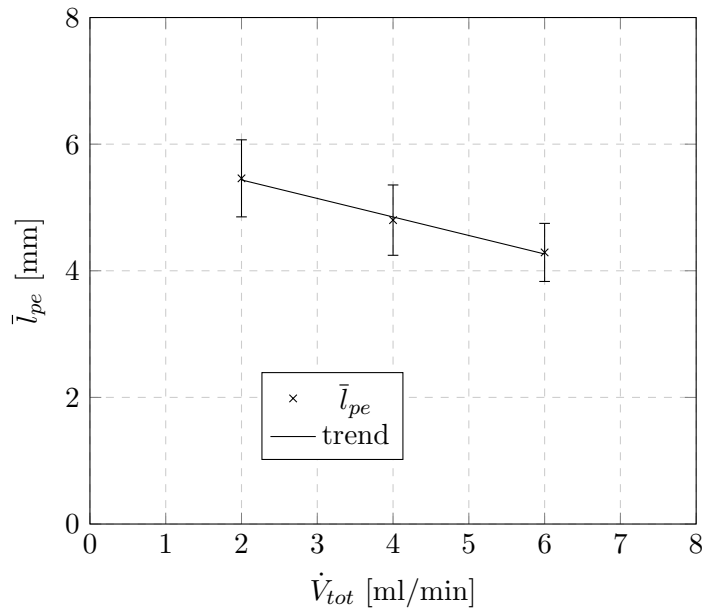| $\dot{V}_{tot}$ ml/min	Re_c 10^2	Ca_c 10^{-3}	$Pe_{r,\mathcal{A}}$ 10^4	L_{pe} -
2	0.511	2.70	42.5	5.46
4	1.02	5.39	85.0	4.80
6	1.53	8.89	1280	4.30

Figure 4.5: Physical mass-transfer system: measured average periodic element length $\bar{l}_{pe}$ as function of the investigated total volumetric flow rates $\dot{V}_{tot}$.

Table 4.3: Physical mass transfer: constant dimensionless flow and transport parameters, independent of the volumetric flow rate.

$\hat{\varrho}$	$\hat{\mu}$	$\hat{V}$	$\hat{\mathcal{D}}_{\mathcal{A}}$	$m_{\mathcal{A}}$
-	-	-	-	-
0.887	1.54	1.00	2.20	0.997

4.3.2   Reactive mass transfer

To study the reactive mass-transfer the test system consisting of kerosene (CAS:8008-20-6) and water (demineralized water) in conjunction with acetic acid (CAS:64-19-7) and sodium iodide (CAS:1310-73-2) as solutes $\mathcal{A}$ and $\mathcal{B}$ is chosen, since the test system has found application in related research efforts, see e.g. Burns and Ramshaw (2001), Harries et al. (2003), Kashid et al. (2007a), or Dessimoz et al. (2008). In relation to the experimental setup the nonpolar kerosene wets the channel walls and disperse aqueous slugs occur. Acetic acid is dissolved initially in kerosene, i.e. the raffinate solvent, and transferred into water, i.e. the extract solvent, where it reacts with sodium iodide. The solutes react in an equimolar ratio, cf. Mortimer et al. (2015) described by the elementary reaction equation

$$1\,\mathcal{A} + 1\,\mathcal{B} \rightarrow \text{Products.} \tag{4.2}$$

An initial mass fraction of acetic acid in the organic solvent of $\omega^0_{r,\mathcal{A}} = 0.04$ kg/kg is used, i.e. $c^0_{r,\mathcal{A}} = 0.550$ mol/l, while half number of molecules is initially present in the extract solvent, i.e. $c^0_{e,\mathcal{B}} = 0.275$ mol/l. The initial loads are chosen as compromise between the assumption of dilute concentrations and the measurement accuracy in conjunction with the physical mass-transfer system, compare section 4.3.1. The experiments are performed within the co-flow arrangement of the mixing junction, see figure 4.1b. The chemical analysis is performed by titration of the extract solvent, on basis of hydrochloric acid or sodium iodide, in conjunction with Phenolphthalein used as an optical indicator. Each sample is analyzed once only, due to the accurate

chemical analysis. The concentration of the raffinate solvent and the reactive consume are derived by a mass balance from the known concentration of the extract solvent. Mass fractions of $\omega_{r,\mathcal{A}}^0 = 0.02$ kg/kg and $\omega_{e,\mathcal{B}}^0 = 0.02$ kg/kg are used for the determination all flow, transport, and chemical parameters, summarized in tables 4.4 and 4.5. The fluid and transport properties are retrieved from the cited literature source or estimated by own measurements using the listed measurement tool for the mutual saturated solvents. The hydrogen and hydroxide ions are used for the modeling of the diffusion coefficients. The binary diffusion coefficient of the proton is estimated with the correlation of, cf. Wilke and Chang (1955) and average molar weight of kerosene of 170 g/mol, cf. Dagaut and Cathonnet (2006). Further, the interfacial tension is measured in chemical equilibrium. The measured interfacial tension, see table 4.4, is significantly lower than for the pure solvent system, given to $\sigma = 42 \cdot 10^{-3}$ kg/s^2 Kashid et al. (2007a). Additionally, the batch experiments for the evaluation of the distribution coefficient showed a high scatter. Accordingly, the value proposed by Kashid et al. (2010) is used as it is in good agreement with the batch experiments.

The measured interfacial tension is shown in figure 4.6 as function of the initial load in the

Table 4.4: Reactive mass transfer: Flow parameters, including sources or used measurement device.

ϱ_c kg/m^3	ϱ_d kg/m^3	μ_c 10^{-3}kgm/s	μ_d 10^{-3}kgm/s	σ 10^{-3}kg/s^2
792	998	2.19	1.00	25.3
Pyknometer: Brand (Duranglas 25cm^3)	(González et al., 2004)	(González et al., 2004)	Viscosimeter: Visco Tester VT 550	Tensiometer: Krüss K105T

Table 4.5: Reactive mass-transfer: Transport and chemical parameters, including sources or used measurement device.

$\mathcal{D}_{r,\mathcal{A}}$ 10^{-9} m^2/s	$\mathcal{D}_{e,\mathcal{A}}$ 10^{-9} m^2/s	$m_{\mathcal{A}}$ -	$\mathcal{D}_{e,\mathcal{B}}$ 10^{-9} m^2/s	ϑ 10^{11} l/ mol s
1.14	1.31	85	1.33	1.14
(Wilke and Chang, 1955)	(Wilke and Chang, 1955)	(Kashid, 2007), Batch experiments	(Samson, 2003)	(Kashid, 2007), (Zellner et al., 1977)

raffinate solvent, equal to the load in the extract solvent, including the estimated overall measurement error of 5% as error bars. The strong dependence to the interfacial tension is obvious as the interfacial tension decreases about 50% in the examined interval with, despite the low load. The influence of the solutes to the other flow parameters, i.e. the densities and the viscosities, and the diffusion coefficients is in contrast smaller than 10% in the examined range. The influence to the chemical parameters is even smaller. A volumetric reference flow rate of $\dot{V}_{ref} = \dot{V}_{tot} = 2$ ml/min is chosen. Additionally, the volumetric flow rates $\dot{V}_{tot} = 3$ ml/min and $\dot{V}_{tot} = 4$ ml/min are realized, all examined at the constant volumetric flow rate ratio of $\hat{V} = \dot{V}_d/\dot{V}_c = 1$. The reactor length is determined to $l_{re} = 1000$ mm, based on the reference total volumetric flow rate. The minimal length of $l_{min} = 50$ mm, measured from the needle tip to the separating steel sleeve is used and in total $S = 7$ sections are investigated, namely $l_1 = l_{min} = 50$ mm, $l_2 = 100$ mm, $l_3 = 200$ mm, $l_4 = 300$ mm, $l_5 = 500$ mm, $l_6 = 700$ mm, and $l_7 = l_{re} = 1000$ mm.

The periodic-element lengths are measured for each total volumetric flow rate considering three different reactor length, namely $l_2 = 500$ mm, $l_3 = 300$ mm, and $l_4 = 200$ mm. At least 15
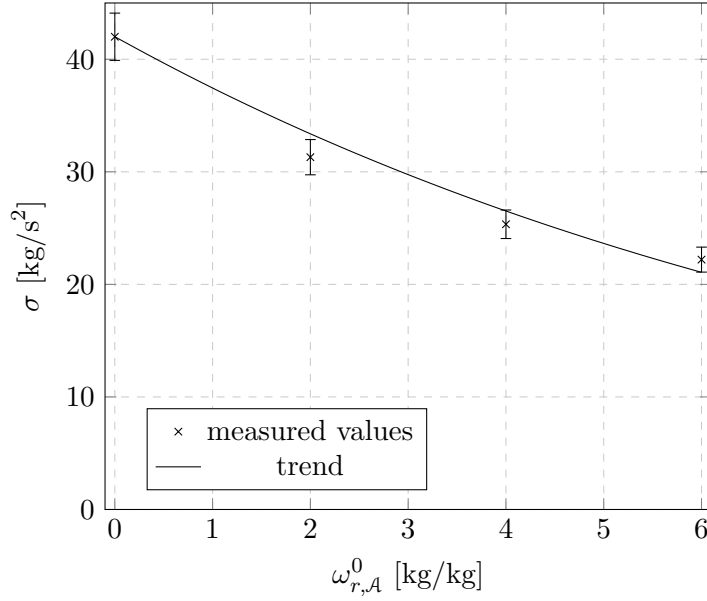
Figure 4.6: Reactive mass transfer: measured interfacial tension σ as function of the initial load $\omega_{r,\mathcal{A}}^0$.

measurements are averaged at each reactor length and each volume flow rate. The lengths of the periodic elements $\bar{l}_{pe}$ are shown in figure 4.7 as function of the total volumetric flow rate. The periodic-element length decreases with increase of the volumetric flow rate, as reported by de Menech et al. (2008). The increase of the velocity difference, due to the increase of average channel velocity can be found as reason, described by equation 1.9. The maximum spread of a measured periodic-element length to the averaged value appears to be $\epsilon_{l_{pe},max} = 14\%$, while an average deviation of $\bar{\epsilon}_{l_{pe}} = 3.4\%$ is present. An average periodic-element length of $\bar{l}_{pe} \approx 2.8$ mm is determined. These small deviations compared to the physical mass-transfer system, see section 4.3.1, indicate a stable generation of the flow pattern.
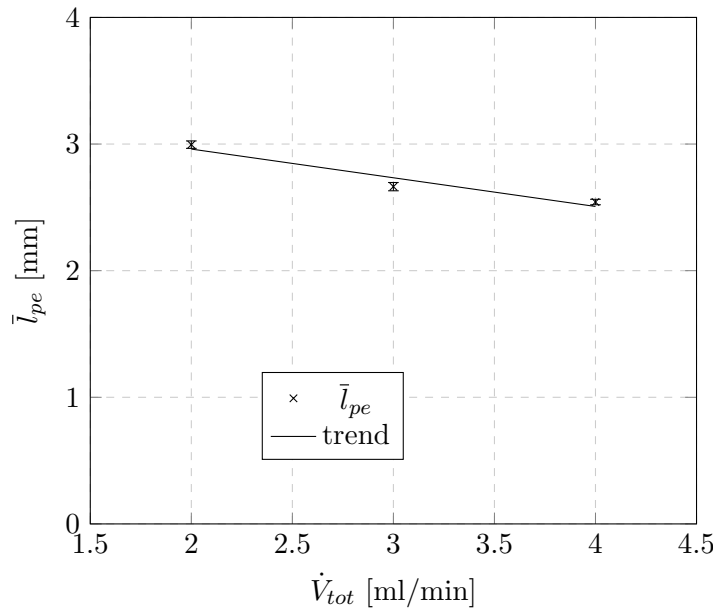

Figure 4.7: Reactive mass transfer: measured average periodic-element length $\bar{l}_{pe}$ for the investigated total volumetric flow rates $\dot{V}_{tot}$.

The derived dimensionless parameters are summarized in tables 4.6 and 4.7 separated into flow rate dependent and constant parameters. The dependency of the excess factor ψ on the volumetric flow rate appears to be weak and the excess factor is therefore treated as constant. The magnitude of the Hatta number indicates a very fast or rather instantaneous chemical reaction and a desired mass-transfer limited transfer process. The dimensionless periodic element length is calculated based on the averaged periodic element length for each volumetric flow rate. The modeling assumption $L_{pe}/Pe_{r,\mathcal{A}} \ll 1$ is fulfilled.

Table 4.6: Reactive mass transfer: dimensionless parameters depending on the volumetric flow rate.

$\dot{V}_{tot}$ ml/min	Re_c -	Ca_c 10^{-3}	$Pe_{r,\mathcal{A}}$ 10^4	L_{pe} –
2	15.4	3.67	3.74	2.96
3	23.0	5.50	5.61	2.66
4	30.7	7.33	7.48	2.54

Table 4.7: Reactive mass transfer: constant dimensionless parameters.

$\hat{\varrho}$ –	$\hat{\mu}$ –	$\hat{V}$ –	$\hat{D}_{\mathcal{A}}$ –	$m_{\mathcal{A}}$ –	$Ha_{e,\mathcal{A}}$ 10^4	λ –	ψ –
1.13	0.475	1	1.15	85	2.74	1.02	1.77

4.4   Evaluation and comparison

The results of the experiments are presented and discussed in the following. The evolution of the dimensionless volumetric mass-transfer coefficient Si, i.e. the product of the Sherwood number Sh and the dimensionless interfacial area α, is examined as a function of the extraction rate $F_{\mathcal{A}}$. Further, the simulation model is adapted to the corresponding conditions in the experiments and the simulation results are compared to the experimental findings.

4.4.1   Physical mass transfer

The comparison of the dimensionless volumetric mass-transfer coefficient Si as a function of the extraction rate $F_{\mathcal{A}}$, obtained from both, the experiment and the simulation, is shown is shown in figure 4.8 for the reference volumetric flow rate of $\dot{V}_{ref} = 4\text{ml/min}$. The experimental dimensionless volumetric mass-transfer coefficient (exp) over-predicts the volumetric mass-transfer coefficients of the simulation (sim) significantly. The discrepancy between the experimental findings and the simulation results are not really surprising. In the experiment, the two liquids form an interface in the generation unit, cf. figure 4.1a, and hence, a substantial mass transfer can occur during the formation of the slugs, long before the slug-flow pattern is developed, cf. Zhao et al. (2007) or Fries et al. (2008). In contrary, the simulation is valid for the developed slug-flow pattern only. This is clearly indicated by the remaining offset between the experimentally and stimulative obtained volumetric mass-transfer coefficients for large extraction rates, i.e. at the end of the transfer process, see figure 4.8. Hence, strictly spoken, the initial concentration for the simulation cannot simply be taken from the inflow in both branches of the generation unit. Instead, the initial concentrations should be taken from the developed slug close to the
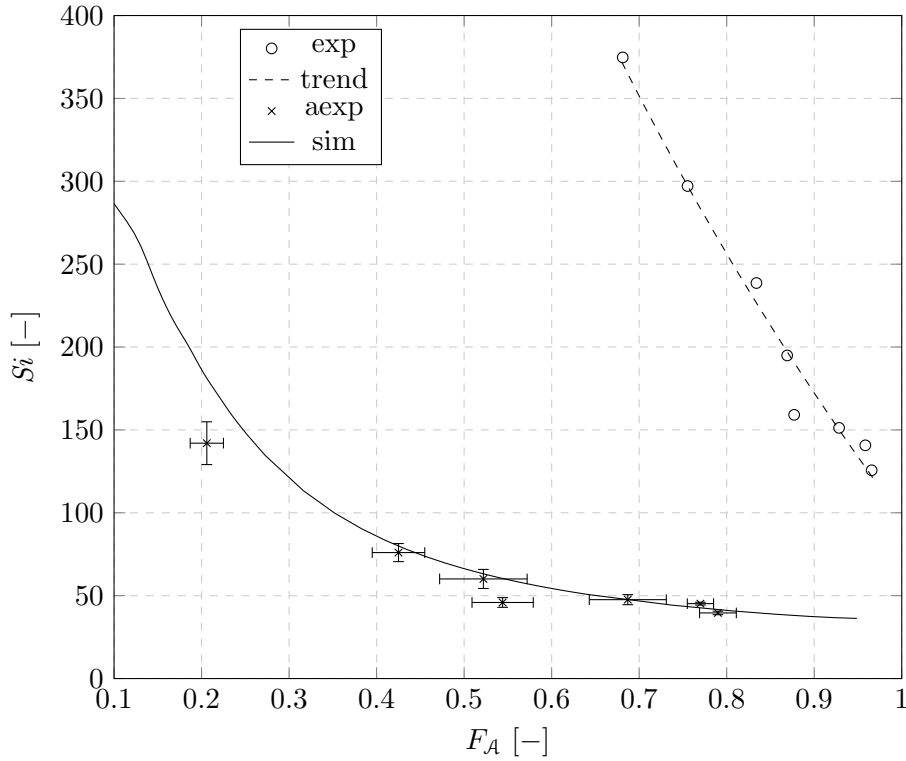
Figure 4.8: Physical mass-transfer, comparison of experimental (exp,trend), adapted experimental (axep), and simulation (sim) data: dimensionless volumetric mass-transfer coefficient Si as function of the extraction rate $F_{\mathcal{A}}$ for the reference flow rate $\dot{V}_{tot} = \dot{V}_{ref} = 4$ ml/min.

generation unit.

Formally, this problem can be solved by an adaption of the frame of reference, as illustrated in figure 4.9. The generation unit is excluded from the frame of reference and instead an average concentration, found for the shortest reactor section $\bar{c}_{r,\mathcal{A}}(l_{min}) = c_{r,\mathcal{A}}^{0,aexp}$, and the corresponding contact-time $\tau_m(l_{min})$, are used as initial state for the evaluation of the experiments. This adapted evaluation of the experimental data now leads to experimentally adapted volumetric mass-transfer coefficients (aexp) which are in good agreement with the simulation results, as obvious in figure 4.8. The same procedure is also used for the evaluation of the other two volumetric flow rates in the experiment, see figure 4.10a and figure 4.10b. Once more, the very good agreement is obtained for the adapted experimental (aexp) and the simulation (sim) results. The adapted experimental and the simulation data converge against the same dimensionless volumetric mass-transfer coefficient at the end of the transient process, i.e. large extraction rates. In other words, the mass that is transferred along the shortest section length l_{min} is a good approximation to describe the influence of the generation unit to the overall transfer process. The counter-flow arrangement of the generation unit obviously leads to a considerable mass transfer during the generation of the flow pattern. The overall influence can be described by the relative concentration difference to $\Delta C_{r,\mathcal{A}}(l_{min}) = \left(c_{r,\mathcal{A}}^0 - \bar{c}_{r,\mathcal{A}}(l_{min})\right)/c_{r,\mathcal{A}}^0 = 17\%$. This estimation holds for all investigated volumetric flow rates in good approximation. The remaining deviations between the experimental points and the simulation data are caused by the unstable generation of the slug-flow pattern in the counter-flow arrangement of the generation unit, compare section 4.3.1, in combination with the adaption of the frame of reference, see figure 4.1a. The influence of the measurement error increases as a result of the adaption of the frame of reference. The relative standard deviation for the shortest section length l_{min}, i.e. the lowest
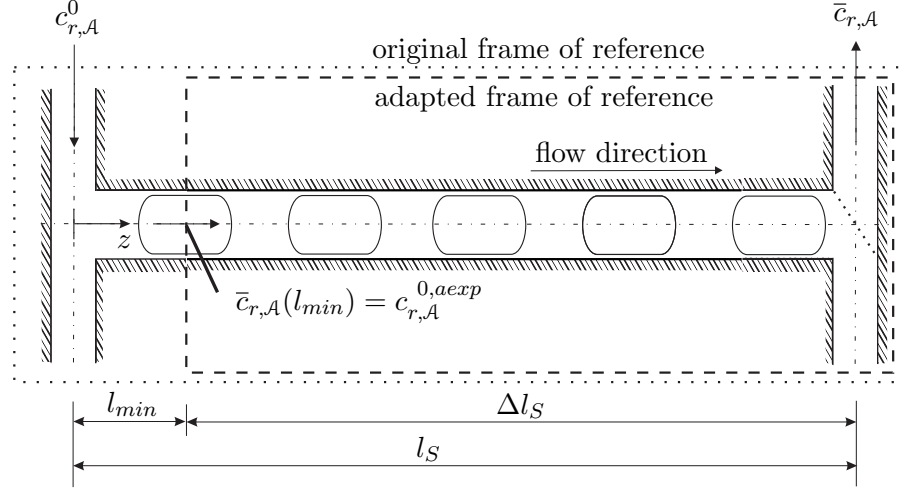
Figure 4.9: Physical mass transfer: Adaption of the frame of reference for the evaluation of the experimental data, excluding the influence of the mixing junction.
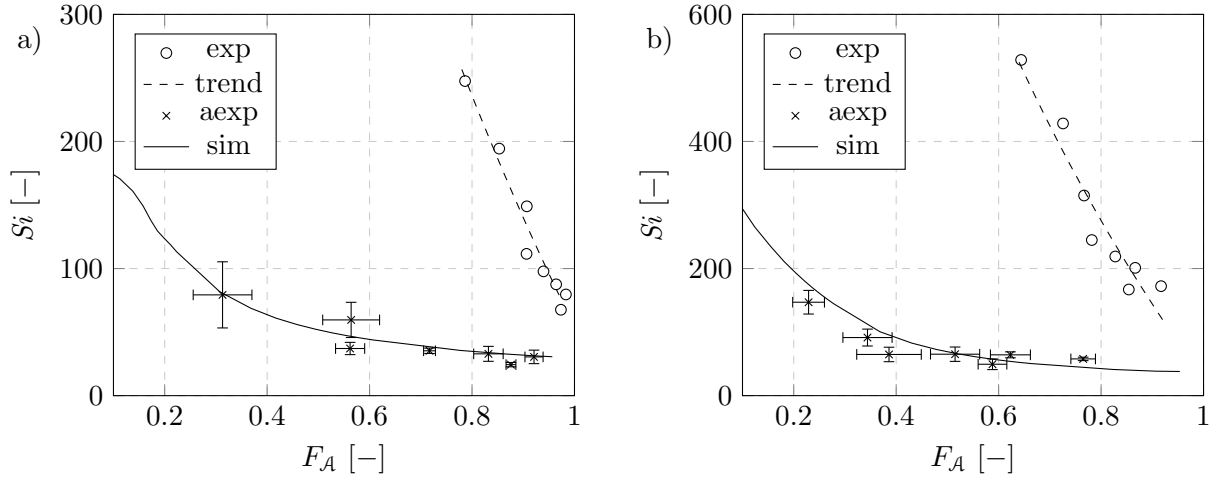

Figure 4.10: Physical mass transfer, comparison of experimental (exp,trend), adapted experimental (aexp) and simulation (sim) data: dimensionless volumetric mass-transfer coefficient Si as a function of the extraction rate $F_{\mathcal{A}}$: a) $\dot{V}_{tot} = 2$ ml/min; b) $\dot{V}_{tot} = 6$ ml/min.

extraction rate, for the volumetric reference flow rate in the original frame of reference appears to 1.5% of the measured average value. The relative standard deviation increases to 10% of the adapted experimental data, as the relative influence of the measurement error increases due to the decrease of the average concentration in the adapted frame of reference.

The highest deviation of the adapted experimental values to the simulation is given for the lowest extraction rate for the volumetric reference flow rate, appearing to

$$\epsilon_{Si,max} = max \left| 1 - \frac{Si(aexp)}{Si(sim)} \right| = 46\%, \tag{4.3}$$

while a average deviation of $\bar{\epsilon}_{Si} = 7\%$ is present for all values. The volumetric mass-transfer coefficients, evaluated for $F_{\mathcal{A}} = 0.95$, are presented in table 4.8. The magnitudes are in the expected range. In summary, the volumetric mass-transfer coefficients from the experiments and the simulation model are in very good and reasonable agreement for the current investigation.

Table 4.8: Physical mass transfer: Dimensioned and dimensionless volumetric mass-transfer coefficients at the end of the transfer process, i.e. $F_A = 0.95$, for the examined total volumetric flow rates $\dot{V}_{tot}$.

$\dot{V}_{tot}$ ml/min	$ka(F_A = 0.95)$ 10^{-3}/s	$Si(F_A = 0.95)$ $-$
2	30.6	30.6
4	36.3	36.3
6	38.0	38.0

4.4.2 Reactive mass transfer

The dimensionless volumetric mass-transfer coefficient Si as function of the extraction rate for reactive mass transfer is shown in figure 4.11. The comparison offers a good agreement of numerical and experimental data. Hence, the use of the co-flow arrangement of the mixing junction, see figure 4.1, shows only a weak or rather negligible influence on the generation process. An adaption of the frame of reference is not necessary, so that one more measured data point can be presented. This can be seen in the diagram, where the experimental (exp) and simulation (sim) data converge towards the same limiting value for large extraction rates in good approximation. The results for the other two volumetric flow rates show a similar behavior,
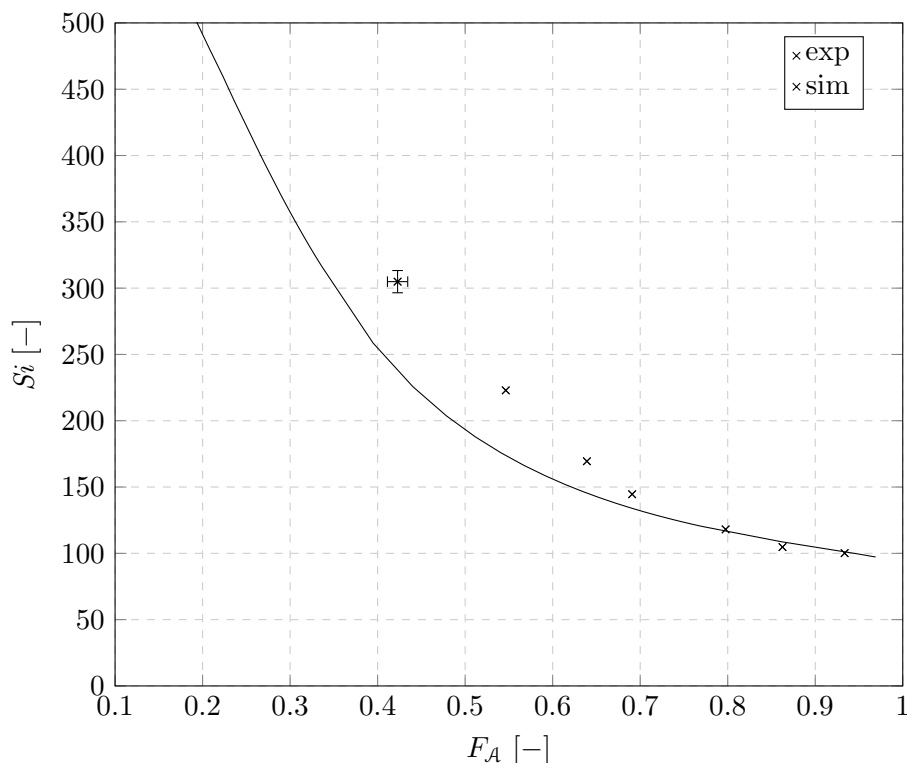
Figure 4.11: Reactive mass-transfer, comparison of experimental (exp) and simulation (sim) data: Dimensionless volumetric mass-transfer coefficient Si as function of the extraction rate F_A for the reference flow rate $\dot{V}_{tot} = 2$ ml/min.

shown in figures 4.12a and figure 4.12b. The co-flow arrangement of the generation unit results in a stable and reproducible process, indicated by the small scatter and standard deviations of the experimental data points and the low deviations of the periodic-element lengths, compare section 4.3.2.

The largest deviation of the experimental values to the simulated data is $\epsilon_{Si,max} = 25\%$ for the smallest section l_{min}, i.e. the lowest extraction rate, in combination and the reference flow rate, while an average deviation of $\bar{\epsilon}_{Si} = 5\%$ is present for all values. The deviations are evaluated analogous to $\epsilon_{l_{pe,max}}$, compare equation 4.3. The error bars are only plotted exemplary for the dimensionless volumetric mass-transfer coefficient, obtained for the lowest extraction rate, in conjunction with the volumetric reference flow rate. The low magnitude of the error results from the use of the co-flow arrangement without adaption of the frame of reference. The other error bars, not shown in the diagrams, offer an even smaller measurement error.

The larger deviations for the short sections, rather low extraction rates, may be caused by the change of the flow parameters during the transfer process and the related influence of Marangoni effects, that are not covered by the model. A noticeable dependence of the interfacial tension to the concentration is recognized during the measurement of the fluid properties, supporting this idea, compare section 4.3.2. This train of thoughts is confirmed as the deviations for low extraction rates decrease with increasing volumetric flow rate, i.e. convection. The volumetric
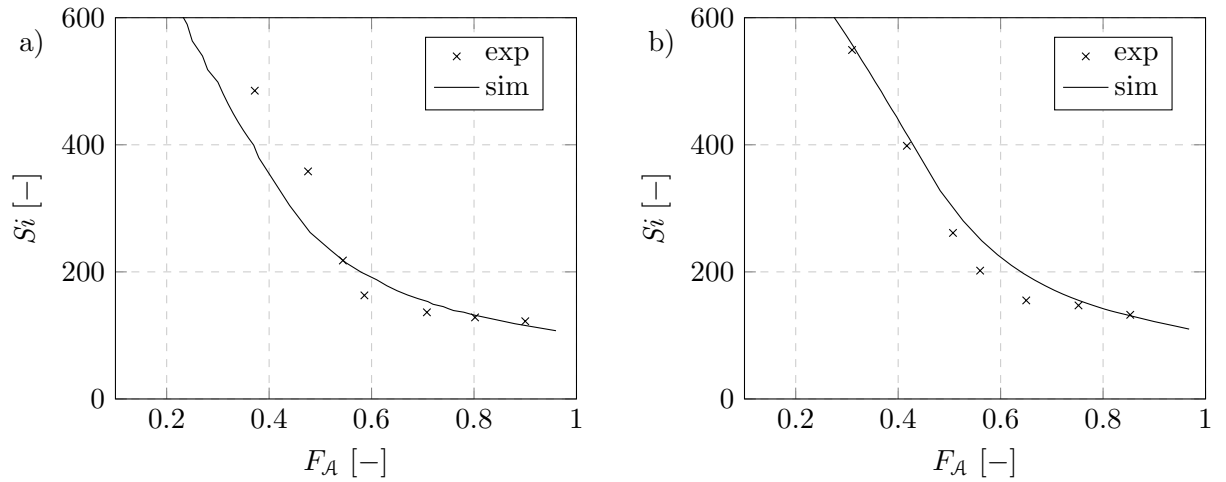
Figure 4.12: Comparison of experimental and numerical data for reactive mass transfer: Dimensionless volumetric mass-transfer coefficient Si as a function of the extraction rate $F_{\mathcal{A}}$: a) $\dot{V}_{tot} = 3\,\mathrm{ml/min}$; b) $\dot{V}_{tot} = 4\,\mathrm{ml/min}$.

mass-transfer coefficients for $F_{\mathcal{A}} = 0.95$ based on the simulation data are presented in table 4.9. The magnitudes are again in the expected range. In summary, a reasonable agreement of the mass-transfer model and the experimental obtained values is achieved. The remaining deviations may especially be caused by the influence of Marangoni stresses, during the transfer process.

Table 4.9: Reactive mass tranfer: Dimensional and dimensionless volumetric mass-transfer coefficients at the end of the transfer process ($F_{\mathcal{A}} = 0.95$) for various total volumetric flow rates $\dot{V}_{tot}$, derived from the simulation results.

| $\dot{V}_{tot}$ | ka | Si |
ml/min	$10^{-3}/\mathrm{s}$	$-$
2	114	97.2
3	145	107
4	161	110

5

Results

The integral and local mass transfer and the influence of the parameters is examined in this chapter based on the chosen experimental test systems, see chapter 4. First, the spatial distribution of the mass transfer at the free interface is investigated in detail, a parameter study is performed and a conclusion is given.

5.1 Spatial distribution of the volumetric mass-transfer coefficient

The volumetric mass-transfer coefficient and its spatial distribution are investigated in detail using the experimentally validated reference cases, compare chapter 4, of the physical and the reactive mass-transfer test systems. The spatial distribution is evaluated for a mean extraction rate of $F_{\mathcal{A}} = 0.38$ for each system.

5.1.1 Physical mass transfer

Exemplary the reference flow rate of $\dot{V}_{tot} = 4$ ml/min is used for the investigation of the temporal evolution and the spatial distribution of the volumetric mass-transfer coefficient of the physical mass-transfer system. The following dimensionless parameters $Re_c = 102$, $\hat{\varrho} = 0.887$, $Ca_c = 5.39 \cdot 10^{-3}$, $\hat{\mu} = 1.54$, $\hat{V} = 1$, $L_{pe} = 4.80$, $Pe_{r,\mathcal{A}} = 85.0 \cdot 10^4$, $\hat{D}_{\mathcal{A}} = 2.20$, and $m_{\mathcal{A}} = 0.997$ characterize the problem. The disperse phase is the raffinate solvent and no chemical reaction is present, i.e. $C^0_{e,\mathcal{B}} = 0$. In figure 5.1 the evolution of the dimensionless volumetric mass-transfer coefficient Si, appearing as product of the Sherwood number Sh and the dimensionless specific area of the free interface α, obtained from the adapted experiments $Si(aexp)$ and the simulation Si are plotted as function of the extraction rate $F_{\mathcal{A}}$. The evolution of the simulation is further split into its local portions Si^{WF}, Si^{F}, and Si^{B} of the wall film (WF), the front cap (F), and the back cap (B). The volumetric mass-transfer coefficient and its portions converge all towards a limiting value with increasing extraction rate as expected, cf. Clift et al. (1978). The portions of the dimensionless volumetric mass-transfer coefficient $Si^{F} = 2.26$, $Si^{WF} = 32.7$ and $Si^{B} = 1.11$ sum up to a transfer rate of $Si = 36.07$ at the end of the transient process, i.e. $F_{\mathcal{A}} = 0.95$. The wall-film portion has the largest contribution to the dimensionless volumetric mass-transfer coefficient, namely $Si^{WF}/Si = 91\%$, almost constant throughout the whole process. The contribution of the front and the back cap appears rather small, i.e. $(Si^{F} + Si^{B})/Si = 9\%$. This is true even at the beginning of the transfer process, when the largest concentration difference should allow for effective mass transfer.
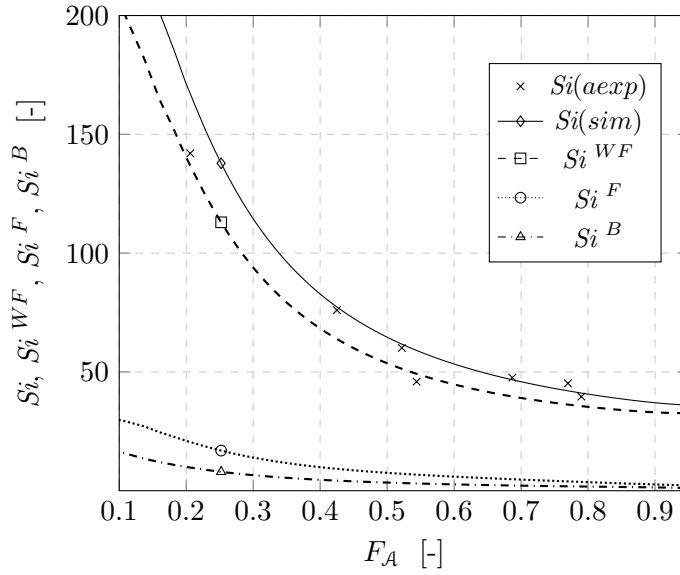
Figure 5.1: Physical mass transfer, reference case: dimensionless volumetric mass-transfer coefficient of experiment $Si(aexp)$ and simulation $Si(sim)$ and local portions Si^F, Si^{WF}, and Si^B as a function of the extraction rate $F_{\mathcal{A}}$.

The detailed analysis of the conditions at the free interface and inside the solvents gives insight into this behavior, evaluated for the mean extraction rate of $F_{\mathcal{A}} = 0.38$. The dimensionless interfacial velocity $\left|V^{IF}\right|$, the stream lines and the local dimensionless volumetric mass-transfer coefficient $dSi(Z)$, normalized with its maximum value $(dSi)_{max}$, are plotted as function of the dimensionless coordinate Z, see figure 5.2. The wall-film portion represents the largest portion of the interfacial area, with $\alpha^{WF}/\alpha = 81\%$, while the caps occupy $(\alpha^B + \alpha^F)/\alpha = 19\%$ of the area of the free interface, based on a specific interfacial area of $\alpha = 4.69$ in dimensionless formulation. The transport is dominated by convection, i.e. $Pe_{r,\mathcal{A}} \gg 1$, resulting in a transport along the stream lines and an inhomogeneous concentration field. The magnitude of the local convection is captured by the tangential interface velocity in figure 5.2. Mass is transported from the bulk to the free interface at the front saddle point (SF), due to the direction of the vortices. Here, the flow of the continuous phase also enters the wall film. Hence, the largest local transfer rates appear close to the saddle point at the front, as the flow compresses the concentration boundary layer and causes larger gradients. The driving concentration gradient decreases along the interface to a minimum at the back saddle point (SB), where the flow is directed into the bulk of the disperse phase. Another local maximum of the volumetric mass-transfer coefficient occurs at the constriction of the wall film, near the maximum of the tangential interface velocity. The local concentration differences between the vortices inside the disperse phase appear to be much smaller, than across the interface, as is obvious from the concentration field. Accordingly, mass is transported pre-dominantly from the bulk in the main vortex to the free interface and much less into the vortices in the front and in the back. The transfer rates at the front and the back portions of the free interface are consequently much smaller. No mass is transferred at the stagnant points in the front and in the back, lying on the symmetry line.

In figure 5.3 the evolution of the relative mean wall-film concentration Γ, appearing mean as ratio of the average concentration of solute $\mathcal{A}$ in the wall film to the average concentration inside the solvent assigned to the continuous phase, is shown. The relative wall-film concentration rises quickly to a maximum of $\Gamma \approx 3$ and decreases during the transfer process to a limiting value of $\Gamma = 1.27$ for $F_{\mathcal{A}} = 0.95$. Hence, the mean concentration inside the wall film is about 27%
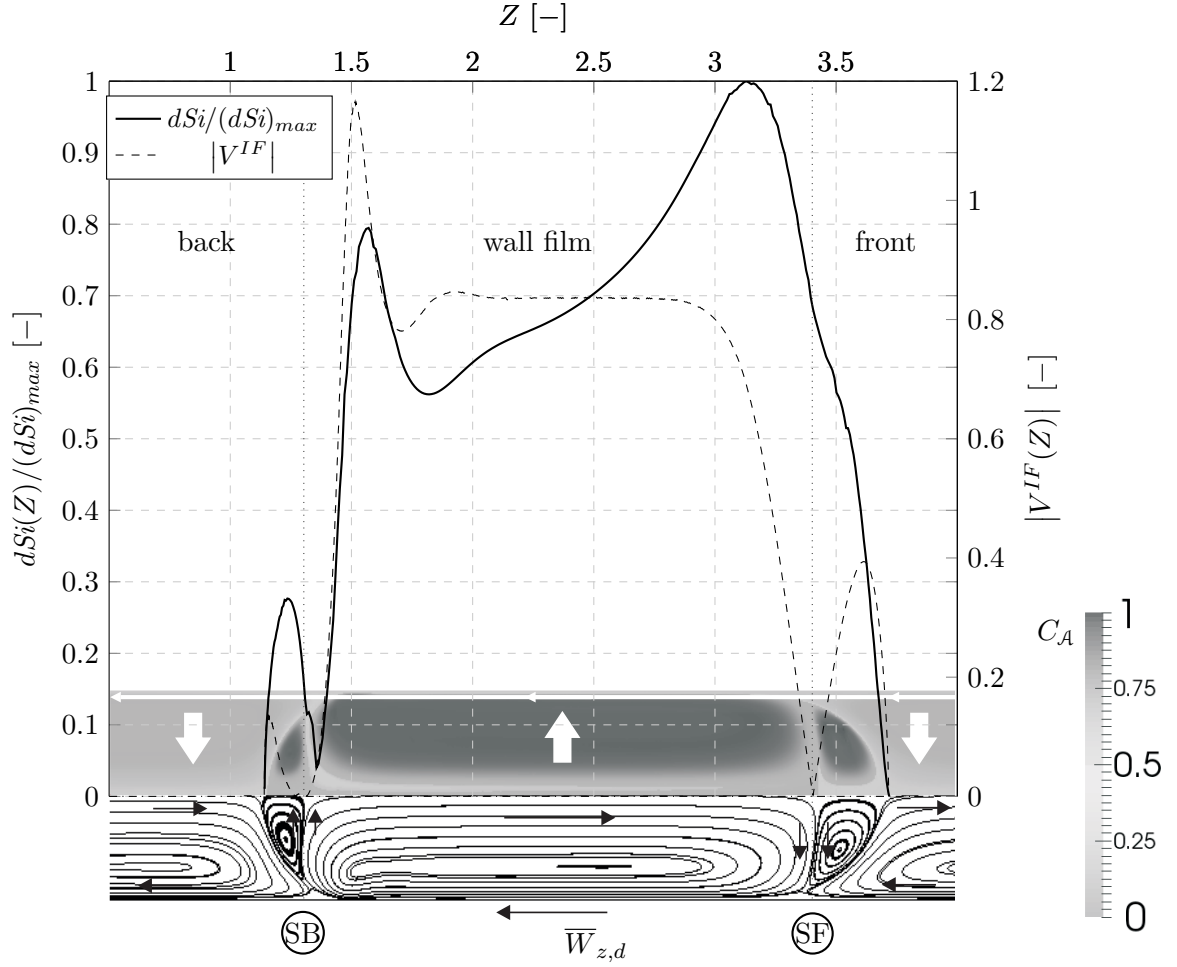
Figure 5.2: Physical mass transfer, reference case: distribution of the dimensionless local volumetric mass-transfer coefficient dSi, normalized to is maximum $(dSi)_{max}$ as function of the dimensionless coordinate Z. Additionally, the concentration field, the stream lines and the dimensionless tangential velocity $|V^{IF}|$ are given.

higher than the average concentration inside the extract solvent, i.e. continuous phase, during the transient process. This is caused by the large amount of mass transferred through the wall film. The concentration distribution along the extended wall film, compare section 1.3.2,

$$\gamma(Z) = \frac{1}{\mathbf{A}^{EWF}(Z)} \int_{A^{EWF}(Z)} C_{sc,\mathcal{A}}^{EWF}(H,Z)d\mathbf{A}, \tag{5.1}$$

for $F_{\mathcal{A}} = 0.38$ confirms this behavior. The local concentration $C^{EWF}(H,Z)$ is averaged for each cross-section inside the extended wall film $\mathbf{A}^{EWF}$, see figure 5.4, and gives further insight into the transport process. The concentration of a fluid element increases in the axial direction along the wall film. Mass transferred near the front saddle point (SF) into the wall film decreases the local concentration difference downstream due to accumulation. After leaving the wall film, mass is transferred into the bulk of the extract solvent and the fluid element re-enters the wall film with decreased concentration. The relative axial flow in the wall film intensifies the transport between the bulks of the solvents as mass is transferred into the wall film and further into the bulk of the continuous phase, as sketched in figure 5.4. This result is in close relation to the findings from literature, cf. section 1.3.2. The wall-film Péclet number appears to be $Pe^{WF} = 67.5$, based on $\overline{H} = 0.0230$ and $\overline{\Delta W}_Z = 0.0760$.
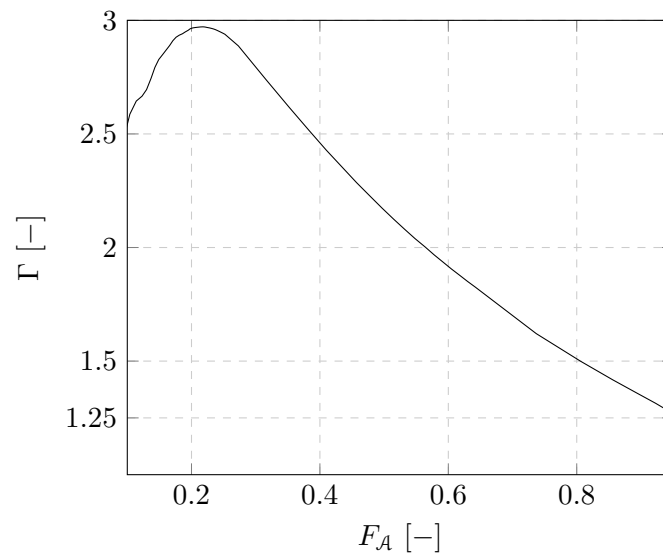
Figure 5.3: Physical mass transfer, reference case: Relative wall-film concentration Γ, ratio of the average wall-film concentration to the average concentration in the continuous phase, as function of the extraction rate $F_{\mathcal{A}}$.

Figure 5.4: Physical mass transfer, reference case: Concentration distribution along the extended wall film $\gamma(Z)$ as a function of the dimensionless coordinate Z. Additionally, the concentration field and the stream lines are shown.

5.1.2   Reactive mass transfer

The volumetric reference flow rate of $\dot{V}_{tot} = 2$ ml/min is used for the detailed investigation, corresponding to the following dimensionless parameters: $Re_c = 15.4$, $\hat{\varrho} = 1.26$, $Ca_c = 3.66 \cdot 10^{-3}$, $\hat{\mu} = 0.457$, $\hat{V} = 1.00$, $L_{pe} = 2.96$, $Pe_{r,\mathcal{A}} = 3.74 \cdot 10^4$, $\hat{D}_{\mathcal{A}} = 1.15$, $m_{\mathcal{A}} = 85$, $Ha_{e,\mathcal{A}} = 2.74 \cdot 10^4$, $\lambda = 1.02$, and $\psi = 1.77$. Here, the continuous phase is the raffinate solute. A chemical reaction is present, i.e. $C_{e,\mathcal{B}}^0 > 0$. In figure 5.5 the evolution of the dimensionless volumetric mass-transfer
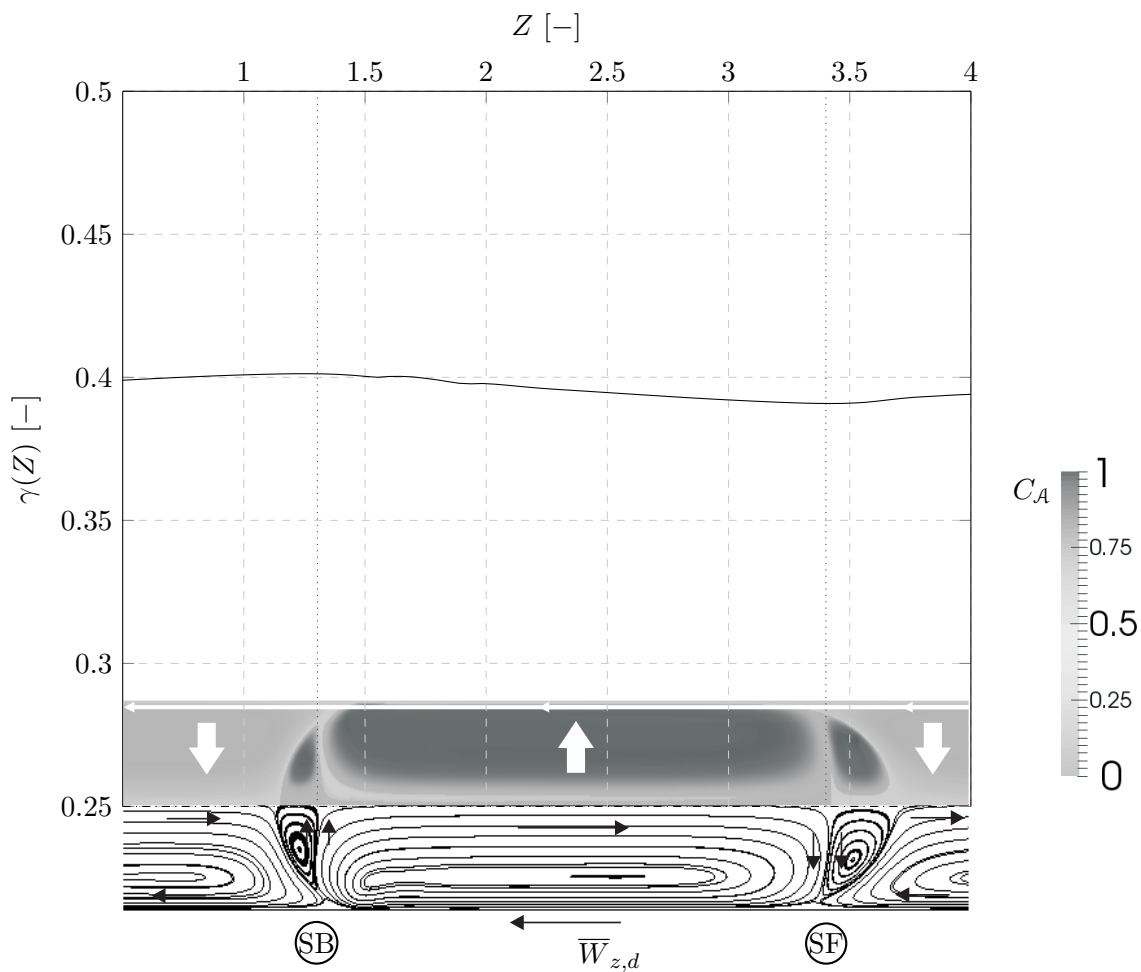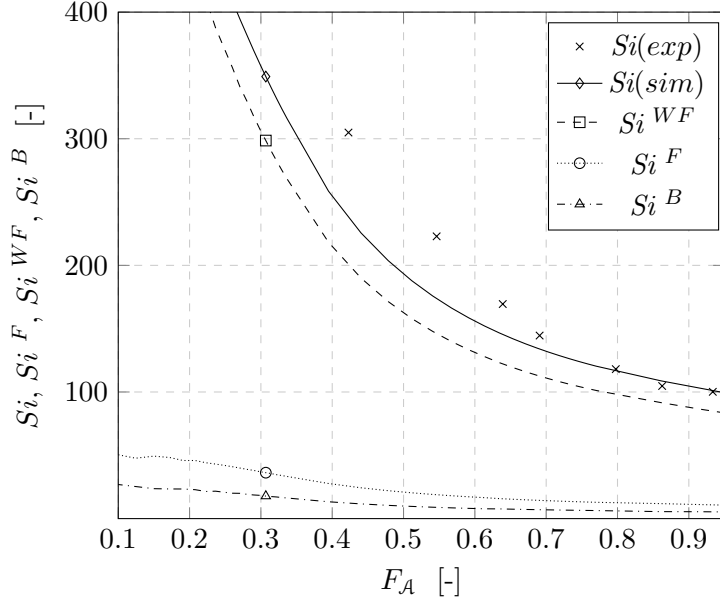

Figure 5.5: Reactive mass transfer, reference case: Dimensionless volumetric mass-transfer coefficient Si and local portions Si^F, Si^{WF} and Si^B as function of the extraction rate $F_{\mathcal{A}}$.

coefficient Si, being the product of the Sherwood number Sh and the specific interfacial area α in dimensionless form, obtained from the experiments and the simulation are plotted as function of the extraction rate $F_{\mathcal{A}}$. The evolution of the simulation is split into its local portions Si^{WF}, Si^F, and Si^B of the wall film (WF), the front cap (F), and the back cap (B). The transfer rate and its portions converge towards a limiting value as expected, cf. Clift et al. (1978). The portions of the dimensionless volumetric mass-transfer coefficient $Si^{WF} = 83.6$, $Si^F = 10.6$, and $Si^B = 5.40$ sum up to a dimensionless volumetric mass-transfer coefficient of $Si = 99.6$, for $F_{\mathcal{A}} = 0.95$. The wall-film portion dominates and is responsible for $Si^{WF}/Si = 84\%$ of the volumetric mass-transfer coefficient, while the contributions of the caps are much smaller, i.e. $(Si^F + Si^B)/Si = 16\%$. In figure 5.6 the dimensionless concentration fields, the stream lines, and the local dimensionless volumetric mass-transfer coefficient $dSi(Z)$, normalized to its local maximum $(dSi)_{max}$ for $F_{\mathcal{A}} = 0.38$ are shown as functions of the coordinate Z. The wall film occupies the largest portion of the interface with $\alpha^{WF}/\alpha = 66\%$, while the caps occupy $(\alpha^F + \alpha^B)/\alpha = 34\%$ based on a specific interfacial area of $\alpha = 4.96$ in dimensionless form. The local dimensionless volumetric mass-transfer coefficient shows a similar behavior as for the physical mass transfer and a detailed discussion does not appear necessary, compare section 5.1.1.

The evolution of the relative wall-film concentration Γ, appearing as mean ratio of the average concentration in the wall film to the average concentration in the continuous phase, as a function of the extraction rate $F_{\mathcal{A}}$, see figure 5.7. The relative wall-film concentration is always $\Gamma < 1$, since the continuous phase is the raffinate solvent, and converges towards a limiting value of
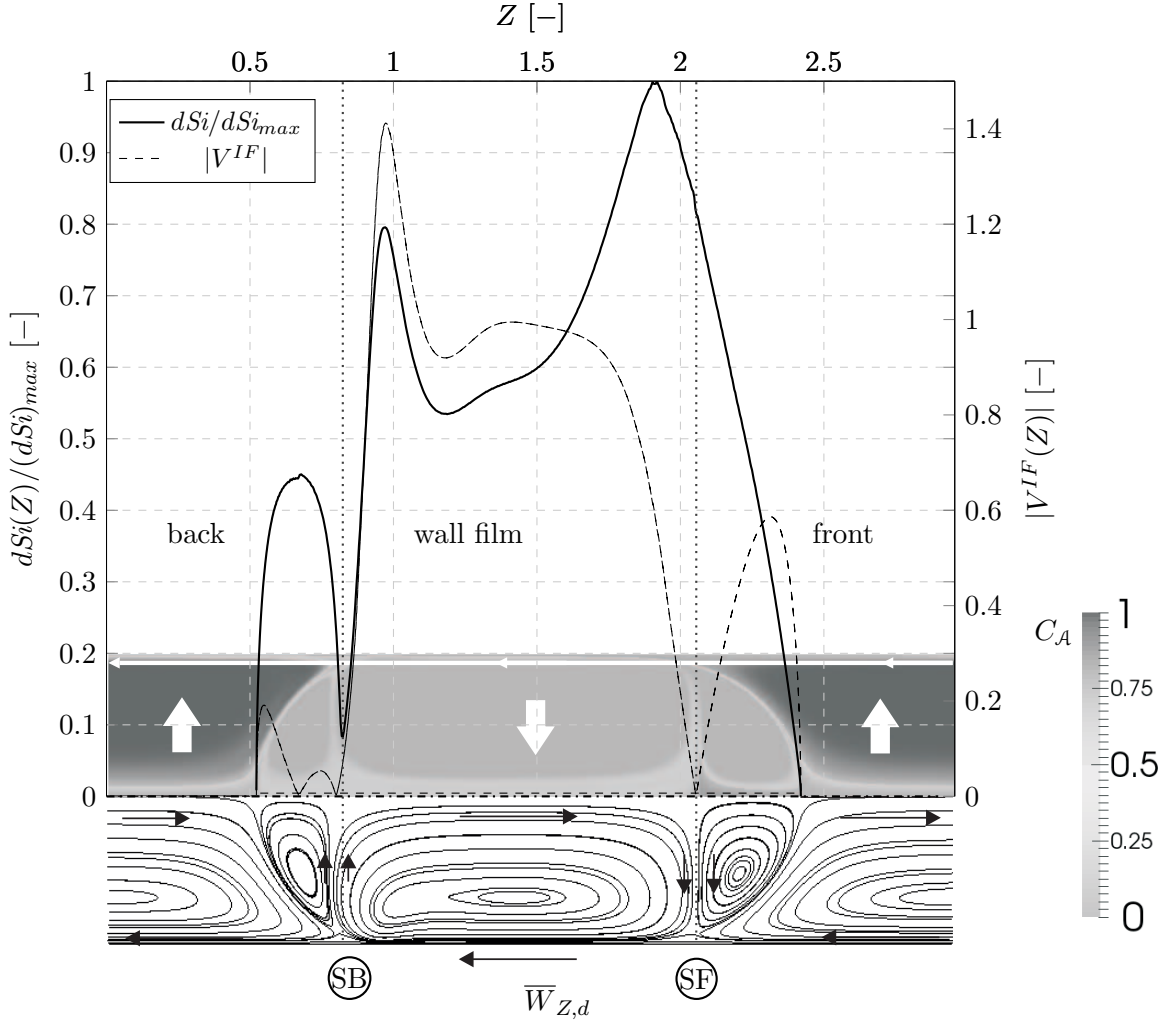
Figure 5.6: Reactive mass transfer, reference case: distribution of the dimensionless local volumetric mass-transfer coefficient dSi, normalized to is maximum $(dSi)_{max}$ as function of coordinate Z. Additionally, the concentration field, the stream lines and the dimensionless interfacial velocity $\left|V^{IF}\right|$ are shown.

$\Gamma = 0.170$ for $F_{\mathcal{A}} = 0.95$. The mean concentration inside the wall film is about 83% lower than the average concentration inside the continuous phase, i.e. here the raffinate solvent, during the transient process. The concentration distribution along the extended wall film $\gamma(Z)$, see 5.8, shows again that the velocity difference $\overline{\Delta W}_z$ in the wall film intensifies the transport between the bulks of the solvents. This explains the large wall-film portion of the dimensionless volumetric mass-transfer coefficient, compare section 5.1.1. The wall-film Péclet number is $Pe_{r,\mathcal{A}} = 40.6$, based on the dimensionless average wall-film height $\overline{H} = 0.0180$ and dimensionless velocity difference $\overline{\Delta W}_Z = 0.0600$.
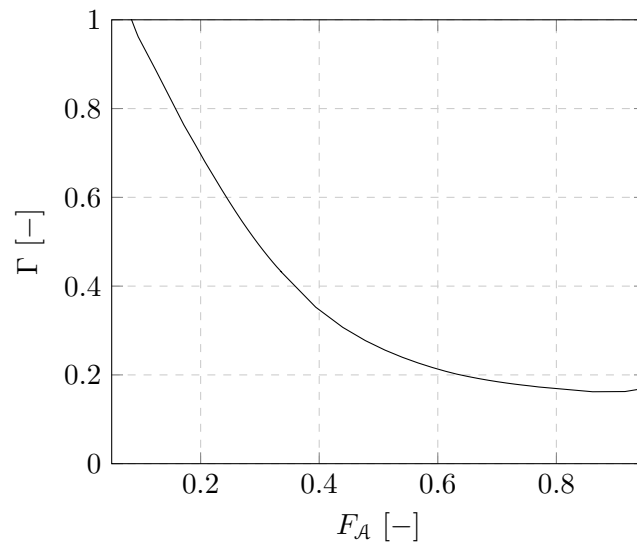
Figure 5.7: Reactive mass transfer, reference case: Relative wall-film concentration Γ, appearing as mean ratio of the average concentration in the wall film to the average concentration in the continuous phase, as function of the extraction rate F_A.
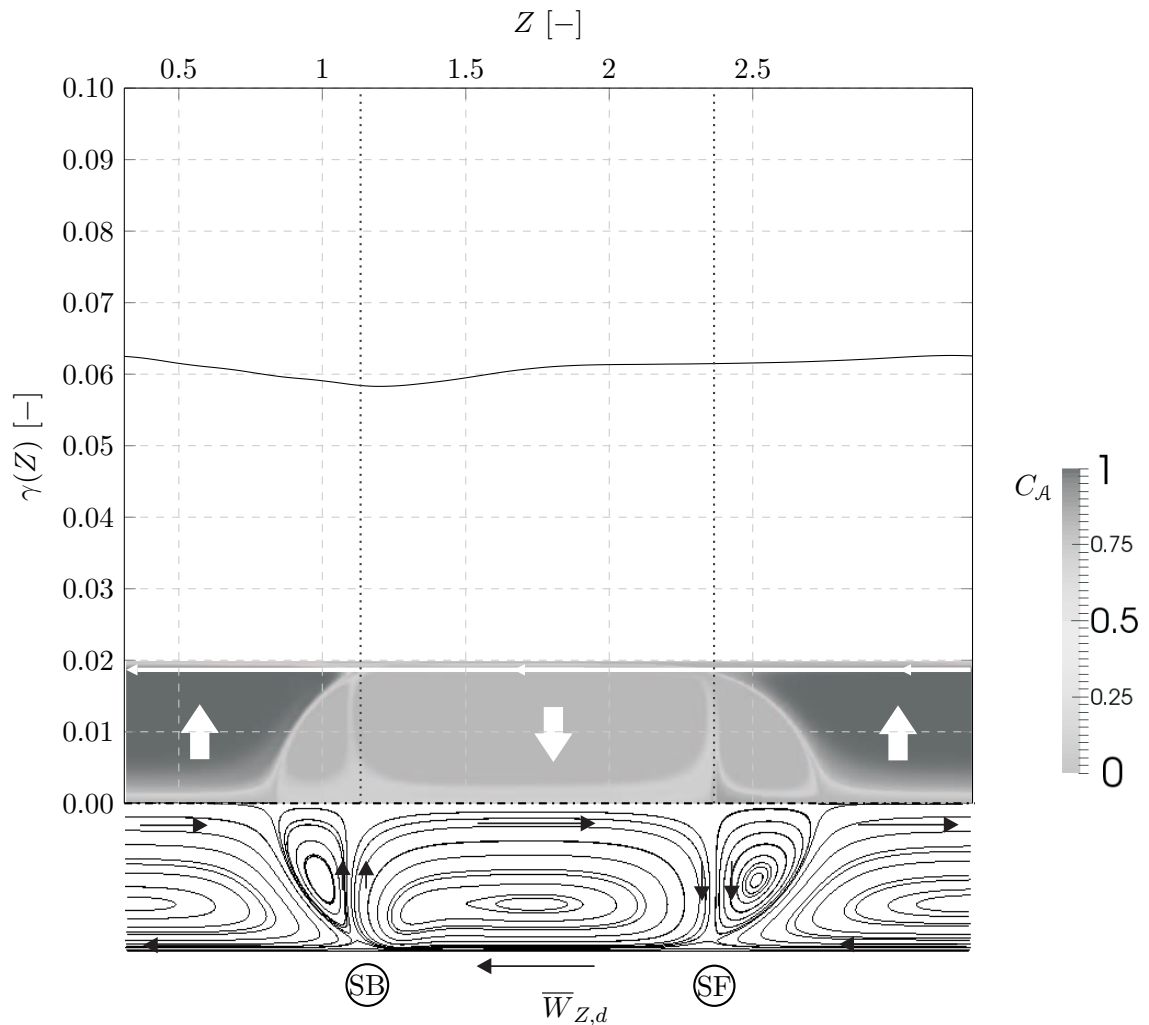
Figure 5.8: Reactive mass-transfer, reference case: Concentration distribution along the extended wall film $\gamma(Z)$ as a function of the dimensionless coordinate Z. Additionally, the concentration fields and the stream lines are shown.

5.2   Parameter study

The influence of the dimensionless model parameters, onto the dimensionless volumetric mass-transfer coefficient and its local portions is studied, using the mass-transfer test systems. The parameters are classified into three groups: flow, transport, and chemical parameters. In all cases one dimensionless parameter Π, with $\Pi = Ca_c, Pe_{r,\mathcal{A}}$, etc., is varied, while the others are kept constant.

The change of the volumetric mass-transfer coefficient, relative to the corresponding reference case at the end of the process, i.e. $F_{\mathcal{A}} = 0.95$, and of the related local portions P, with $P = WF, F, B$, are studied. The relative changes are defined to

$$\Delta Si_{rel} = \frac{Si_{max}(\Pi) - Si_{min}(\Pi)}{Si_{max}(\Pi)} \text{ and } \Delta Si_{rel}^{WF} = \frac{Si_{max}^{WF}(\Pi) - Si_{min}^{WF}(\Pi)}{Si_{max}^{WF}(\Pi)}, \qquad (5.2)$$

in the examined parameter interval $[\Pi_{min}; \Pi_{max}]$. The maximum and the minimum of the dimensionless volumetric mass-transfer coefficients $Si_{max}(\Pi)$, $Si_{min}(\Pi)$ and the corresponding wall-film portion $Si_{max}^{WF}(\Pi)$, $Si_{min}^{WF}(\Pi)$, are used for the quantitative description. Additionally, the influence to the wall-film Péclet number Pe^{WF}, the relative wall-film concentration Γ, and the interfacial wall-film portion α^{WF}/α are studied.

A correlation is derived for each parameter. Here, the best fitting Ansatz-function is used, without the use of a special theory. The mathematical expressions are incorporated into the diagrams.

5.2.1   Flow parameters

The influence of the flow parameters, i.e. the capillary number Ca_c, the viscosity ratio $\hat{\mu}$, the ratio of volumetric flow rates $\hat{V}$, and the periodic element length L_{pe} is investigated, on basis of the reference case of the physical mass-transfer test-system. The Reynolds number Re_c and the density ratio $\hat{\varrho}$ are not considered since both parameters have no influence on the flow topology, cf. Dittmar (2015). The reference parameters are given to: $Ca_c = 5.39 \cdot 10^{-3}$, $\hat{\mu} = 1.71$, $\hat{V} = 1$, $L_{pe} = 4.80$, $Pe_{r,\mathcal{A}} = 85.0 \cdot 10^4$, $\hat{D}_{\mathcal{A}} = 2.20$ and $m_{\mathcal{A}} = 0.997$. Further, $c_{e,\mathcal{B}} = 0$ is valid, indicating that no chemical reaction is considered. The raffinate solvent is assigned to the disperse phase.

Capillary number

The capillary number $Ca_c = \mu_c \overline{w}_z / \sigma$ describes the ratio of the viscous to interfacial stress and is the most influencing parameter to the flow topology. The interval $1.08 \cdot 10^{-3} \leq Ca_c \leq 1.08 \cdot 10^{-1}$ is investigated, representing the limiting parameter range for the appearance of the slug-flow topology, compare section 1.3.1. The dimensionless volumetric mass-transfer coefficient and its wall-film portion, see figure 5.9a and 5.9b, increase with the capillary number while the portions of the caps vanish. The relative change of the dimensionless volumetric mass-transfer coefficient is $\Delta Si_{rel} = 29.9\%$ and for the wall-film portion $\Delta Si_{rel}^{WF} = 14.2\%$. The relative wall-film portion is always in the range of $Si^{WF}/Si > 80\%$. The behavior is related to the large influence of the capillary number onto the flow topology, see figure 5.10. As can be seen in the figure, the interfacial portions of the caps, connected to the front and the back vortices, become smaller as the capillary number increases. The vortex on the back side of the slug weakens with increasing capillary number and may even disappear, see figure 5.11b. Further, the wall-film thickness, the related velocity difference across the wall film, and the wall-film Péclet number increase with increasing the capillary number, see figure 5.11a. As consequence, the relative
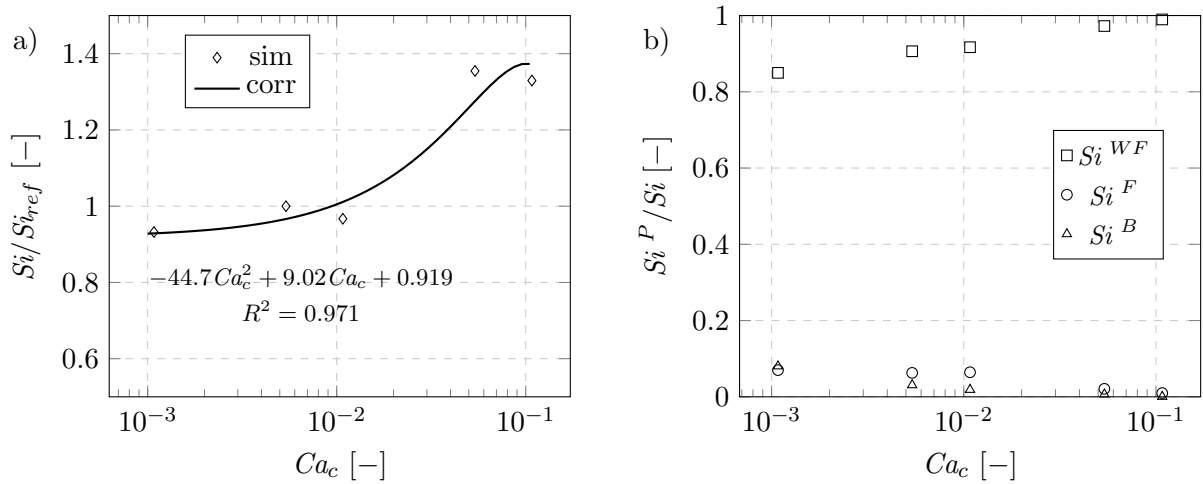
Figure 5.9: Influence of the capillary number Ca_c onto the mass transport: a) Relative dimensionless volumetric mass-transfer coefficient Si/Si_{ref}; b) Local portions Si^P/Si.

wall-film concentration decreases slightly as the axial transport in the wall film is intensified, see figure 5.11b. The change of the flow topology appears to be responsible for these changes of the dimensionless volumetric mass-transfer coefficient and its local portions. In summary, the capillary number has a medium influence to the volumetric mass-transfer coefficient, while only a small change of its wall-film portion is present. All transfer rates are normalizes with ζ_r.
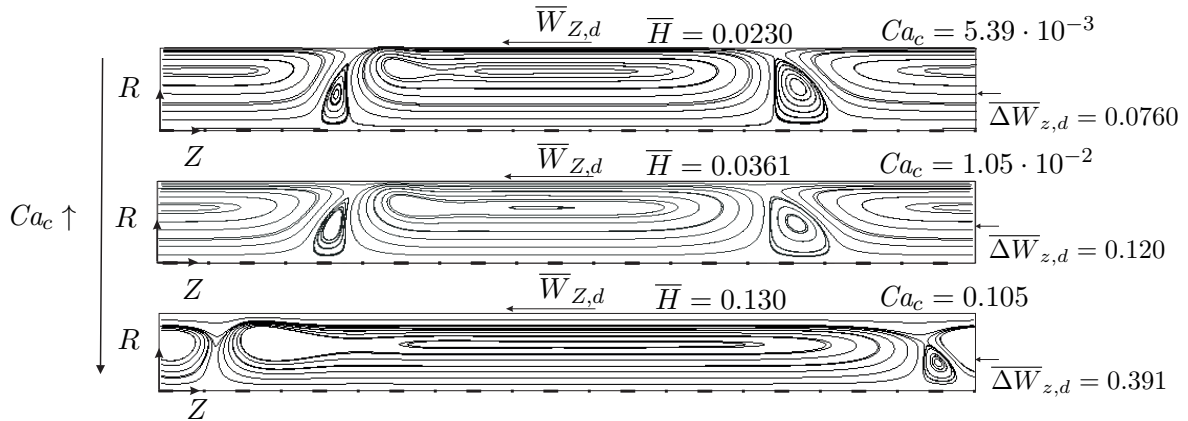
Figure 5.10: Influence of the capillary number Ca_c to the flow topology.
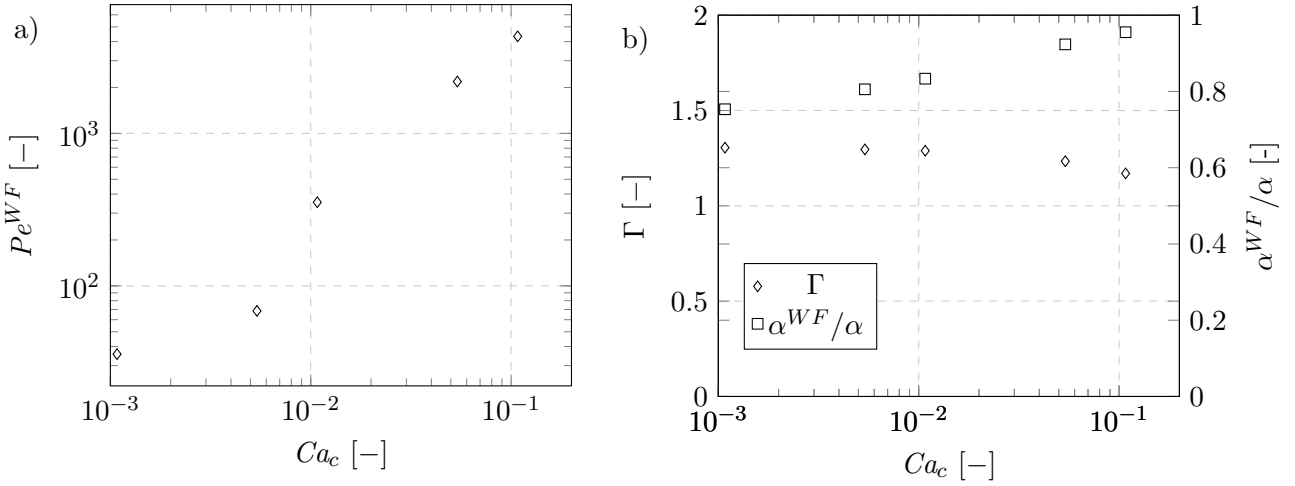
Figure 5.11: Influence of the capillary number Ca_c onto the mass transport: a) Wall-film Péclet number Pe^{WF}; b) Relative wall-film concentration Γ and wall-film portion of the interfacial area α^{WF}/α.

Viscosity ratio

A change of the viscosity ratio $\hat{\mu} = \mu_d/\mu_c$ corresponds to a change of the viscosity of the disperse phase, i.e. the raffinate solvent, at constant capillary number. The typical range for technical liquid/liquid mass-transfer systems of $0.154 \leq \hat{\mu} \leq 15.4$ is examined, cf. Lo (1991). The dimensionless volumetric mass-transfer coefficient appears to be almost constant, see figure 5.12a, with a relative change of $\Delta Si_{rel} = 6.10\%$. Only a slight relative change of its wall-film portion $\Delta Si_{rel}^{WF} = 3.70\%$ is present, see figure 5.12b, with increasing viscosity of the disperse phase. The relative wall-film portion remains in the range $Si^{WF}/Si > 80\%$. The findings are
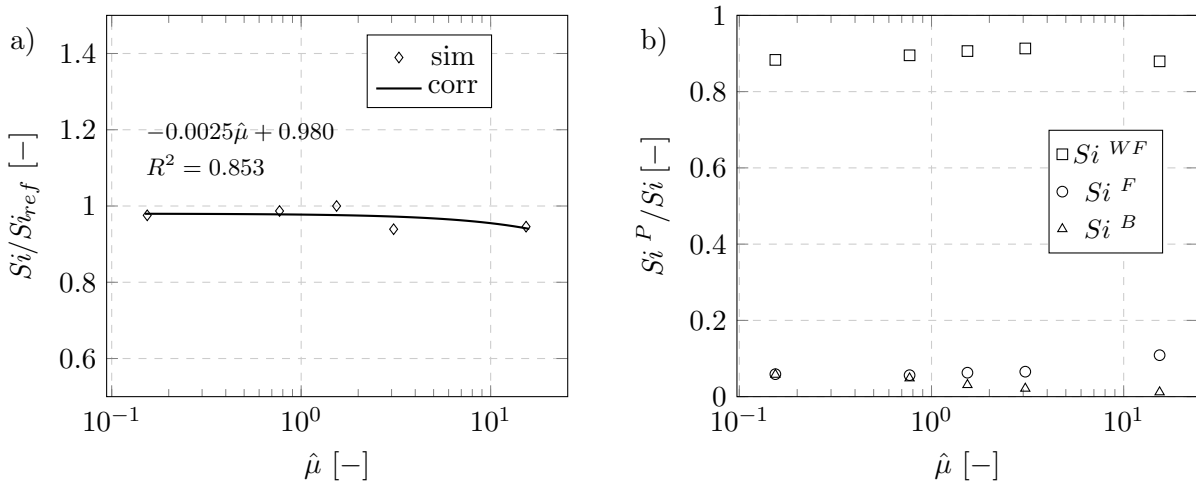
Figure 5.12: Influence of the viscosity ratio $\hat{\mu}$ onto the mass transport: a) Relative dimensionless volumetric mass-transfer coefficient Si/Si_{ref}; b) Local portions Si^P/Si.

related to the almost constant quantities of the wall-film Péclet-number, see figure 5.13a, the relative wall-film concentration, and the wall-film portion of the interfacial area, see figure 5.13b. In summary, the influence of the viscosity ratio is weak in the examined parameter range, due its the weak influence onto the flow topology.
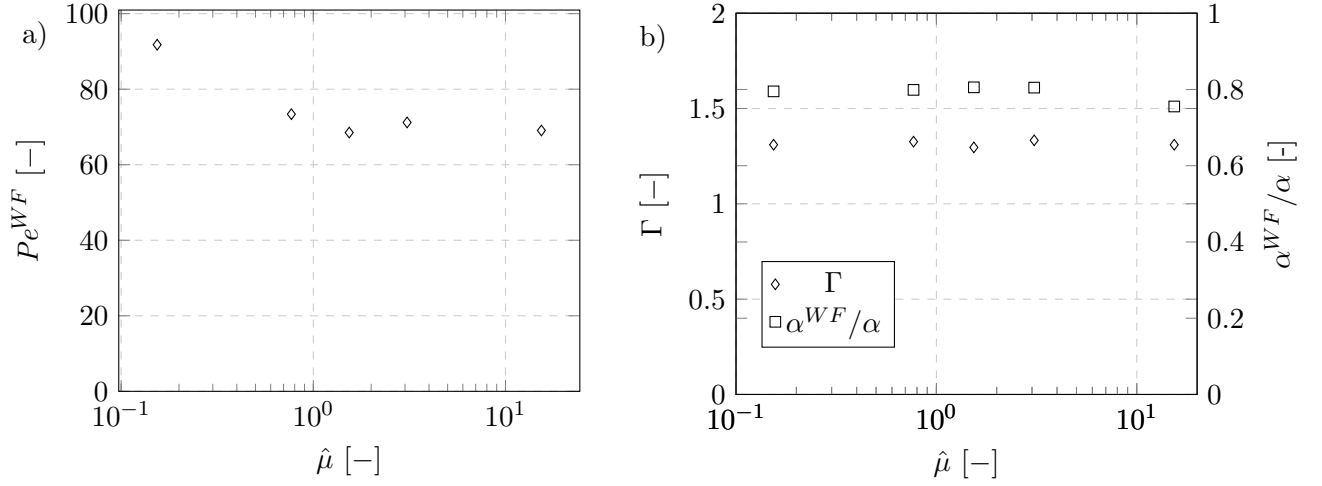
Figure 5.13: Influence of the viscosity ratio $\hat{\mu}$ onto mass transport: a) Wall-film Péclet number Pe^{WF}; b) Relative Wall-film concentration Γ and wall-film portion of the interfacial area α^{WF}/α.

Ratio of volumetric flow rates

The ratio of volumetric flow rates $\hat{V} = \dot{V}_d/\dot{V}_c$ corresponds in the current case to the ratio of the volume of the raffinate solvent to the volume of the extract solvent $\hat{V} \hat{=} \dot{V}_r/\dot{V}_e = \zeta_r/(1 - \zeta_r)$, at $Ca_c = const.$, inside the periodic element. The range $0.5 \leq \hat{V} \leq 2$ is examined, as the slug flow occurs at comparable flow rates, see section 1.3.1. The dimensionless volumetric mass-transfer coefficient decreases as the ratio of volumetric flow rates increases, see figure 5.14a. The wall portion of the volumetric mass-transfer coefficient increases in contrast, see figure 5.14b. The relative decrease of the volumetric mass-transfer coefficient is $\Delta Si_{rel} = 28.8\%$, caused by a decreasing concentration difference in conjunction with the increasing volume of the raffinate solvent, i.e. the disperse phase. The relative change of the wall-film portion is only
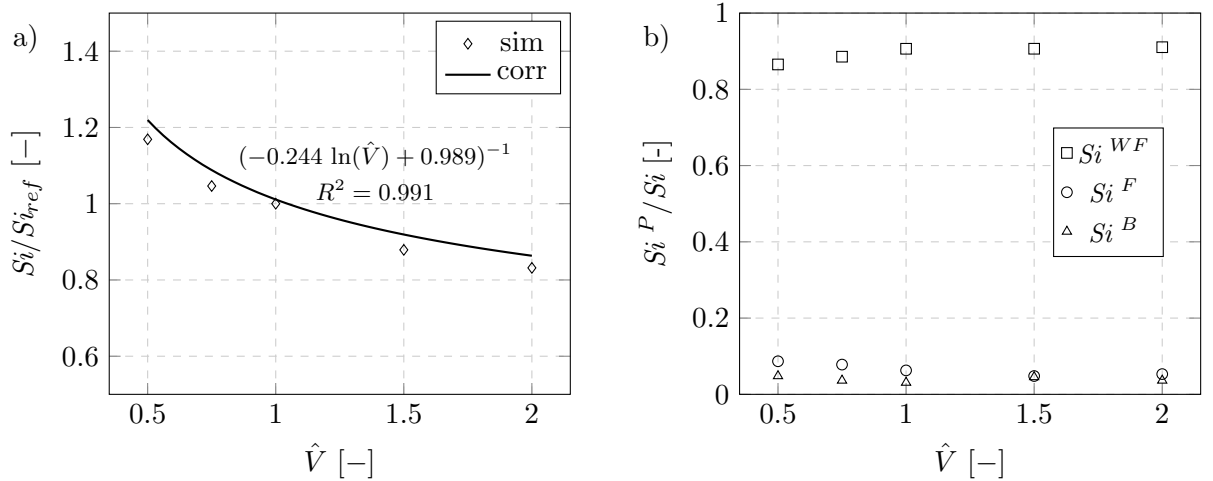
Figure 5.14: Influence of the ratio of volumetric flow rates $\hat{V}$ onto the mass transport: a) Relative dimensionless volumetric mass-transfer coefficient Si/Si_{ref}; b) Local portions Si^P/Si.

$\Delta Si_{rel}^{WF} = 5.01\%$, i.e. almost constant, whereas in all cases we have $Si^{WF}/Si > 80\%$. The increase of the wall-film portion of the dimensionless volumetric mass-transfer coefficient is in close relation to the change of the wall-film portion of the interfacial area, compare figure 5.15b. The wall-film Péclet number appears to be almost constant as the wall-film thickness and the

velocity difference show a weak dependency onto the ratio of volumetric flow rates, obvious from figure 5.15a and figure 5.15b for the relative wall film concentration. In summary, the influence of the ratio of volumetric flow rates has noticeable influence onto the volumetric mass-transfer coefficient, while the change of the wall-film portion appears to be small.
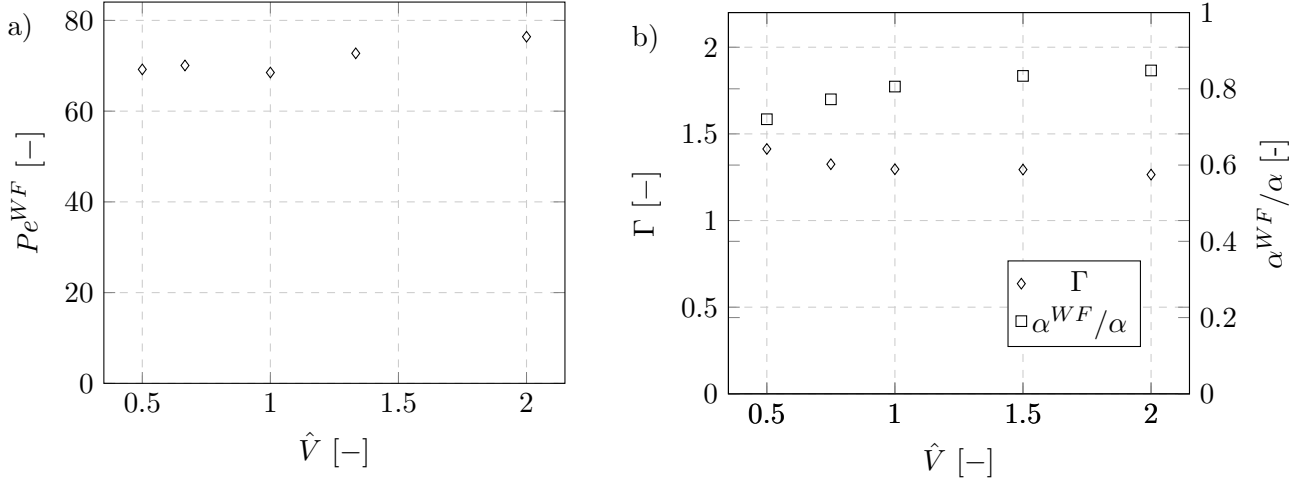
Figure 5.15: Influence of the ratio of volumetric flow-rates $\hat{V}$ onto the mass transport: a) Wall-film Péclet number Pe^{WF}; b) Relative wall-film concentration Γ and wall-film portion of the interfacial area α^{WF}/α.

Periodic element length

The dimensionless periodic element length is defined to $L_{pe} = l_{pe}/d$, with the periodic element length l_{pe} and the capillary diameter d. The lower bound for the examined range of $2.41 \leq L_{pe} \leq 19.2$ is derived in relation to the definition of the slug flow, compare section 1.3.1. The upper bound is derived from the limiting case of a very long periodic element and the stagnation of the increase of the wall film portion, compare figure 5.16b. The relative decrease of the dimensionless volumetric mass-transfer coefficient is $\Delta Si_{rel} = 28.4\%$, resulting from the change of the absolute volume of the periodic element, see figure 5.16a. Accordingly, the overall fluid mass and the transport length increase with the periodic element length. Simultaneously the wall-film portion increases, see figure 5.16b, with a relative change of $\Delta Si_{rel}^{WF} = 14.6\%$. In all cases its value is in the range $Si^{WF}/Si > 80\%$ whereas the limiting value $Si^{WF}/Si \to 100\%$ is found for $L_{pe} \to \infty$, see figure 5.16b. This behavior is again described with influence of the periodic element length onto the portions of the interfacial area, see figure 5.17b. The wall-film portion of the interfacial area increases with the periodic element length at almost constant transport conditions inside the wall film, indicated by the wall-film Péclet number and the relative wall-film concentration, see figure 5.17a and 5.17b. Hence, the change of the wall-film portion of the interfacial area explains the change of wall-film portion of the volumetric mass-transfer coefficient.
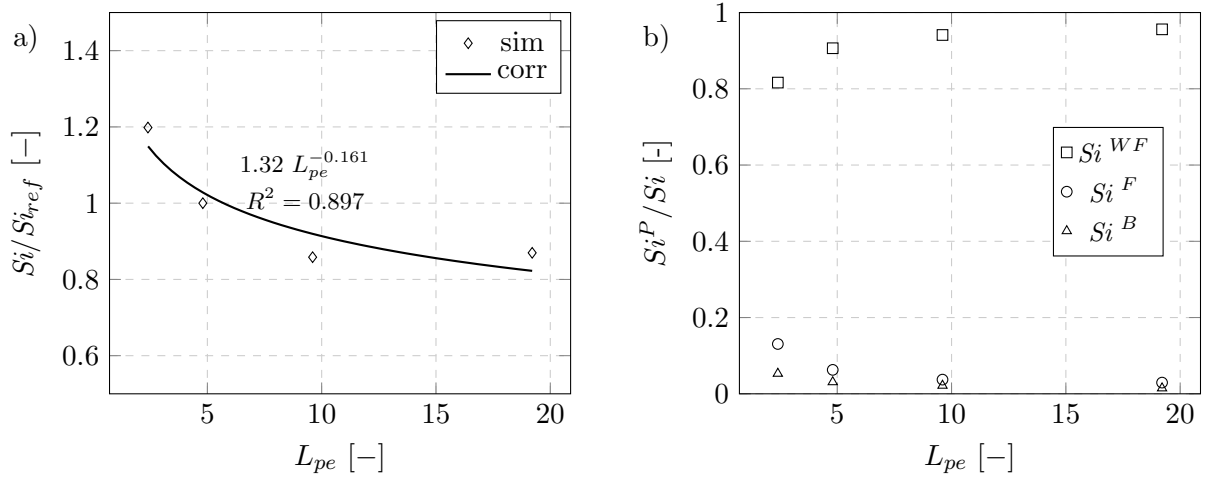
Figure 5.16: Influence of the periodic element length L_{pe} onto the mass transport: a) Relative dimensionless volumetric mass-transfer coefficient Si/Si_{ref}; b) Local portions Si^P/Si.
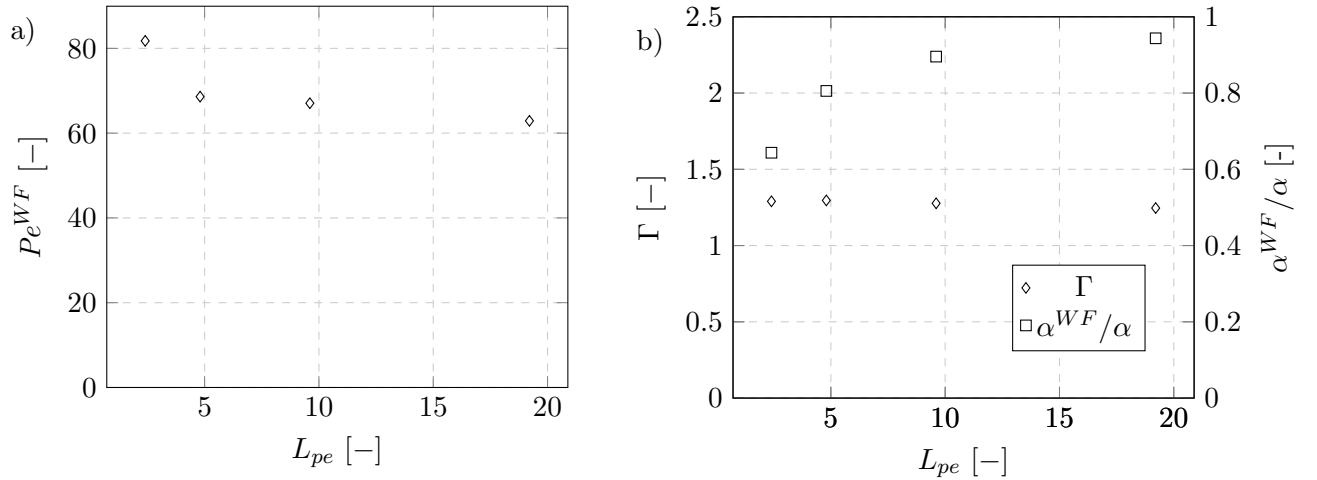
Figure 5.17: Influence of the periodic element length L_{pe} onto the mass transport: a) Wall-film Péclet number Pe^{WF}; b) Relative wall-film concentration Γ and wall-film portion of the interfacial area α^{WF}/α.

5.2.2 Transport parameters

The transport parameters are the Péclet number $Pe_{r,\mathcal{A}}$, the ratio of diffusion coefficients $\hat{D}_{\mathcal{A}}$, and the distribution coefficient $m_{\mathcal{A}}$. The following study is again conducted for pure physical mass transfer. The reference case parameters are $Ca_c = 5.39 \cdot 10^{-3}$, $\hat{\mu} = 1.54$, $\hat{V} = 1$, $L_{pe} = 4.80$, $Pe_{r,\mathcal{A}} = 85.0 \cdot 10^4$, $\hat{D}_{\mathcal{A}} = 2.20$ and, $m_{\mathcal{A}} = 1$. A chemical reaction is not present, i.e. $C_{e,\mathcal{B}}^0 = 0$, and the raffinate solvent is assigned to the disperse phase.

Péclet number

The change of the Péclet number $Pe_{r,\mathcal{A}} = \overline{w}_z d / D_{r,\mathcal{A}}$ corresponds to a change of the ratio of convection and diffusion at constant ratio of diffusion coefficients. The range of $8.50 \leq Pe_{r,\mathcal{A}} \leq 4.26 \cdot 10^5$ is examined, representing the case of intense diffusion and the case of intense convection. Here, it has to be mentioned, that for the lower bound of the examined range, an influence of axial dispersion to the volumetric mass-transfer coefficient may not be negligible, compare with the modeling assumption in chapter 2. Despite the simulated mass-transfer for the lower bound

can be seen as a good approximation for this area. The dimensionless volumetric mass-transfer coefficient increases with increasing Péclet number with a relative gain of $\Delta Si_{ref} = 98.7\%$ in the examined range, see figure 5.18a. The relative increase of the dimensionless volumetric mass-transfer coefficient becomes smaller with increasing Péclet numbers, indicated by the constant slope of the correlation (corr) in conjunction with the logarithmic scale of the abscissa. This shows the limitation of the diffusional transport to the gain of the volumetric mass-transfer coefficient, cf. Kashid (2007). The wall-film portion of the dimensionless volumetric mass-transfer coefficient shows a maximum around $Pe_{r,\mathcal{A}} \approx 10^4$, see figure 5.18b. The relative change of the wall-film portion is $\Delta Si_{rel}^{WF} = 67.7\%$ and here the ratio Si^{WF}/Si falls below 80% for lower values of the Péclet number. For $Pe_{r,\mathcal{A}} \leq 10^3$, the portions of the caps are in a comparable magnitude to the wall-film portion of the volumetric mass-transfer coefficient.
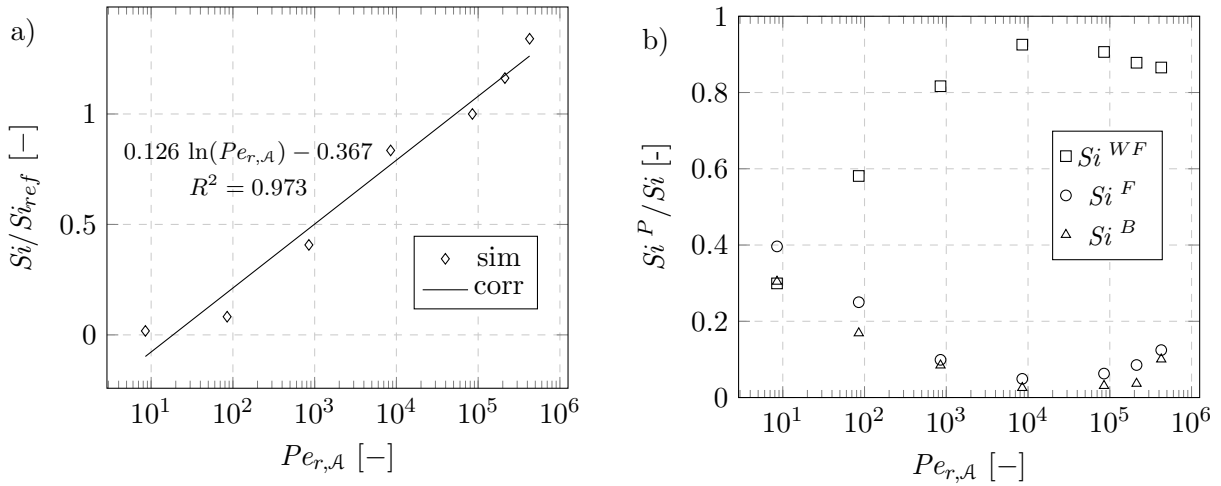
Figure 5.18: Influence of the Péclet number $Pe_{r,\mathcal{A}}$ onto the mass transport: a) Relative dimensionless volumetric mass-transfer coefficient Si/Si_{ref}; b) Local portions Si^{P}/Si.

The wall-film Péclet number increases with the Péclet number, see figure 5.19a, indicating an increase of the convective transport in the wall film. The relative wall-film concentration Γ, representing the ratio of the concentration in the wall film to the driving concentration in the continuous phase, decreases as the Péclet number increases, see figure 5.19b. Mass accumulates in the wall film for lower Péclet numbers, the transport through the wall film is hindered and contributions of the caps to the dimensionless volumetric mass-transfer coefficient increases. An increase of the ratio of convection and diffusion beyond the maximum results in a limitation of the wall-film portion of the dimensionless volumetric mass-transfer coefficient, due to the diffusive transport. The maximum of the transfer performance is reached, indicated by the almost constant wall-film ratio and the influence of the cap portions of the volumetric mass-transfer coefficient increases as result. In summary, it appears not surprising that ratio of convection and diffusion has a large influence onto the volumetric mass-transfer coefficient at the free interface and its spatial portions.
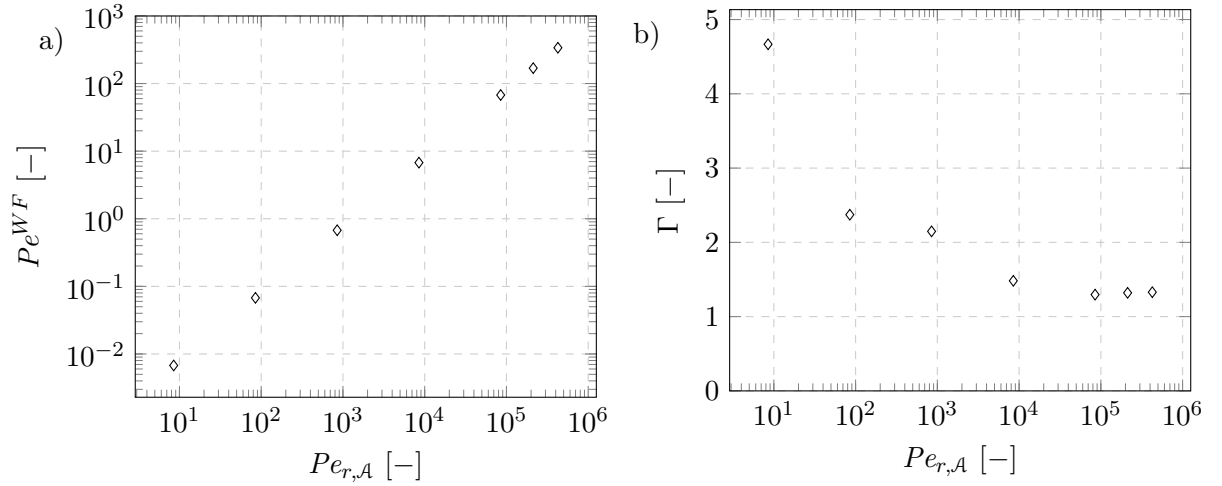
Figure 5.19: Influence of the Péclet number $Pe_{r,\mathcal{A}}$ onto the mass transport: a) Wall-film Péclet number Pe^{WF}; b) Relative wall-film concentration Γ.

Ratio of diffusivities

The ratio of diffusivities $\hat{\mathcal{D}}_\mathcal{A} = \mathcal{D}_{e,\mathcal{A}}/\mathcal{D}_{r,\mathcal{A}}$ of solute $\mathcal{A}$ is investigated at constant Péclet number $Pe_{r,\mathcal{A}}$ in the range $0.110 \leq \hat{\mathcal{D}}_\mathcal{A} \leq 11.0$, which appears to be typical for liquid/liquid systems, cf. Lo (1991). Starting at lower bound of the examined range, the dimensionless volumetric mass-transfer coefficient increases with increase of the diffusivity in the extract solvent i.e. the continuous phase, about $\Delta Si_{rel} = 85.6\%$, see figure 5.20a. The wall-film portion of the dimensionless volumetric mass-transfer coefficient is almost constant and in all cases in the range $Si^{WF}/Si \geq 80\%$, see figure 5.20b, with a relative change of $\Delta Si_{rel}^{WF} = 5.10\%$ only. The further extension of the parameter range towards $\hat{\mathcal{D}}_\mathcal{A} \to 0$ may not result in a significant change of the wall-film portion of the volumetric mass-transfer coefficient, since the wall-film portion of the volumetric mass-transfer coefficient dominates also for gas/liquid systems, with $\hat{\mathcal{D}}_\mathcal{A} \sim 10^{-4}$, cf. Sobieszuk et al. (2012) or Liu and Wang (2011). The wall-film Péclet number decreases
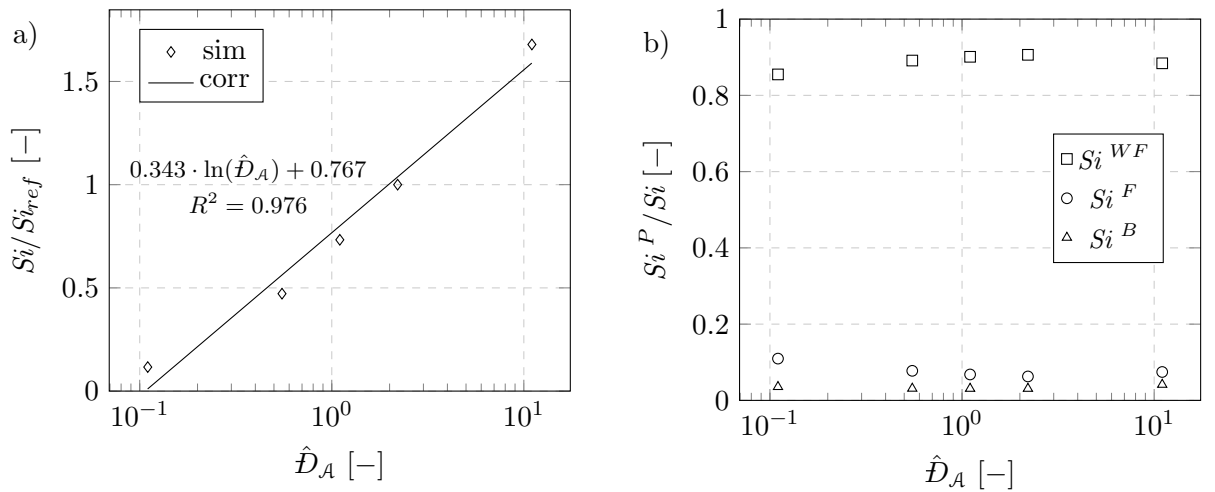
Figure 5.20: Influence of the ratio of diffusivities $\hat{\mathcal{D}}_\mathcal{A}$ onto the mass transport: a) Relative dimensionless volumetric mass-transfer coefficient Si/Si_{ref}; b) Local portions Si^P/Si.

as the ratio of diffusivities increases, i.e. the diffusion in the extract solvent, see figure 5.21a. Further, the corresponding relative wall-film concentration Γ increases slightly only, see figure

5.21b. In summary, the ratio of diffusivities has a high influence onto the dimensionless volumetric mass-transfer coefficient, while the only a weak influence to the change of the local portions is observed.
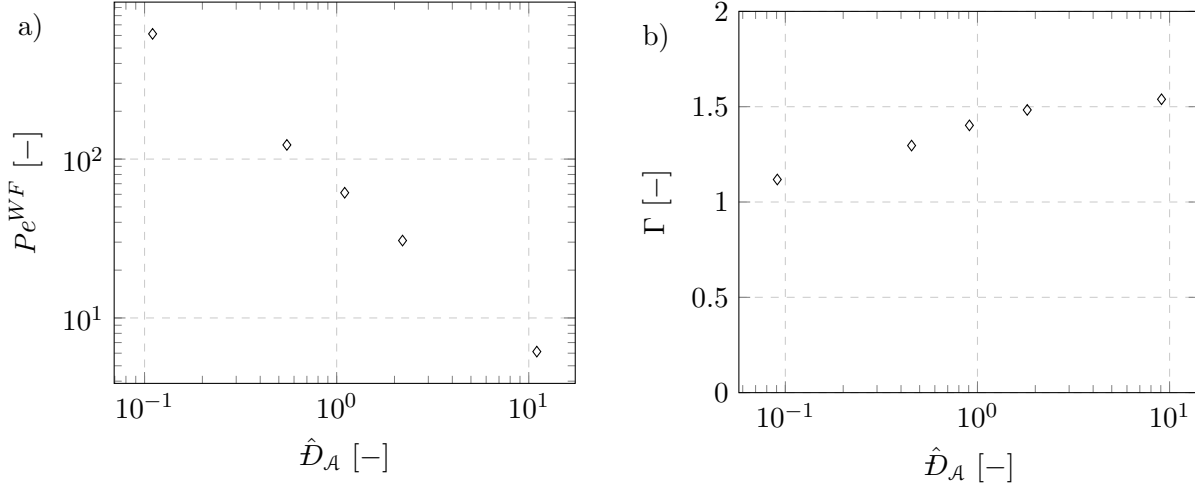
Figure 5.21: Influence of the ratio of diffusivities $\hat{D}_{\mathcal{A}}$ onto the mass transport: a) Wall-film Péclet number Pe^{WF}; b) Relative wall-film concentration Γ.

Distribution coefficient

The distribution coefficient $m_{\mathcal{A}} = c_{e,\mathcal{A}}^{IF}/c_{r,\mathcal{A}}^{IF}$, i.e. the ratio of interfacial concentrations in the extract and the raffinate solvent, is examined in the range $0.01 \leq m_{\mathcal{A}} \leq 100$. In figure 5.22a, the dimensionless volumetric mass-transfer coefficient is plotted as function of the distribution coefficient. Obviously, at both sides of the examined range an asymptotic behavior can be detected. The volumetric mass-transfer coefficient increases with increasing distribution coefficient, since the solubility inside the extract solvent increases and the resistance to the mass-transfer decreases in consequence, compare section 1.3.1. Since the driving concentration difference $\Delta c_{\mathcal{A}} = (\overline{c}_{r,\mathcal{A}} - \overline{c}_{e,\mathcal{A}}/m_{\mathcal{A}})$ grows with a increasing distribution coefficient. The relative change of the dimensionless volumetric mass-transfer coefficient is about $\Delta Si_{rel} = 97.7\%$ within the examined interval. The wall-film portion of the dimensionless volumetric mass-transfer coefficient likewise increases with an increasing distribution coefficient. The relative change in the examined range is about $\Delta Si_{rel}^{WF} = 19.4\%$, see figure 5.22b. The wall-film portion falls slightly below $Si^{WF}/Si = 80\%$ for lower distribution coefficients. The wall-film portion of the volumetric mass-transfer coefficient increases up to $Si^{WF}/Si = 95\%$ for larger volumetric mass-transfer coefficients. The back-cap portion of the volumetric mass-transfer coefficient is almost constant in the examined range and while the front-cap portion of the volumetric mass-transfer coefficient changes significantly in the examined range, traced back to the spatial distribution of the local volumetric mass-transfer coefficient, compare section 5.1.1. The largest local potential for mass transfer appears close to the spatial transition of the wall film to the front cap. The relative wall-film concentration is almost constant in the examined range, see figure 5.23. The wall-film Péclet number remains constant $Pe^{WF} = 67.5$, since the distribution coefficient does not enter. In summary, the distribution coefficient has a high influence to the dimensionless volumetric mass-transfer coefficient and again only a weak influence to the weighting of its portions.
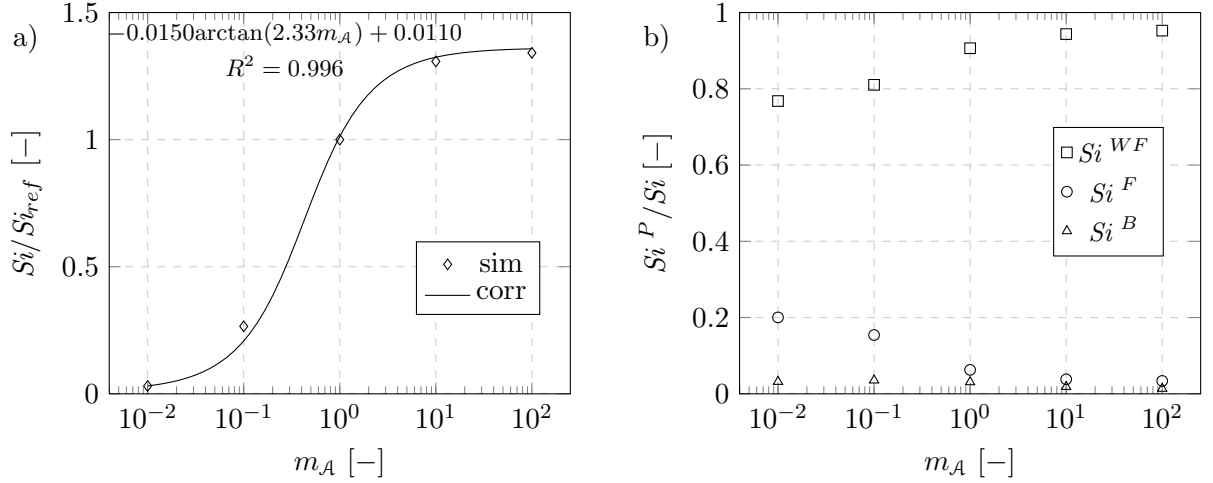
Figure 5.22: Influence of the distribution coefficient $m_{\mathcal{A}}$ onto the mass transport: a) Relative dimensionless volumetric mass-transfer coefficient Si/Si_{ref}; b) Local portions Si^P/Si.

Figure 5.23: Relative wall-film concentration Γ as function of the distribution coefficient $m_{\mathcal{A}}$.

5.2.3 Chemical parameters

The influence of the chemical parameters is based on the reactive mass transfer. The influence of the reaction velocity, i.e. the Hatta number $Ha_{e,\mathcal{A}}$, the ratio of chemical reservoirs, i.e. the excess factor ψ, and the ratio of Péclet numbers in the extract solvent λ is examined, based on the reference case of the reactive mass transfer. As basis for the parameter study, the dimensionless parameters for flow and transport are given as $Ca_c = 3.66 \cdot 10^{-3}$, $\hat{\mu} = 4.75$, $\hat{V} = 1$, $L_{pe} = 2.96$, $Pe_{r,\mathcal{A}} = 3.74 \cdot 10^4$, $\hat{D}_{\mathcal{A}} = 1.15$, and $m_{\mathcal{A}} = 85$. The chemical parameters are $Ha_{e,\mathcal{A}} = 2.74 \cdot 10^4$, $\psi = 1.77$, and $\lambda = 1.02$, with $C_{r,\mathcal{B}}^0 > 0$. A constant wall-film Péclet number of $Pe^{WF} = 40.1$ is present since the chemical parameters do not enter. The raffinate solvent is assigned to the continuous phase here. The large distribution coefficient does not have a significant influence to the local mass transfer, compare section 5.2.2.

Hatta number

The influence of the Hatta number, i.e. the reaction velocity, is examined in the range $10^1 \leq Ha_{e,\mathcal{A}} \leq 10^6$, which spans a range of fast to even instantaneous reactions. The physical volumet-

ric mass-transfer coefficient $Si(Ha_{e,\mathcal{A}} = 0)$ and its wall-film portion are used as references for the calculation of the enhancement factor. The dimensionless volumetric mass-transfer coefficient appears to be independent of the reaction rate, see figure 5.24a. The relative enhancement of the case including a chemical reaction is just about $\Delta Si_{rel} = 17.3\%$ compared to the pure physical mass transfer, i.e. the enhancement factor appears to $\mathcal{E} = 1.17$. The wall-film portion of the volumetric mass-transfer coefficient appears to be almost constant in the examined range, see figure 5.24b. It increases relatively about $\Delta Si_{rel}^{WF} = 15.2\%$ compared to the case without reaction. Further, the wall-film portion of the volumetric mass-transfer coefficient in all cases is in the range $Si^{WF}/Si > 80\%$. The relative wall-film concentration Γ, relating the concentration in the wall film to the diving concentration in the continuous phase, shows a strong dependence onto the Hatta number, see figure 5.25. The relative wall-film concentration is always below $\Gamma = 1$, since mass is transferred from the continuous into the disperse phase. For $Ha_{e,\mathcal{A}} \to \infty$ the relative wall-film concentration converges to $\Gamma \to 0$, i.e. the average concentration in the wall film converges to $\bar{c}_{sc,\mathcal{A}}^{WF} \to 0$. The low concentration in the wall film does not hinder the transfer at the wall-film portion of the free interface, as the wall-film portion of the volumetric mass-transfer coefficient dominates, see figure 5.24b. The influence of the large distribution coefficient of the reactive mass-transfer system and the portions of the volumetric mass-transfer coefficient is weak, compare with section 5.2.2. In Summary, the Hatta number has only a weak influence to the the volumetric mass-transfer coefficient and its spatial portions of the volumetric mass-transfer coefficient.

Figure 5.24: Influence of the Hatta number $Ha_{e,\mathcal{A}}$ onto the reactive mass transport: a) Relative dimensionless volumetric mass-transfer coefficient Si/Si_{ref}; b) Local portions Si^{P}/Si.

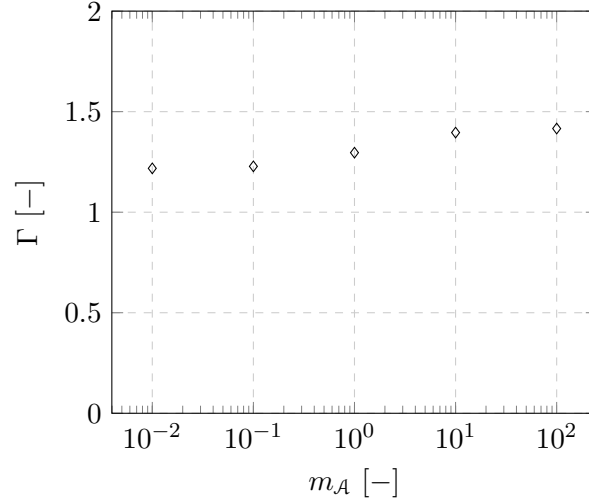**Figure 5.25:** Relative wall-film concentration Γ as function of the Hatta number $Ha_{e,\mathcal{A}}$.

Excess factor

The excess factor $\psi = \left(\nu_{\mathcal{B}} c_{r,\mathcal{A}}^0 / (\nu_{\mathcal{A}} c_{e,\mathcal{B}}^0)\right) \left[\zeta_r/(1-\zeta_r)\right]$ captures the ratio of the chemical reservoirs, with ζ_r being the volume fraction of the raffinate solvent. The parameter is examined in the range of $10^{-2} \leq \psi \leq 10^2$. For $\psi \to 0$, solute $\mathcal{B}$ is present at high excess and the largest volumetric mass-transfer coefficients are obtained, corresponding to a pseudo-first order reaction system, see figure 5.26a. The volumetric mass-transfer coefficient decreases with increasing excess factor, as the influence of the solute $\mathcal{B}$ vanishes and the system converges towards the pure physical mass transfer without chemical reaction. The relative change of the volumetric mass-transfer coefficient is about $\Delta Si_{rel} = 44.3\%$ in the examined interval. The wall-film portion is always in the range $Si^{WF}/Si > 80\%$ and shows only a weak dependency onto the excess factor, see figure 5.26b. The relative change of the wall-film portion is only about $\Delta Si_{rel}^{WF} = 15.2\%$. The relative wall-film concentration Γ decreases as the excess factor decreases and the influence

a)

b)
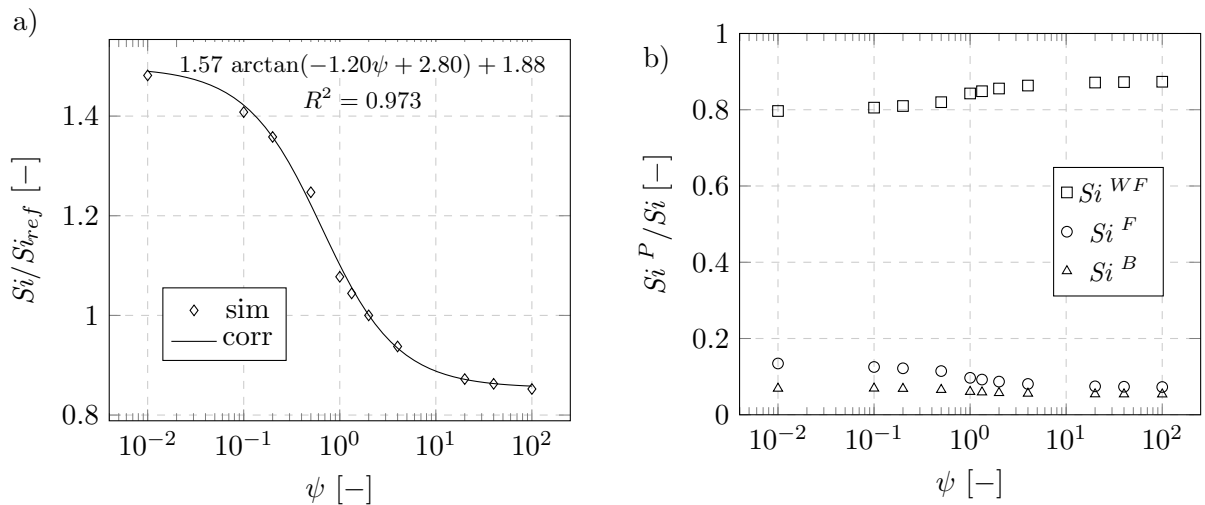
Figure 5.26: Influence of the excess factor ψ to the reactive mass transport: a) Relative dimensionless volumetric mass-transfer coefficient Si/Si_{ref}; b) Local portions Si^P/Si.

of the chemical reaction increases, see figure 5.27. The large wall-film portion of the dimensionless volumetric mass-transfer coefficient shows, that the local mass transfer at the wall-film

portion of the free interface is not hindered. In summary, the excess factor has a significant influence onto the volumetric mass-transfer coefficient, while again only a weak influence onto the weighting of the spatial portions is present.
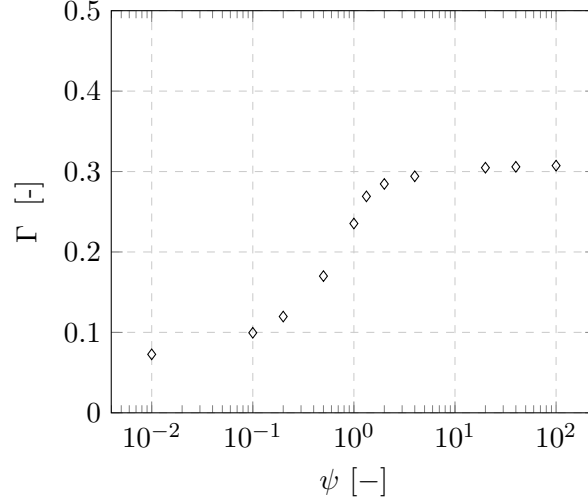
Figure 5.27: Relative wall-film concentration Γ as function of the excess factor ψ.

Ratio of Péclet numbers

The ratio of Péclet numbers $\lambda = Pe_{e,\mathcal{A}}/Pe_{e,\mathcal{B}} = \mathcal{D}_{e,\mathcal{A}}/\mathcal{D}_{r,\mathcal{A}}$, i.e. the ratio of the diffusivities of solute $\mathcal{A}$ and solute $\mathcal{B}$ the in the extract solvent, i.e. here the disperse phase. According to the typical magnitude diffusion coefficients in liquids, the range $0.1 \leq \lambda \leq 10$ is examined, cf. Lo (1991). The volumetric mass-transfer coefficient increases as the ratio of Péclet numbers increases by about $\Delta Si_{ref} = 57.7\%$, see figure 5.28a. The intensified supply of solute $\mathcal{B}$ to the free interface enhances the volumetric mass-transfer coefficient significantly and an enhancement factor of $\mathcal{E} = 2.02$ is seen. Further, the wall-film portion is almost constant with a relative change of $\Delta Si_{rel}^{WF} = 2.6\%$ and always in the range $Si^{WF}/Si > 80\%$, see figure 5.28b. The concentration of solute $\mathcal{B}$ at the interface rises as the ratio of Péclet numbers increases, due to the more intense diffusion. The relative wall-film concentration Γ decreases slightly as the ratio of Péclet numbers
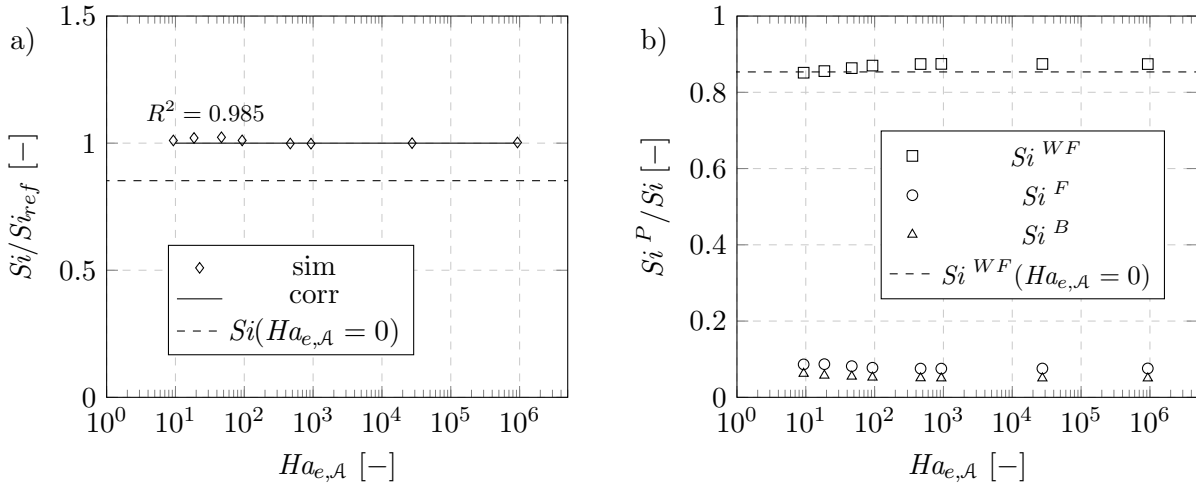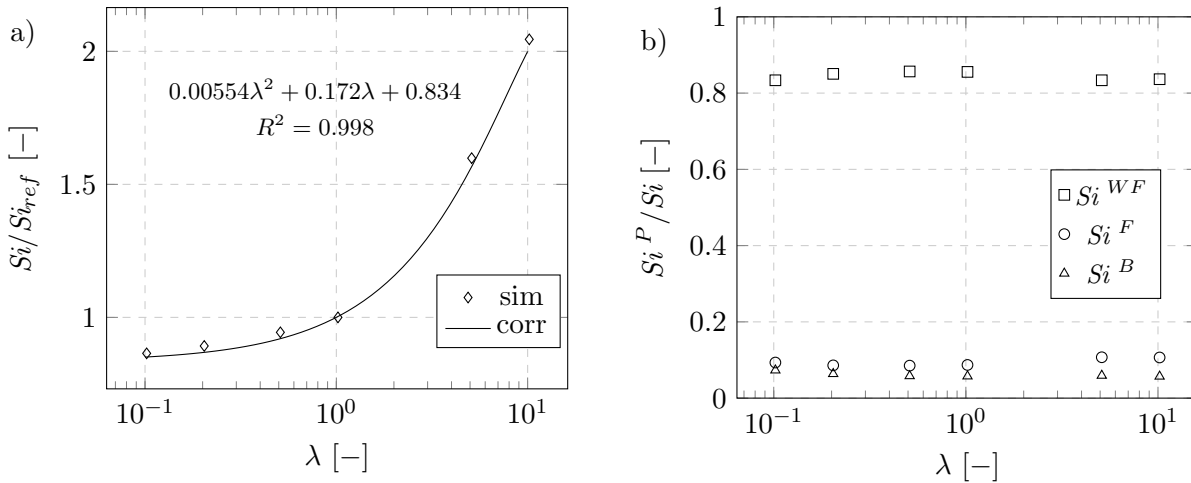

Figure 5.28: Influence of the ratio of Péclet numbers λ onto the reactive mass transport: a) Relative dimensionless volumetric mass-transfer coefficient Si/Si_{ref}; b) Local portions Si^{P}/Si.
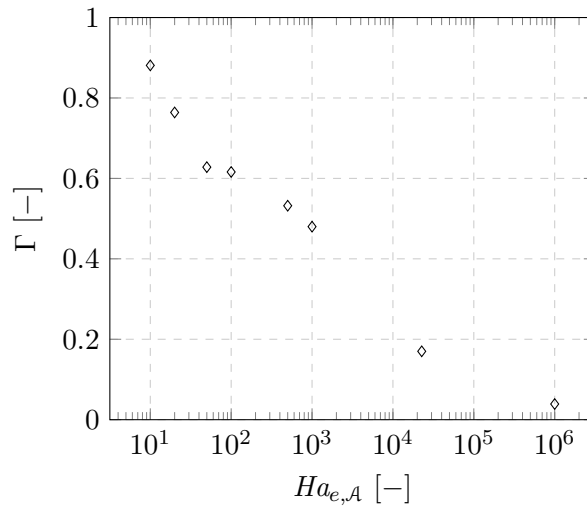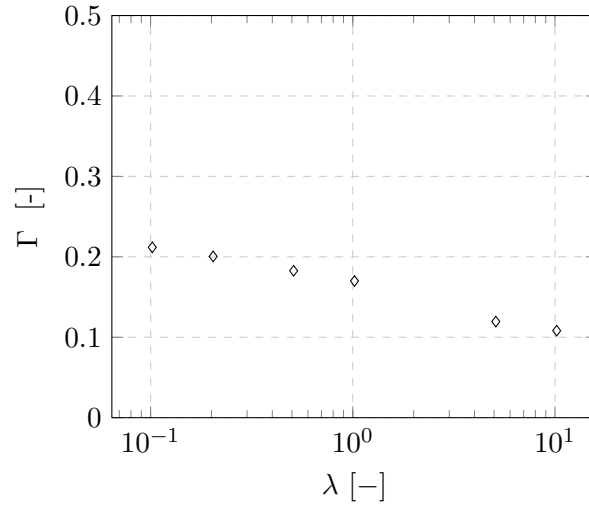
Figure 5.29: Relative wall-film concentration Γ as function of the ratio of Péclet numbers λ.

increases, see figure 5.29. The more intense diffusion of solute $\mathcal{B}$ supports the appearance of the chemical reaction close to the interface. In summary, the ratio of Péclet numbers in the extract solvent shows a strong influence to the volumetric mass-transfer coefficient, while the influence to its portions is weak again.

5.3 Conclusion

The results of the parameter study are summarized in table 5.1, containing the dimensionless parameter $\Pi = Ca_c, \hat{\mu}$, etc., the examined range $[\Pi_{min}; \Pi_{max}]$, the relative changes of the dimensionless volumetric mass-transfer coefficient ΔSi_{rel} and the related wall-film portion ΔSi_{rel}^{WF}. The dimensionless parameters and their influence onto the dimensionless volumetric mass-transfer coefficient can be classified into three groups:

I: The **transport** parameters have the greatest influence onto the volumetric mass-transfer coefficient, with a change of $\Delta Si_{rel} \sim 90\%$ for each parameter.

II: The **chemical** parameters with a magnitude of relative change of $\Delta Si_{rel} \sim 40\%$ are next.

III: Finally, the **flow** parameters cause only changes of $\Delta Si_{rel} \sim 30\%$ and, therefore, have the weakest influence.

This ranking of the different parameter classes can directly be used as a guideline for process design. Further, the derived correlations, presented in the corresponding section, can be used to predict the relative change of the dimensionless volumetric mass-transfer coefficient

$$\frac{Si}{Si_{ref}} = \mathcal{F}_{F_\mathcal{A}}(F_\mathcal{A}) \; \mathcal{F}_{Ca}(Ca_c) \; \mathcal{F}_\mu(\hat{\mu}) \; \mathcal{F}_{\hat{V}}(\hat{V}) \; \mathcal{F}_{L_{pe}}(L_{pe}) \; \mathcal{F}_{Pe}(Pe_{r,\mathcal{A}}) \; \mathcal{F}_{\hat{D}}(\hat{D}_\mathcal{A}) \; \mathcal{F}_m(m_\mathcal{A})...$$
$$... \left[1 + \mathcal{F}_{Ha}(Ha_{e,\mathcal{A}}) \; \mathcal{F}_\lambda(\lambda) \; \mathcal{F}_\psi(\psi) \right]. \tag{5.3}$$

If the physical mass transfer is examined, the Hatta number is $Ha_{e,\mathcal{A}} = 0$, i.e. $C_{e,\mathcal{B}}^0 = 0$, and the influence of the chemical parameters vanish. Here, the evolution of the transfer rate as function of the extraction rate is described by $Si(F_\mathcal{A}) = 7.46 \; F_\mathcal{A}^2 - 12.9 \; F_\mathcal{A} + 6.58$. An overall prediction error of $\epsilon_{Si} = 10\%$ has been noticed referenced to the corresponding simulation values. The largest deviations are present for the outer bounds of the examined parameter ranges.

In contrast, the wall-film portion of the volumetric mass-transfer coefficient is for almost all studied parameter combinations in the range $Si^{WF}/Si \gtrsim 80\%$. Further, most parameters have only a weak influence to the weighting of the spatial portions of the dimensionless volumetric mass-transfer coefficient, as obvious from the small relative changes ΔSi_{rel}^{WF}. A significant change of the weighting of the spatial portions of the dimensionless volumetric mass-transfer coefficient is only found for the variation of the Péclet number $Pe_{r,\mathcal{A}}$. The great influence of ratio

Table 5.1: Results of the parameter study: Given is the parameter Π, the examined range $[\Pi_{min}; \Pi_{max}]$, the related relative changes of the dimensionless volumetric mass-transfer coefficient ΔSi_{rel}, and its wall-film portion ΔSi_{rel}^{WF}.

Π	$[\Pi_{min}; \Pi_{max}]$	ΔSi_{rel}	ΔSi_{rel}^{WF}	parameter group
Ca_c	$1.08\ 10^{-3} - 0,108$	29.9%	14.2%	Flow
$\hat{\mu}$	$0.154 - 15.4$	6.10%	3.70%	Flow
$\hat{V}$	$0.5 - 2$	28.8%	5.0%	Flow
L_{pe}	$2.4 - 19.2$	28.4%	14.6%	Flow
$Pe_{r,\mathcal{A}}$	$8.5 - 4.26\ 10^5$	98.7%	**67.7**$\%$	transport
$\hat{D}_{\mathcal{A}}$	$0.110 - 11.0$	85.6%	5.10%	transport
$m_{\mathcal{A}}$	$10^{-2} - 10^2$	97.7%	19.4%	transport
$Ha_{e,\mathcal{A}}$	$0 - 10^6$	21.1%	15.2%	chemical
ψ	$10^{-3} - 4\ 10^2$	44.3%	15.2%	chemical
λ	$0.108 - 10.8$	57.7%	2.60%	chemical

of convection and diffusion onto the local mass transfer has also been derived from the literature review, compare section 1.3.2, and is traced back to the flow topology and the related transport paths. The main transport paths within the slug-flow pattern are identified and abstracted to a resistance scheme or an electrical circuit, shown in figures 5.30a and 5.30b. Therefore, the closed flow structures, consisting of vortices and the extended wall film, can be interpreted as storage volumes. In the dispersed phase the vortex at the front (FD), the main vortex (MD), and the vortex in the back (BD) can be found, while in continuous phase the main vortex (MC) and the extended wall film (EWF) are present. These flow structures are connected by resistances, where diffusional transport is active. In general, the mass-transfer resistance at the free interface can be described by means of the volumetric mass-transfer coefficient $\mathcal{R}^{IF} \propto 1/ka$ and separated into its local portions $\mathcal{R}^{WF}, \mathcal{R}^F$, and $\mathcal{R}^B$ based on the corresponding portions of the transfer rate. Additionally the resistances inside the disperse phase $\mathcal{R}^{MBD}$ and $\mathcal{R}^{MFD}$ and the continuous phase $\mathcal{R}^{MWFC}$ are present. Hence, all vortices in the disperse and the continuous phase and the wall film can exchange mass by diffusion, normal to the flow of the stream lines between the respective structures. The development of the mass transport depends on the ratios of the resistances. The investigation shows, that the wall film occupies the biggest portion of the interfacial area $\alpha^{WF}/\alpha \approx 66\%$. A large axial flow through the wall film intensifies the mass transfer at the free interface. This corresponds to a small resistance to the mass transfer compared to the caps, occupying small portion of the interfacial area and interfacial velocities of lower magnitude, compare section 1.3.2, section 5.1 and section 5.2. Accordingly, the ratio of convection and diffusion inside the wall film can be used to describe weighting of the spatial portions of the volumetric mass-transfer coefficient, i.e. captured by the wall-film Péclet number

$$Pe^{WF} = \frac{\overline{\Delta w_z}\overline{h}}{\mathcal{D}_{sc,\mathcal{A}}} \tag{5.4}$$
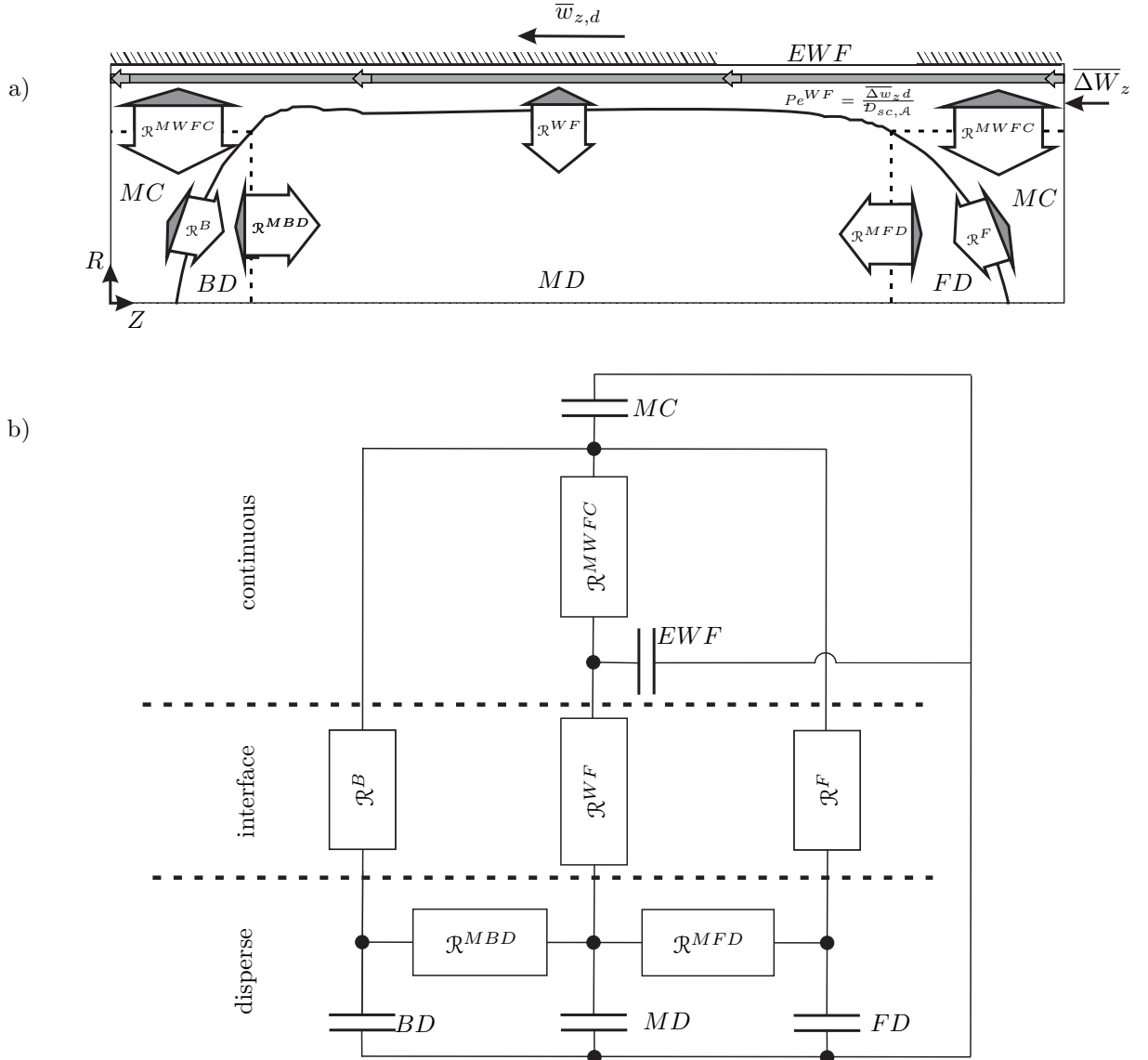
Figure 5.30: Interpretation of the mass transport in the liquid/liquid slug-flow micro-capillary reactor: a) Illustration of transport paths; b) Abstracted electrical circuit.

in good approximation. The wall-film portion of the dimensionless volumetric mass-transfer coefficient Si^{WF}/Si, therefore is plotted against the wall-film Péclet number in figure 5.31a for all simulations. The wall-film portion increases with the wall-film Péclet number till is reaches a maximum at $Pe^{WF} \approx 10$. For $Pe^{WF} > 10$ the wall-film portion of the dimensionless volumetric mass-transfer coefficient remains almost constant. The diagram can be divided into three parts:

(I): A domination of the wall-film portion can be expected for $Pe^{WF} \geq 1$, i.e. then we have $Si^{WF}/Si \geq 0.8$.

(II): For $0.2 \leq Si^{WF}/Si < 0.8$, the portions of the transfer-rates are in a comparable magnitude, given approximately for $10^{-3} \lesssim Pe^{WF} < 1$.

(III): The mass transfer through the caps dominates for $Pe^{WF} \lesssim 10^{-3}$, with $Si^{WF}/Si \leq 0.2$.

Here, it may be useful to mention, that a domination of the cap portions of the volumetric mass-transfer coefficient occurs only for very small volumetric flow rates in the magnitude of $\dot{V}_{tot} \leq 10^{-6}$ml/min or rather the stagnant case. Accumulation or depletion of mass inside the
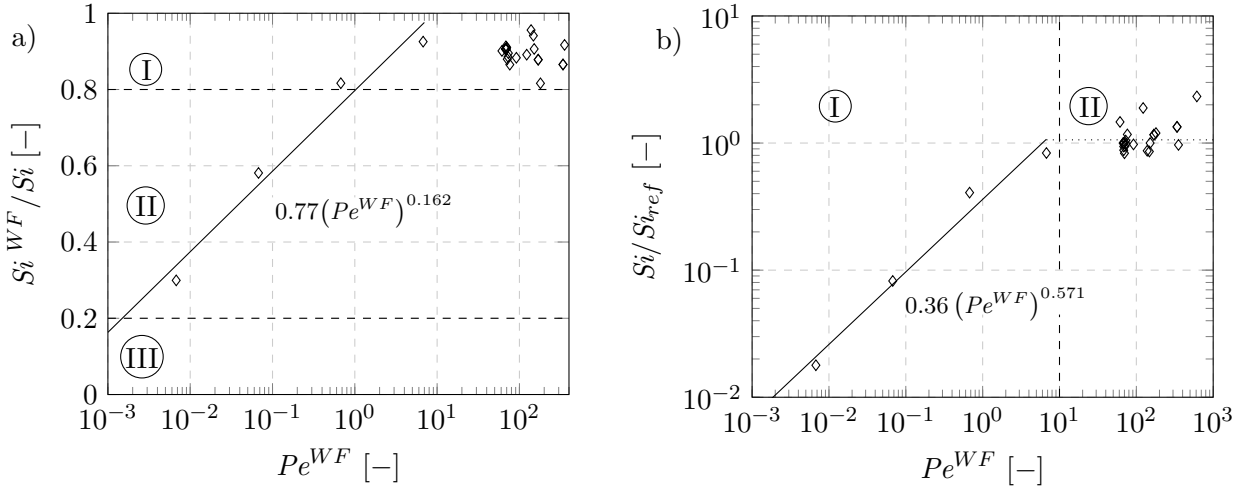
Figure 5.31: Influence of the wall-film Péclet number Pe^{WF} onto the mass transport: a) Wall-film portion of the dimensionless volumetric mass-transfer coefficient Si^{WF}/Si; b) Relative dimensionless volumetric mass-transfer coefficient Si/Si_{ref}.

wall film does hinder the mass transfer only in this case. For all other cases, the wall-film concentration appears as an effect of the large local volumetric mass-transfer coefficients. Plotting the dimensionless volumetric mass-transfer coefficient against the wall-film Péclet number shows, that large volumetric mass-transfer coefficients induce the need of a large wall-film portion of the volumetric mass-transfer coefficient, compare figure 5.31b. The volumetric mass-transfer coefficient increases monotonously with the wall-film Péclet number until it stagnates. The diagram can be divided into two parts:

(I): For $Pe^{WF} \lesssim 10^1$ a strong dependence between the dimensionless volumetric mass-transfer coefficient to the wall-film Péclet number is given.

(II): The increase of the volumetric mass-transfer coefficient becomes rather negligible for $Pe^{WF} \gtrsim 10^1$, i.e. a strong dependence onto the wall-film Péclet number Pe^{WF} is not present.

This result is closely related to the portions of the volumetric mass-transfer coefficient at the free interface, since the portion of the dimensionless volumetric mass-transfer coefficient also increases until $Pe^{WF} \approx 10$, where it reaches a maximum, cf. section 5.2.2. A further increase of Pe^{WF}, or in other words of the volumetric flow rate, does not result in an increase of the wall-film portion of the dimensionless volumetric mass-transfer coefficient, resulting in an optimized point of operation in relation to the pressure drop, i.e. the high pumping power, in the micro-capillary reactor, being significant for process applications, compare section 1.3. Accumulation of depletion of mass inside the wall film does play a subordinated rule.

The wall-film Péclet number can be evaluated from the wall-film height $\overline{h}$ and the velocity difference $\overline{\Delta w_z}$. Here, the correlations by Fairbrother and Stubbs (1935) and Bretherton (1960) are helpful, as introduced in section 1.3.1, and the wall-film Péclet-number appears to be

$$Pe^{WF} \cong Pe_{sc,\mathcal{A}} \, Ca_d^{7/6}. \qquad (5.5)$$

Here, $Pe_{sc,\mathcal{A}}$ is the Péclet number with the diffusion coefficient within the solvent, assigned to the continuous phase, and Ca_d is the capillary number of the disperse phase. The wall-film portion of the volumetric mass-transfer coefficient dominates for $Pe^{WF} \geq 1$, i.e. $Ca_d \geq Pe_{sc,\mathcal{A}}^{-6/7}$

and below this threshold a significant influence of the caps is present. Based on a typical Péclet number of $Pe_{sc,\mathcal{A}} \approx 10^3$, cf. section 1.3.1, the wall-film portion of the volumetric mass-transfer coefficient dominates for $Ca_d \geq 2.68 \cdot 10^{-3}$. Further, the optimal point of operation appears around $Pe^{WF} = 10$, cf. figures 5.31, and the optimal average channel velocity then is

$$\overline{w}_z^{opt} = \left[\frac{10 \, \mathcal{D}_{sc,\mathcal{A}}}{d} \left(\frac{\sigma}{\mu_d} \right)^{(6/7)} \right]^{(7/13)} . \tag{5.6}$$

Based on the derived typical values, cf. section 1.3.1, an optimal average flow velocity of $\overline{w}_z = 7.02 \cdot 10^{-3} m/s$ results. This optimal flow velocity has to be derived for each mass-transfer system and is not a general value.

It can be concluded that the wall film is the key element for the mass transfer at the free interface and in general the large volumetric mass-transfer coefficients occurring in the liquid/liquid slug-flow micro-capillary reactor. A wall-film portion of the dimensionless volumetric mass-transfer coefficient in the range $Si^{WF}/Si > 80\%$ clearly indicates this for collectively-dominated systems, and the portions of the caps are subordinated. The wall-film Péclet number is a simple tool for capturing the weighing of the portions of the mass transfer-rate at good approximation.

Finally, a guideline for the fluid mechanical design of a micro reactor can be derived. The operation of the reactor for a given mass-transfer system with the optimal average flow velocity results in a large volumetric mass-transfer coefficient at a desired low pumping power input, i.e. a low pressure drop. The residence time, or rather the time for mass transfer, is achieved by simply adapting of the reactor length l_{re}. Hence, an explicit reactor design can be achieved, by fairly simple means.

6

Summary and outlook

The mass transport in a liquid/liquid slug-flow micro-capillary reactor, with and without chemical reaction, is investigated. The principle micro-capillary reactor set up for two phase process applications, the slug flow, and the derivation of the volumetric mass-transfer coefficient are reviewed. Coming from the current state of scientific research regarding the local mass transfer the ratio of convection and diffusion within the thin wall film is focused, that can be described by a wall-film Péclet number Pe^{WF}.

The modeling starts from the steady-state two-phase slug flow in a periodic element with circular cross-section inside a straight micro capillary. A cylindrical coordinate system is used, that is fixed to the movement of the disperse phase, for the description of the system. The mass transport is investigated for dilute solutions and the influence of an irreversible second-order chemical reaction with constant reaction velocity in an isothermal system is taken into account. The mass-balancing approach at the periodic element considers the effect of axial dispersion for a large ratio of convection and diffusion. The free interface is separated into wall film and caps by means of the saddle points of the flow field at the free interface. The mass transfer is discussed based on the volumetric mass-transfer coefficient, that can be divided into portions by means of the flow topology, in detail the saddle points at the free interface, and its spatial distribution at the free interface.

The governing sets of equations for two-phase flow and mass transport, with and without chemical reaction, are solved numerically using an interface-tracking method. A steady-state interface is numerically obtained with an existing two-phase slug-flow simulation model, cf. Dittmar (2015). The steady-state interface is exported and used to arrange separate, phase-fitted computational domains. The steady-state two-phase flow and the reactive mass transport are solved on coupled static computational domains in a segregated manner in one-way coupling. The interface-tracking approach allows the local alignment of the flow directions of the mesh and the mass transport close to the free interface, where steep gradients can be expected. Hence, an excellent numerical quality with minimized numerical diffusion is achieved, as shown by the numerical tests.

Two mass-transfer systems, i.e. a physical and a reactive mass-transfer system, are chosen as basis for the investigation of the transport mechanisms. An experimental setup with adaptive reactor length is used to evaluate the temporal evolution of the volumetric mass-transfer coefficient for different volumetric flow rates. Low solute concentrations are used. The derivation of the related model parameters offers the basis for the adaption of the simulation model to the specific experimental conditions. The comparison of the experimental and numerical obtained evolutions of the volumetric mass-transfer coefficient show very good agreement for both cases.

The results, based on the chosen mass-transfer test systems, show that the main amount of mass is transferred into the thin wall film for both examined mass-transfer systems. The wall film occupies about 66% of the interfacial area. The relative flow through the wall film intensifies the mass transfer at the wall-film portion of the free interface and the axial transport between the solvent bulks for large Péclet numbers and the caps are of subordinated influence. The study of the effects of the dimensionless parameters, namely flow, transport and chemical parameters, shows, that the spatial weighting of the portions of the volumetric mass-transfer coefficient, in particular the wall-film portion, depends on the ratio of convection and diffusion. The presence of a chemical reaction enhances the local volumetric mass-transfer coefficient at the free interface homogeneously and the influence to the spatial distribution of the volumetric mass-transfer coefficient is negligible. The weighting of the portions of the volumetric mass-transfer coefficient is traced back to the local transport conditions inside the wall film and the wall-film Péclet number Pe^{WF}. For $Pe^{WF} > 1$, representing the common case in micro reactors, the wall-film portion of the dimensionless volumetric mass-transfer coefficient dominates, i.e. more than 80% of mass are transferred through the wall-film portion of the free interface. The increase of the volumetric mass-transfer coefficient due to convection stagnates for $Pe^{WF} \geq 10$, limited by the molecular diffusion. This result is used for the derivation of an optimal flow rate. Therefore, the wall-film Péclet number is expressed by correlations for the wall-film height and the velocity difference.

The structure, built in this thesis, offers points for future developments. Firstly, the influence of axial dispersion is only physically captured for a large ratio of convection to diffusion by the model. A detailed analysis of the influence of axial dispersion for low Péclet numbers may result in a change of the volumetric mass-transfer coefficient in this range. A change of the weighing of the portions of the volumetric mass-transfer coefficient compared to the results of this examination is expected. For its investigation a sufficient long chain of consecutive periodic elements has to be simulated without periodic coupling of the convective fluxes at the axial boundaries. The evaluated volumetric mass-transfer coefficients have to be compared to the results achieved with the simulation model of the present investigation to work out the effect of the axial dispersion to the mass transfer. Secondly, the extension of the modeling approach to finite low concentrations and the influence to the mass transfer is of interest. Therefore, the coupling of the two-phase flow and the reactive mass-transport equations has to be introduced and reactive mass transport and the now transient two-phase flow have to be solved simultaneously. The presence of a finite low concentration introduces the local and global variability of the modeling parameters, i.e. densities, viscosities, interfacial tension, diffusivities, and chemical reaction parameters. The influence of Marangoni stresses to the transfer process may be the main interest. It has to be checked, if the two-dimensional description is still valid or at least a good approximation by comparison with a three dimensional model. A third point can be, the extension of the simulation concept to curved flow channels introducing centrifugal forces and secondary flow structures, called Dean vortices, is of interest. The modular concept of the micro-capillary offers a great variability for the spatial arrangement of the residence-time unit with further intensified transfer performance, as shown by several investigations using for example curved, meandering or helical channel arrangements. Therefore, the here introduced numerical method has to be extended to the third spatial dimension. The reference simulation, the generation of the domains and the simulation of the steady-state two-phase flow have to be extended. Here, the reactive mass-transport algorithm is independent of the underlying two-phase flow topology and can be taken over.

List of symbols

Greek symbols

Symbol	Explanation	SI-Units
α	dimensionless specific interfacial area	$[-]$
β	mass-transfer coefficient	$[\text{m/s}]$
δ	phase field function, marker function	$[-]$
γ	concentration distribution along the extended wall film	$[-]$
Γ	relative wall-film concentration	$[-]$
ϵ	relative error	$[-]$
ζ	volume fraction	$[-]$
ϑ	isothermal 2. order reaction velocity constant	$[\text{m}^3/\text{mols}]$
ι, I	reaction rate, dimensionless reaction rate	$[\text{mol/(m}^3\text{s)}],[-]$
κ, K	curvature of the free interface, dimensionless curvature of the free interface	$[1/\text{m}], [-]$
λ	ratio of Péclet numbers in the extraction solvent	$[-]$
μ	dynamic viscosity	$[\text{kg/(ms)}]$
Π	general designation of a dimensionless group	$[-]$
ϱ	density	$[\text{kg/m}^3]$
σ	interfacial tension	$[\text{kg/(m s}^2)]$
τ	time	$[\text{s}]$
T	dimensionless convective time	$[-]$
φ, ϕ	circumferential coordinate, dimensionless circumferential coordinate	$[-], [-]$
ψ	excess factor	$[-]$
ω	mass fraction	$[\text{kg/kg}]$
Ω	relaxation factor	$[-]$

Latin symbols

Symbol	Explanation	SI-Units
a	specific interfacial area	$[1/\text{m}]$
A	interfacial area	$[\text{m}^2]$
A	dimensionless cell area	$[-]$
$\mathbf{A}$	cross-sectional area	$[\text{m}^2]$
$\mathcal{A}$	solute $\mathcal{A}$	$[-]$
$\mathcal{B}$	solute $\mathcal{B}$	$[-]$
c, C	concentration, dimensionless concentration	$[\text{mol/m}^3], [-]$
d, D	diameter, dimensionless diameter	$[\text{m}]$
$\mathcal{D}$	diffusion coefficient	$[\text{m}^2/\text{s}]$
e, E	cell edge length, dimensionless cell edge length	$[\text{m}], [-]$
$\vec{e}$	unit vector	$[-]$
$\mathcal{E}$	enhancement factor	$[-]$
f	force	$[\text{kg m/s}^2]$
F	extraction rate	$[-]$
g, G	gap height, dimensionless gap height	$[\text{m}], [-]$
h, H	wall-film thickness, dimensionless wall-film thickness	$[\text{m}], [-]$
it	iteration number $it = 1, ..., it_{max}$	$[-]$
k, K	overall mass-transfer coefficient, actual overall mass-transfer coefficient	$[\text{m/s}]$
$ka, d(ka), (ka)^P$	volumetric mass-transfer coefficient, local volumetric mass-transfer coefficient, portion P of volumetric mass-transfer coefficient	$[1/\text{s}]$
l, L	length, dimensionless length	$[\text{m}], [-]$

m	distribution coefficient	$[-]$
M	amount of substance	$[\text{mol}]$
n, N	interfacial normal direction, dimensionless interfacial normal direction	$[\text{m}], [-]$
$\vec{n}$	unit normal vector	$[\text{m}]$
o	O-grid meshing length/point	$[-]$
p, P	pressure, dimensionless pressure	$[\text{kg}/(\text{m s}^2)]$
Q	volumetric mass-transfer quotient	$[-]$
r, R	radial coordinate, dimensionless radial coordinate	$[\text{m}], [-]$
R^2	coefficient of determination	$[-]$
Res	residuum	$[-]$
$\mathcal{R}$	mass-transfer resistance	$[\text{s}]$
t, T	interfacial tangential direction, dimensionless interfactial tangential direction	$[\text{m}], [-]$
$\vec{u}, \vec{U}$	velocity vector, dimensionless velocity vector, velocity field	$[\text{m/s}], [-]$
u, U	Cartesian velocity component, dimensionless Cartesian velocity component	$[\text{m/s}], [-]$
v, V	Cartesian velocity component, dimensionless Cartesian velocity component	$[\text{m/s}], [-]$
w, W	Cartesian velocity component, dimensionless Cartesian velocity component	$[\text{m/s}], [-]$
V	volume	$[\text{m}^3]$
w_r, W_R	velocity in radial direction, dimensionless velocity in radial direction	$[\text{m/s}], [-]$
w_φ, W_ϕ	velocity in circumferential direction, dimensionless velocity in circumferential direction	$[\text{m/s}], [-]$
w_z, W_Z	velocity in axial direction, dimensionless velocity in axial direction	$[\text{m/s}], [-]$
y, Y	coordinate direction, dimensionless coordinate direction	$[\text{m}], [-]$
z, Z	axial direction/position along the reactor axis, dimensionless axial direction	$[\text{m}], [-]$
$\mathcal{Z}$	position along the reactor axis	$[\text{m}]$

Dimensionless groups

Symbol	Explanation
Ca	Capillary number number
Co	Courant number
Di	Diffusion number
Fo	Fourier number
Ha	Hatta number
Pe	Péclet number
Re	Reynolds number
Sh	Sherwood number
Si	dimensionless volumetric mass-transfer coefficient, product of the Sherwood number and the dimensionless specific interfacial area
dSi	local dimensionless volumetric mass-transfer coefficient
Si^P	portion of the dimensionless volumetric mass-transfer coefficient, $P = F, WF, B$

Indices

Symbol	Explanation
I, II	phase
0	initial value
∞	value for long contact times
ad	adjacent to the free interface
ana	analytical
$\mathcal{A}$	solute $\mathcal{A}$
B	back
$\mathcal{B}$	solute $\mathcal{B}$
BD	back vortex disperse
c	continuous phase
C	dimensionless concentration

Ca	capillary number
per	periodic
d	disperse phase
D	Diameter of the flow channel
$Đ$	Diffusion
dyn	dynamic
e	extraction solvent
EWF	extended wall film
F	interfacial front portion
$F_{\mathcal{A}}$	extraction rate of solute $\mathcal{A}$
FD	front vortex disperse
Ha	Hatta number
i	solute, $i = \mathcal{A}, \mathcal{B}$
it	iteration number, $it = 1, ..., it_{max}$
IF	interface
in	entering control volume
ι	chemical reaction
j	cell number
l, L	length, dimensionless length
λ	ratio of Péclet numbers
pe	periodic element
ln	logarithmic
m	mass transfer
$m_{\mathcal{A}}$	distribution coefficient of solute $\mathcal{A}$
max	maximum
min	minimum
$mesh$	computational mesh
MBD	main and back vortex disperse
MC	main vortex in the continuous phase
MD	main vortex in the disperse phase
MCD	main and front vortex disperse
$MWFC$	main vortex and wall film in the continuous phase
out	leaving control volume
opt	optimal
p	phase, $p = c, d$ or $p = I, II$
pe	periodic element
Pe	Péclet number
ψ	excess factor
∇P	pressure gradient
P	interfacial portion, $P = F, WF, B$
r	raffinate solvent
re	reactor
ref	reference
res	resulting
rel	relative
μ	viscosity
s	solvent, $s = r, e$
S	section, $S = 1, 2, 3, ...$
sc	solvent assigned to continuous phase
$stat$	static
Si	dimensionless volumetric mass-transfer coefficient
dSi	local dimensionless volumetric mass-transfer coefficient
t	tangential direction
τ_m	mass-transfer time
tot	total
V	volume
W	dimensionless velocity component
WF	wall film
z, Z	in z-direction, in dimensionless Z-direction

Mathematical operators and constants

By means of the exemplary values f and g.

Symbol	Explanation
∇f	gradient of quantity f
Δf	difference of quantity f
$\dot{f}$	flux/flow-rate of quantity f
$\overline{f}$	average of quantity f
df	infinitesimal local value of quantity f
df/dg	total derivative of quantity f with respect to g
$\partial f/\partial g$	partial derivative of quantity f with respect to g
$\vec{f}$	vector
$\vec{f}^{\,T}$	transposed vector $\vec{f}$
$|f|$	absolute of f (Euclidean norm)
$\hat{f}$	ratio of quantity $\hat{f} = f_d/f_c$, $\hat{f} = f_e/f_r$, $\hat{f} = f_1/f_2$
$\text{erf}(f)$	error function of quantity f
$\ln(f)$	logarithmus naturalis of quantity f
$\vec{f} \cdot \vec{g}$	scalar product of vectors $\vec{f}$ and $\vec{g}$
$\mathcal{F}(g)$	mathematical function depending on quantity g
$\sum_g f$	sum of f over g elements
$f|^g$	evaluation of quantity f at position g
$\min(f,g)$	minimum of quantities f and g
$\mathcal{G}$	gravitational acceleration, $\mathcal{G} = 9.81\text{m}^2/\text{s}$
π	mathematical constant $\pi \approx 3.14159$
$\arctan(f)$	arcus tangens of f

Abbreveations

Symbol	Explanation
aexp	adapted experimental data
B	back
BD	back vortex in the disperse phase
CAS	chemical abstract service
corr	correlation
exp	experimental data
EWF	extended wall film
F	front
FD	front vortex in the disperse phase
FEP	Flourinated-Ethylene-Propylene
GAMG	Gauss-algebraic-multi-grid
IF	interface
MBD	main and back vortex in the disperse phase
MCD	main and front vortex in the disperse phase
MC	main vortex in the continuous phase
MD	main vortex in the disperse phase
MWFC	main vortex and wall film in the continuous phase
PCTFE	Polychlortriflourethylen
PEEK	Poly-Ether-Ether-Ketone
PISO	pressure implicit with splitting of operators
SB	saddle point at back
SF	saddle point at front
sim	simulation data
WF	wall film

References

M. Adekojo Waheed, M. Henschke, and A. Pfennig. Mass transfer by free and forced convection from single spherical liquid drops. *Int. J. Heat Mass Transfer*, 45(22):4507–4514, 2002.

S. Afkhami, A. M. Leshansky, and Y. Renardy. Numerical investigation of elongated drops in a microfluidic T-junction. *Phys. Fluids*, 23(2):022002, 2011.

B. Ahmed, D. Barrow, and T. Wirth. Enhancement of reaction rates by segmented fluid flow in capillary scale reactors. *Adv. Synth. Catal.*, 348(9):1043–1048, 2006.

A. Alke, D. Bothe, M. Kröger, B. Weigand, D. Weirich, and H. Weking. Direct numerical simulation of high Schmidt number mass transfer from air bubbles rising in liquids using the volume-of-fluid-method. *ERCOFTAC Bull.*, 82:5–10, 2010.

D. M. Anderson, G. B. McFadden, and A. A. Wheeler. Diffusive-interface methods in fluid mechanics. *Annu. Rev. Fluid Mech.*, 30(1):139–165, 1998.

J. D. Anderson and J. F. Wendt. *Computational fluid dynamics: An introduction*. Springer, Berlin, 2009.

S. L. Anna. Droplets and bubbles in microfluidic devices. *Annu. Rev. Fluid Mech.*, 48(1):285–309, 2016.

N. Aoki, S. Tanigawa, and K. Mae. A new index for precise design and advanced operation of mass transfer in slug flow. *Chem. Eng. J.*, 167(2-3):651–656, 2011.

L. Arsenjuk, F. Kaske, J. Franzke, and D. W. Agar. Experimental investigation of wall film renewal in liquid–liquid slug flow. *Int. J. Multiphase Flow*, 85:177–185, 2016.

N. Assmann and P. R. von Rohr. Extraction in microreactors: Intensification by adding an inert gas phase. *Chem. Eng. Process.*, 50(8):822–827, 2011.

N. Assmann, A. Ładosz, and P. R. von Rohr. Continuous micro liquid-liquid extraction. *Chem. Eng. Tech.*, 36(6):921–936, 2013.

P. Aussillous and D. Quéré. Quick deposition of a fluid on the wall of a tube. *Phys. Fluids*, 12(10):2367, 2000.

H.-D. Baehr and K. Stephan. *Wärme- und Stoffübertragung*. Springer, Berlin, 2006.

H. Baltes, O. Brand, G. K. Fedder, C. Hierold, J. G. Korvink, and O. Tabata. *Micro process engineering: Fundamentals, devices, fabrication, and applications*. Wiley-VCH, Weinheim, 2008.

G. Bercic and A. Pintar. The role of gas bubbles and liquid slug lengths on mass transport in the taylor flow through capillaries. *Chem. Eng. Sci.*, 52(21-22):3709–3719, 1997.

R. B. Bird, W. E. Stewart, and E. N. Lightfoot. *Transport phenomena*. Wiley-VCH, New York, 2007.

J. U. Brackbill, D. B. Kothe, and C. Zemach. A continuum method for modeling surface tension. *J. Comput. Phys.*, 100 (2):335–354, 1992.

F. P. Bretherton. The motion of long bubbles in tubes. *J. Fluid Mech.*, 2(10):166–188, 1960.

M. R. Bringer, C. J. Gerdts, H. Song, J. D. Tice, and R. F. Ismagilov. Microfluidic systems for chemical kinetics that rely on chaotic mixing in droplets. *Philos. Trans. Royal Soc. A*, 362(1818):1087–1104, 2004.

J. R. Burns and C. Ramshaw. The intensification of rapid reactions in multiphase systems using slug flow in capillaries. *Lab Chip*, 1(1):10–15, 2001.

M. E. Charles. The pipeline flow of capsules: Part 2: Theoretical analysis of the concentric flow of cylindrical forms. *Can. J. Chem. Eng.*, (46):46–51, 1963.

Z. Che, T. N. Wong, and N.-T. Nguyen. An analytical model for plug flow in microcapillaries with circular cross section. *Int. J. Heat Fluid. Fl.*, 32(5):1005 – 1013, 2011.

G. F. Christopher and S. L. Anna. Microfluidic methods for generating continuous droplet streams. *J. Phys. D: Appl. Phys.*, 40(19):R319–R336, 2007.

R. Clift, J. R. Grace, and M. E. Weber. *Bubbles, drops, and particles*. Academic Press, New York, 1978.

J. Crank. *The mathematics of diffusion*. Clarendon Press, Oxford, 1976.

P. Dagaut and M. Cathonnet. The ignition, oxidation, and combustion of kerosene: A review of experimental and kinetic modeling. *Prog. Energy Combust. Sci.*, 32(1):48–92, 2006.

M. de Menech, P. Garstecki, F. Jousse, and H. A. Stone. Transition from squeezing to dripping in a microfluidic T-shaped junction. *J. Fluid Mech.*, 595:141–161, 2008.

A.-L. Dessimoz, L. Cavin, A. Renken, and L. Kiwi-Minsker. Liquid–liquid two-phase flow patterns and mass transfer characteristics in rectangular glass microreactors. *Chem. Eng. Sci.*, 63(16):4035–4044, 2008.

N. Di Miceli Raimondi, L. Prat, C. Gourdon, and P. Cognet. Direct numerical simulations of mass transfer in square microchannels for liquid–liquid slug flow. *Chem. Eng. Sci.*, 63(22):5522–5530, 2008.

I. Dittmar. *Numerische Untersuchung der flüssig/flüssig Pfropfenströmung in einem Mikrokapillarreaktor*. PhD thesis, TU Dortmund, Dortmund, 2015.

I. Dittmar and P. Ehrhard. Numerische Untersuchung einer Flüssig/flüssig-Pfropfenströmung in einem Mikrokapillarreaktor. *Chem. Ing. Tech.*, 85(10):1612–1618, 2013.

L. K. Doraiswamy and M. M. Sharma. *Heterogeneous Reactions: Volume 2: Fluid-fluid-solid reactions*. Wiley-VCH, 1984.

R. Dreyfus, P. Tabeling, and H. Willaime. Ordered and Disordered Patterns in Two-Phase Flows in Microchannels. *Phys. Rev. Lett.*, 90:144505, 2003.

G. Dummann, U. Quittmann, L. Gröschel, D. W. Agar, O. Wörz, and K. Morgenschweis. The capillary-microreactor: A new reactor concept for the intensification of heat and mass transfer in liquid–liquid reactions. *Catal. Today*, 79-80: 433–439, 2003.

W. Ehrfeld, V. Hessel, and H. Löwe. *Microreactors: New technology for modern chemistry*. Wiley-VCH, Weinheim, 2005.

S. Elgeti and H. Sauerland. Deforming fluid domains within the finite element method: Five mesh-based tracking methods in comparison. *Arch. Comput. Methods Eng.*, 23(2):323–361, 2016.

F. Fairbrother and A. E. Stubbs. 119. Studies in electro-endosmosis. Part VI. The "bubble-tube" method of measurement. *J. Chem. Soc.*, 0:527–529, 1935.

J. Farmer, L. Martinelli, and A. Jameson. Fast multigrid method for solving incompressible hydrodynamic problems with free surfaces. *AIAA Journal*, 32(6):1175–1182, 1994.

J. H. Ferziger and M. Peric. *Numerische Strömungsmechanik*. Springer, Berlin, 2008.

A. Fick. Ueber diffusion. *Ann. Phys.*, 170(1):59–86, 1855.

H. Foroughi and M. Kawaji. Viscous oil–water flows in a microchannel initially saturated with oil: Flow patterns and pressure drop characteristics. *Int. J. Multiphase Flow*, 37(9):1147–1155, 2011.

D. M. Fries, T. Voitl, and P. R. von Rohr. Liquid extraction of vanillin in rectangular microreactors. *Chem. Eng. Tech.*, 31 (8):1182–1187, 2008.

P. Garstecki, M. A. Fischbach, and G. M. Whitesides. Design for mixing using bubbles in branched microfluidic channels. *Appl. Phys. Lett.*, 86(24):244108, 2005.

S. Gekle. Dispersion of solute released from a sphere flowing in a microchannel. *J. Fluid Mech.*, 819:104–120, 2017.

A. Ghaini. *Untersuchung der flüssig-flüssig Propfenströmung im Kapillar-Mikroreaktor zur Intensivierung stofftrans-portlimitierter Reaktionen*. PhD thesis, TU Dortmund, Dortmund, 2011.

A. Ghaini, M. N. Kashid, and D. W. Agar. Effective interfacial area for mass transfer in the liquid–liquid slug flow capillary microreactors. *Chem. Eng. Process.*, 49(4):358–366, 2010.

M. D. Giavedoni and F. A. Saita. The rear meniscus of a long bubble steadily displacing a Newtonian liquid in a capillary tube. *Phys. Fluids*, 11(4):786–794, 1999.

B. González, A. Domínguez, and J. Tojo. Dynamic viscosities, densities, and speed of sound and derived properties of the binary systems acetic acid with water, methanol, ethanol, ethyl acetate and methyl acetate at T = (293.15, 298.15, and 303.15) K at atmospheric pressure. *J. Chem. Eng. Data*, 49(6):1590–1596, 2004.

D. Gueyffier, J. Li, A. Nadim, R. Scardovelli, and S. Zaleski. Volume-of-fluid interface tracking with smoothed surface stress methods for three-dimensional flows. *J. Comput. Phys.*, 152(2):423–456, 1999.

A. Günther and K. F. Jensen. Multiphase microfluidics: from flow characteristics to chemical and materials synthesis. *Lab Chip*, 6(12):1487–1503, 2006.

F. H. Harlow and J. E. Welch. Numerical calculation of time-dependent viscous incompressible flow of fluid with free surface. *Phys. Fluids*, 8(12):2182, 1965.

N. Harries, J. R. Burns, D. A. Barrow, and C. Ramshaw. A numerical model for segmented flow in a microreactor. *Int. J. Heat Mass Transfer*, 46(17):3313–3322, 2003.

S. Hatta. Technological reports of Tôhoku University. Tôhoku University, 119(10):613–622, 1932.

A. L. Hazel and M. Heil. The steady propagation of a semi-infinite bubble into a tube of elliptical or rectangular cross-section. *J. Fluid Mech.*, 470, 2002.

V. Hessel, H. Löwe, and S. Hardt. *Chemical micro process engineering: Fundamentals, modelling, and reactions.* Wiley-VCH, Weinheim, 2004.

C. Hirsch. *Numerical computation of internal and external flows: Introduction to the fundamentals of CFD.* Butterworth-Heinemann, Oxford, 2007.

C. W. Hirt and B.D Nichols. Volume of fluid (VOF) method for the dynamics of free boundaries. *J. Comput. Phys.*, 39(1): 201–225, 1981.

C. W. Hirt, J. L. Cook, and T. D. Butler. A Lagrangian method for calculating the dynamics of an incompressible fluid with free surface. *J. Comput. Phys.*, 5(1):103–124, 1970.

C. W. Hirt, A. A. Amsden, and J. L. Cook. An arbitrary Lagrangian–Eulerian computing method for all flow speeds. *J. Comput. Phys.*, 135(2):203–216, 1997.

D. A. Hoang, L. M. Portela, C. R. Kleijn, M. T. Kreutzer, and V. van Steijn. Dynamics of droplet breakup in a T-junction. *J. Fluid Mech.*, 717:86, 2013.

S. R. Hodges, O. E. Jensen, and J. M. Rallison. The motion of a viscous drop through a cylindrical tube. *J. Fluid Mech.*, 501:279–301, 2004.

L. Hohmann, S. K. Kurt, S. Soboll, and N. Kockmann. Separation units and equipment for lab-scale process development. *J. Flow Chem.*, 6(3):181–190, 2016.

K. Y. Huh, M. W. Golay, and V. P. Manno. A method for reduction of numerical diffusion in the donor cell treatment of convection. *J. Comput. Phys.*, 63(1):201–221, 1986.

S. Irandoust and B. Andersson. Simulation of flow and mass transfer in Taylor flow through a capillary. *Comput. Chem. Eng.*, 13(4-5):519–526, 1989.

S. Irandoust, S. Ertlé, and B. Andersson. Gas-liquid mass transfer in Taylor flow through a capillary. *Can. J. Chem. Eng.*, 70(1):115–119, 1992.

H. Jasak. *Error analysis and estimation for the finite volume method with applications to fluid flows.* PhD thesis, Imperial College London, London, 1996.

H. Jasak and A. D. Gosman. Automatic resolution control for the finite-volume method, part 1: A-priori error estimations. *Numer. Heat Transfer, Part B*, 38(3):237–256, 2000.

K. F. Jensen. Microchemical systems: Status, challenges, and opportunities. *AIChE J.*, 45(10):2051–2054, 1999.

K. F. Jensen. Microreaction engineering — is small better? *Chem. Eng. Sci.*, 56(2):293–303, 2001.

J. Jovanovic. *Liquid-liquid microreactors for phase transfer catalysis.* PhD thesis, TU Eindhoven, Eindhoven, 2011.

J. Jovanović, W. Zhou, E. V. Rebrov, T. A. Nijhuis, V. Hessel, and J. C. Schouten. Liquid–liquid slug flow: Hydrodynamics and pressure drop. *Chem. Eng. Sci.*, 66(1):42–54, 2011.

J. Jovanović, E. V. Rebrov, T. A. Nijhuis, M. T. Kreutzer, V. Hessel, and J. C. Schouten. Liquid–liquid flow in a capillary microreactor: Hydrodynamic flow patterns and extraction performance. *Ind. Eng. Chem. Res.*, 51(2):1015–1026, 2012.

G. Juncu. The influence of the Henry number on the conjugate mass transfer from a sphere. *Int. J. Heat Mass Transfer*, 37(4-5):519–530, 2001.

M. N. Kashid. *Experimental and modelling studies on liquid-liquid slug flow capillary microreactors.* PhD thesis, TU Dortmund, Dortmund, 2007.

M. N. Kashid. Quantitative prediction of flow patterns in liquid–liquid flow in micro-capillaries. *Chem. Eng. Process.*, 50 (10):972–978, 2011.

M. N. Kashid and D. W. Agar. Hydrodynamics of liquid–liquid slug flow capillary microreactor: Flow regimes, slug size and pressure drop. *Chem. Eng. J.*, 131(1-3):1–13, 2007.

M. N. Kashid, D. W. Agar, and S. Turek. CFD modelling of mass transfer with and without chemical reaction in the liquid–liquid slug flow microreactor. *Chem. Eng. Sci.*, 62(18-20):5102–5109, 2007a.

M. N. Kashid, Y. M. Harshe, and D. W. Agar. Liquid−liquid slug flow in a capillary: An alternative to suspended drop or film contactors. *Ind. Eng. Chem. Res.*, 46(25):8420–8430, 2007b.

M. N. Kashid, A. Renken, and L. Kiwi-Minsker. CFD modelling of liquid–liquid multiphase microstructured reactor: Slug flow generation. *Chem. Eng. Res. Des.*, 88(3):362–368, 2010.

M. N. Kashid, A. Renken, and L. Kiwi-Minsker. Gas–liquid and liquid–liquid mass transfer in microstructured reactors. *Chem. Eng. Sci.*, 66(17):3876–3897, 2011.

M. N. Kashid, A. Renken, and L. Kiwi-Minsker. *Microstructured devices for chemical processing.* Wiley-VCH, New York, 2015.

F. Kaske, S. Dick, S. A. Pajoohi, and D. W. Agar. The influence of operating conditions on the mass transfer performance of a micro capillary contactor with liquid–liquid slug flow. *Chem. Eng. Process.*, 108:10–16, 2016.

L. Kiwi-Minsker and A. Renken. Microstructured reactors for catalytic reactions. *Catal. Today*, 110(1):2 – 14, 2005.

N. Kockmann. *Transport phenomena in micro process engineering.* Springer, Heidelberg, 2008.

M. Köhler and B. P. Cahill. *Micro-segmented flow: Applications in chemistry and biology.* Springer, Heidelberg, 2014.

M. T. Kreutzer, F. Kapteijn, J. A. Moulijn, and J. J. Heiszwolf. Multiphase monolith reactors: Chemical reaction engineering of segmented flow in microchannels. *Chem. Eng. Sci.*, 60(22):5895–5916, 2005a.

M. T. Kreutzer, F. Kapteijn, Jacob A. Moulijn, C. R. Kleijn, and J. J. Heiszwolf. Inertial and interfacial effects on pressure drop of Taylor flow in capillaries. *AIChE J.*, 51(9):2428–2440, 2005b.

R. Kronig and J. C. Brink. On the theory of extraction from falling droplets. *Appl. Sci. Res.*, 2(1):142–154, 1951.

S. K. Kurt, I. Vural Gürsel, V. Hessel, K. D.P. Nigam, and N. Kockmann. Liquid–liquid extraction system with microstructured coiled flow inverter and other capillary setups for single-stage extraction applications. *Chem. Eng. J.*, 284:764–777, 2016.

O. Levenspiel. *Chemical reaction engineering.* Wiley-VCH, New York, 2007.

W. K. Lewis and W. G. Whitman. Principles of gas absorption. *Ind. Eng. Chem.*, 16(12):1215–1220, 1924.

D. Liu and S. Wang. Gas−liquid mass transfer in Taylor flow through circular capillaries. *Ind. Eng. Chem. Res.*, 50(4): 2323–2330, 2011.

T. C. Lo. *Handbook of solvent extraction.* Krieger, Malabar, 1991.

S. Lomel, L. Falk, J.M. Commenge, J.L. Houzelot, and K. Ramdani. The microreactor: A systematic and efficient tool for the transition from batch to continuous process? *Chem. Eng. Res. Des.*, 84(5):363 – 369, 2006.

J. Magnaudet, S. H. U. Takagi, and D. Legendre. Drag, deformation and lateral migration of a buoyant drop moving near a wall. *J. Fluid Mech.*, 476:115–157, 2003.

E. A. Mansur, M. Ye, Y. Wang, and Y. Dai. A State-of-the-Art Review of Mixing in Microfluidic Mixers. *Chin. J. Chem. Eng.*, 16(4):503 – 516, 2008.

C. Marangoni. Über die Ausbreitung der Tropfen einer Flüssigkeit auf der Oberfläche einer Anderen. *Ann. Phys.*, 219(7): 337–354, 1871.

H. Marschall, K. Hinterberger, C. Schüler, F. Habla, and O. Hinrichsen. Numerical simulation of species transfer across fluid interfaces in free-surface flows using OpenFOAM. *Chem. Eng. Sci.*, 78:111–127, 2012.

U. Miessner, R. Lindken, and J. Westerweel. 3D - Velocity measurements in microscopic two-phase flows by means of micro PIV. In 14th Int. Symp. on Applications of Laser Techniques to Fluid Mechanics, Lisbon, Portugal, 2008.

T. Misek and R. Berger. *Standard test systems for liquid extraction.* IChemE, Rugby, 1985.

C. E. Mortimer, U. Müller, and J. Beck. *Chemie: Das Basiswissen der Chemie.* Georg Thieme Verlag, Stuttgart and New York, 2015.

M. Muradoglu, A. Günther, and H. A. Stone. A computational study of axial dispersion in segmented gas-liquid flow. *Phys. Fluids*, 19(7):072109, 2007.

S. Muzaferija and M. Perić. Computation of free-surface flows using the finite-volume method and moving grids. *Numer. Heat Transfer, Part B*, 32(4):369–384, 1997.

W Nernst. Verteilung eines Stoffes zwischen zwei Lösungsmitteln und zwischen Lösungsmittel und Dampfraum. *Z. Phys. Chem.*, 8(1):110–139, 1891.

A. B. Newman. The drying of porous solids : Diffusion calculations. *Trans. AIChE*, 27:203–220, 1931.

C. A. Nielsen, R. W. Chrisman, R. E. LaPointe, and T. E. Miller. Novel tubing microreactor for monitoring chemical reactions. *Anal. Chem.*, 74(13):3112–3117, 2002.

H. Oertel. *Prandtl - Führer durch die Strömungslehre: Grundlagen und Phänomene*. Vieweg+Teubner, Wiesbaden, 2008.

Y. Okubo, T. Maki, N. Aoki, T. Hong Khoo, Y. Ohmukai, and K. Mae. Liquid–liquid extraction for efficient synthesis and separation by utilizing micro spaces. *Chem. Eng. Sci.*, 63(16):4070–4077, 2008.

E. Olsson and G. Kreiss. A conservative level set method for two phase flow. *J. Comput. Phys.*, 210(1):225–246, 2005.

E. Olsson, G. Kreiss, and S. Zahedi. A conservative level set method for two phase flow ii. *J. Comput. Phys.*, 225(1): 785–807, 2007.

S. Osher and J. A. Sethian. Fronts propagating with curvature-dependent speed: Algorithms based on Hamilton-Jacobi formulations. *J. Comput. Phys.*, 79(1):12–49, 1988.

F. Özkan, A. Wenka, E. Hansjosten, P. Pfeifer, and B. Kraushaar-Czarnetzki. Numerical investigation of interfacial mass transfer in two phase flows using the VOF method. *Eng. Appl. Comp. Fluid*, 10(1):100–110, 2016.

C.-W. Park and G. M. Homsy. Two-phase displacement in Hele Shaw cells: Theory. *J. Fluid Mech.*, 139:291, 1984.

S. V. Patankar. *Numerical heat transfer and fluid flow*. Hemisphere Publ. Co, New York, 1980.

H. Pedersen and C. Horvath. Axial dispersion in a segmented gas-liquid flow. *Ind. Eng. Chem. Fundam.*, 20(3):181–186, 1981.

R. H. Perry, D. W. Green, and J. O. Maloney. *Perry's chemical engineers' handbook*. McGraw-Hill, New York, 1997.

C. S. Peskin. The immersed boundary method. *Acta Numerica*, 11:1–39, 2002.

P. Plouffe, D. M. Roberge, J. Sieber, M. Bittel, and A. Macchi. Liquid–liquid mass transfer in a serpentine micro-reactor using various solvents. *Chem. Eng.J.*, 285:605–615, 2016.

R. Pohorecki. Effectiveness of interfacial area for mass transfer in two-phase flow in microreactors. *Chem. Eng. Sci.*, 62 (22):6495–6498, 2007.

M. Roudet, K. Loubiere, C. Gourdon, and M. Cabassud. Hydrodynamic and mass transfer in inertial gas–liquid flow regimes through straight and meandering millimetric square channels. *Chem. Eng. Sci.*, 66(13):2974–2990, 2011.

H. Rusche. *Computational fluid dynamics of dispersed two-phase flows at high phase fractions*. PhD thesis, Imperial College London, London, 2002.

T. W. F. Russell, A. S. Robinson, and N. J. Wagner. *Mass and heat transfer: Analysis of mass contactors and heat exchangers*. Cambridge University Press, Cambridge, 2008.

G. Ryskin and L. G. Leal. Orthogonal mapping. *J. Comput. Phys.*, 50(1):71–100, 1983.

G. Ryskin and L. G. Leal. Numerical solution of free-boundary problems in fluid mechanics. Part 1. The finite-difference technique. *J. Fluid Mech.*, 148:1–17, 1984a.

G. Ryskin and L. G. Leal. Numerical solution of free-boundary problems in fluid mechanics. Part 2. Buoyancy-driven motion of a gas bubble through a quiescent liquid. *J. Fluid Mech.*, 148:19–35, 1984b.

G. Ryskin and L. G. Leal. Numerical solution of free-boundary problems in fluid mechanics. Part 3. Bubble deformation in an axisymmetric straining flow. *J. Fluid Mech.*, 148:37–43, 1984c.

A. F. M. Salim, J. Pironon, and J. Sausse. Oil-water two-phase flow in microchannels: Flow patterns and pressure drop measurements. *Can. J. Chem. Eng.*, 86(6):978–988, 2008.

E. Samson. Calculation of ionic diffusion coefficients on the basis of migration test results. *Mater. Struct.*, 36(257):156–165, 2003.

F. Sarrazin, K. Loubière, L. Prat, C. Gourdon, T. Bonometti, and J. Magnaudet. Experimental and numerical study of droplets hydrodynamics in microchannels. *AIChE J.*, 52(12):4061–4070, 2006.

F. Scheiff. *Fluiddynamik, Stofftransport und chemische Reaktion der Suspensionskatalyse bei der flüssig/flüssig Pfropfen-strömung*. PhD thesis, TU Dortmund, Dortmund, 2015.

F. Scheiff, M. Mendorf, D. W. Agar, N. Reis, and M. Mackley. The separation of immiscible liquid slugs within plastic microchannels using a metallic hydrophilic sidestream. *Lab Chip*, 11(6):1022–1029, 2011.

D. P. Schmidt, M. Dai, H. Wang, and J. B. Perot. Direct interface tracking of droplet formation. *Atomization Sprays*, 12 (5-6):721–736, 2002.

K. Schulze. *Stoffaustausch und Fluiddynamik am bewegten Einzeltropfen unter dem Einfluss von Marangonikonvektion*. PhD thesis, TU Berlin, Berlin, 2007.

L. E. Scriven and C. V. Sterling. The Marangoni effects. *Nature*, 187(4733):186–188, 1960.

L.E. Scriven. Dynamics of a fluid interface Equation of motion for Newtonian surface fluids. *Chem. Eng. Sci.*, 12(2):98 – 108, 1960.

N. Shao, A. Gavriilidis, and P. Angeli. Mass transfer during Taylor flow in microchannels with and without chemical reaction. *Chem. Eng. J.*, 160:873–881, 06 2010.

A. H. P. Skelland. *Diffusional mass transfer*. Krieger, Malabar, 1985.

P. Sobieszuk, R. Pohorecki, P. Cygański, and J. Grzelka. Determination of the interfacial area and mass transfer coefficients in the Taylor gas–liquid flow in a microchannel. *Chem. Eng. Sci.*, 66(23):6048–6056, 2011.

P. Sobieszuk, J. Aubin, and R. Pohorecki. Hydrodynamics and mass transfer in gas-liquid flows in microreactors. *Chem. Eng. Technol.*, 35(8):1346–1358, 2012.

K.-I. Sotowa. Fluid behaviour and mass transport characteristics of gas-liquid and liquid-liquid flows in microchannels. *J. Chem. Eng. Japan*, 47(3):213–224, 2014.

M. Suo and P. Griffith. Two-Phase Flow in Capillary Tubes. *J. Basic. Eng.*, 86(3):576, 1964.

J. G. M. W. Susanti, , B. Schuur, H. J. Heeres, and J. Yue. Lactic acid extraction and mass transfer characteristics in slug flow capillary microreactors. *Ind. Eng. Chem. Res.*, 55(16):4691–4702, 2016.

M. Sussman, K. M. Smith, M. Y. Hussaini, M. Ohta, and R. Zhi-Wei. A sharp interface method for incompressible two-phase flows. *J. Comput. Phys.*, 221(2):469–505, 2007.

T. Taha and Z. F. Cui. CFD modelling of slug flow inside square capillaries. *Chem. Eng. Sci.*, 61(2):665–675, 2006.

J. Tan, Y. C. Lu, J. H. Xu, and G. S. Luo. Mass transfer performance of gas–liquid segmented flow in microchannels. *Chem. Eng. J.*, 181-182:229–235, 2012.

G. I. Taylor. The motion of ellipsoidal particles in a viscous fluid. *Proc. R. Soc. London, Ser. A*, 103(720):58–61, 1923.

G. I. Taylor. Deposition of a viscous fluid on the wall of a tube. *J. Fluid Mech.*, 10(02):161, 1961.

T. C. Thulasidas, M. A. Abraham, and R. L. Cerro. Flow patterns in liquid slugs during bubble-train flow inside capillaries. *Chem. Eng. Sci.*, 52(17):2947–2962, 1997.

T. C. Thulasidas, M. A. Abraham, and R. L. Cerro. Dispersion during bubble-train flow in capillaries. *Chem. Eng. Sci.*, 54(1):61–76, 1999.

J. D. Tice, H. Songn, A. D. Lyon, and R. F. Ismagilov. Formation of droplets and mixing in multiphase microfluidics at low values of the Reynolds and the capillary numbers. *Langmuir*, 19(22):9127–9133, 2003.

K. A. Triplett, S. M. Ghiaasiaan, S. I. Abdel-Khalik, and D. L. Sadowski. Gas–liquid two-phase flow in microchannels Part I: Two-phase flow patterns. *Int. J. Multiphase Flow*, 25(3):377–394, 1999.

G. Tryggvason, B. Bunner, A. Esmaeeli, D. Juric, N. Al-Rawahi, W. Tauber, J. Han, S. Nas, and Y.-J. Jan. A front-tracking method for the computations of multiphase flow. *J. Comput. Phys.*, 169(2):708–759, 2001.

D. Tsaoulidis. *Studies of intensified small-scale processes for liquid-liquid separations in spent nuclear fuel reprocessing*. PhD thesis, University College London, London, 2015.

D. Tsaoulidis and P. Angeli. Effect of channel size on mass transfer during liquid–liquid plug flow in small scale extractors. *Chem. Eng. J.*, 262:785–793, 2015.

Ž. Tuković and H. Jasak. A moving mesh finite volume interface tracking method for surface tension dominated interfacial fluid flow. *Comput. Fluids*, 55:70–84, 2012.

J. M. van Baten and R. Krishna. CFD simulations of mass transfer from Taylor bubbles rising in circular capillaries. *Chem. Eng. Sci.*, 59(12):2535–2545, 2004.

T. van Gerven and A. Stankiewicz. Structure, energy, synergy, time: The fundamentals of process intensification. *Ind. Eng. Chem. Res.*, 48(5):2465–2474, 2009.

C. O. Vandu, H. Liu, and R. Krishna. Mass transfer from Taylor bubbles rising in single capillaries. *Chem. Eng. Sci.*, 60 (22):6430–6437, 2005.

A. Wegmann and P. R. von Rohr. Two phase liquid–liquid flows in pipes of small diameters. *Int. J. Multiphase Flow*, 32 (8):1017–1028, 2006.

M. Wegner. *Der Einfluss der konzentrationsinduzierten Marangonikonvektion auf den instationären Impuls- und Stofftransport an Einzeltropfen*. PhD thesis, TU Berlin, Berlin, 2009.

H. G. Weller, G. Tabor, H. Jasak, and C. Fureby. A tensorial approach to computational continuum mechanics using object-oriented techniques. *Comput. Physics*, 12(6):620, 1998.

C. R. Wilke and P. Chang. Correlation of diffusion coefficients in dilute solutions. *AIChE J.*, 1(2):264–270, 1955.

S. Wolf. *Phasengrenzkonvektionen beim Stoffübergang in flüssig-flüssig-Systemen*. PhD thesis, TU München, München, 1998.

H. Wong, C. J. Radke, and S. Morris. The motion of long bubbles in polygonal capillaries. Part 1. Thin films. *J. Fluid Mech.*, 292(-1):71, 1995.

M. Wörner. Numerical modeling of multiphase flows in microfluidics and micro process engineering: A review of methods and applications. *Microfluid. Nanofluid.*, 12(6):841–886, 2012.

C. Yang and Z.-S. Mao. Numerical simulation of interphase mass transfer with the level set approach. *Chem. Eng. Sci.*, 60 (10):2643–2660, 2005.

J. Yue, G. Chen, Q. Yuan, L. Luo, and Y. Gonthier. Hydrodynamics and mass transfer characteristics in gas–liquid flow through a rectangular microchannel. *Chem. Eng. Sci.*, 62(7):2096–2108, 2007.

R. Zellner, K. Erler, and D. Field. Kinetics of the recombination reaction OH+H+M→H2O+M at low temperatures. *Proc. Combust. Inst*, 16(1):939–948, 1977.

Y. Zhao, G. Chen, and Q. Yuan. Liquid-liquid two-phase flow patterns in a rectangular microchannel. *AIChE J.*, 52(12): 4052–4060, 2006.

Y. Zhao, G. Chen, and Q. Yuan. Liquid–liquid two-phase mass transfer in the T-junction microchannels. *AIChE J.*, 53 (12):3042–3053, 2007.

Z. M. Zorin and N. V. Churaev. Immiscible liquid-liquid displacement in thin quartz capillaries. *Adv. Colloid Interfac.*, 40: 85–108, 1992.